The Assembly of Cluster Galaxies

Vandana Desai

A dissertation submitted in partial fulfillment
of the requirements for the degree of

Doctor of Philosophy

University of Washington

2004

Program Authorized to Offer Degree: Astronomy

ProQuest Information and Learning Company
300 North Zeeb Road
P.O. Box 1346
Ann Arbor, MI 48106-1346

University of Washington
Graduate School

This is to certify that I have examined this copy of a doctoral dissertation by

Vandana Desai

and have found that it is complete and satisfactory in all respects,
and that any and all revisions required by the final
examining committee have been made.

Chair of Supervisory Committee:

Julianne J. Dalcanton

Reading Committee:

Julianne J. Dalcanton

Fabio Governato

Thomas Quinn

Date: 08-18-04

Signature

Date 08-18-04

University of Washington

Abstract

The Assembly of Cluster Galaxies

by Vandana Desai

Chair of Supervisory Committee:

Professor Julianne J. Dalcanton
Astronomy

Clusters of galaxies are the largest bound structures in the universe. As such, they represent an important tool for testing models of structure formation. In addition, because galaxies in clusters span a range of local environments and experience the full spectrum of galaxy evolution pathways, clusters are ideal targets for investigations of galaxy evolution. This dissertation utilizes observations of clusters to study both structure formation and galaxy evolution. In Chapter 1, we use Sloan Digital Sky Survey data of low redshift clusters to test the results of numerical simulations of structure growth in a ΛCDM universe. Considering that the simulations follow the non-linear process of structure formation over several orders of magnitude in mass, we found a remarkable agreement between theory and observation. In Chapters 2, 3, and 4 we present results from a Hubble Space Telescope survey of 10 high redshift ($0.4 < z < 0.8$) galaxy clusters from the ESO Distant Cluster Survey. These data, in conjunction with data on lower-redshift clusters, show that 1) the fraction of elliptical galaxies varies between 15% and 55% but shows no systematic trend with redshift; 2) The S0 fraction has systematically increased at the expense of the late-type fraction since $z \sim 0.8$, strongly suggesting that late types have transformed into S0s within

clusters; 3) the morphology-density relation is already in place at $z \lesssim 0.8$; and 4) most ellipticals in clusters were assembled at $z \gtrsim 3$, not in dissipationless mergers of galaxies containing old stellar populations at $z < 1$.

TABLE OF CONTENTS

LIST OF FIGURES

LIST OF TABLES

ACKNOWLEDGMENTS

Many people contributed to both my growth as a scientist and to this dissertation. My strongest influences during my first two years of course work and qual studying were my entering class: Sean Matt, Darren Reed, and especially Ben Williams and Armin Rest. I thank them all for their collaboration, comraderie, and the ocassional games of hacky sack, beer-minton, and miniature golf on homemade courses. As I became more involved in research, my compadres in the research groups of Paul Hodge, Julianne Dalcanton, and Tom Quinn helped shape my understanding of the universe. Connie Rockosi, Anil Seth, Andrew West, and especially Beth Willman were outstanding sounding boards as I attempted to contribute to this understanding.

Without a doubt, my committee members and primary intellectual inflences, Julianne Dalcanton, Fabio Governato, and Tom Quinn can take a good share of credit for any scientific success that I may reap (but of course all mishaps are mine alone!). Each has contributed something unique to this dissertation and to me personally. It is difficult to articulate what these relationships have meant to me; suffice it to say that I am immensely grateful to have had them.

Finally, I cannot imagine how I would have accomplished this work (or anything good, really) without the companionship of my husband Noah. This is for him.

Chapter 1

THE CLUSTER GALAXY CIRCULAR VELOCITY FUNCTION

1.1 Abstract

We present galaxy circular velocity functions (GCVFs) for 34 low redshift ($z \lesssim 0.15$) clusters identified in the Sloan Digital Sky Survey (SDSS), for 15 clusters drawn from dark matter simulations of hierarchical structure growth in a ΛCDM cosmology, and for ~22,000 SDSS field galaxies. We find that the simulations successfully reproduce the shape, amplitude, and scatter in the observed distribution of cluster galaxy circular velocities. The power law slope of the observed cluster GCVF is ~-2.4, independent of cluster velocity dispersion. The average slope of the simulated GCVFs is somewhat steeper, although formally consistent given the errors. We find that the effects of baryons on galaxy rotation curves is to flatten the simulated cluster GCVF into better agreement with observations. The cumulative GCVFs of the simulated clusters are very similar across a wide range of cluster masses, provided individual subhalo circular velocities are scaled by the circular velocities of the parent cluster. The scatter is consistent with that measured in the cumulative, scaled observed cluster GCVF. Finally, the observed field GCVF deviates significantly from a power law, being flatter than the cluster GCVF at circular velocities less than 200 $\mathrm{km\,s^{-1}}$.

1.2 Introduction

In the widely accepted hierarchical clustering model of structure formation, adiabatic fluctuations in the initial density field grow and merge into increasingly larger dark matter halos. Simple inflationary approaches model the initial power spectrum of fluctuations as Gaussian and scale-invariant, while cosmological parameters and the nature of the dark matter control its subsequent evolution. The resulting mass function of dark matter halos can be predicted using N-body simulations (Sheth & Tormen, 1999; Bode et al., 2001; Jenkins et al., 2001; Reed et al., 2003) or analytic methods based upon Press-Schecter theory (Press & Schechter, 1974; Bond et al., 1991; Bower, 1991; Lacey & Cole, 1993; Sheth et al., 2001). The observed mass function is therefore an important constraint on fundamental properties of the universe. In the following, we focus on the mass function on galaxy scales.

Comparing predicted mass functions to observations requires mapping the observable properties of galaxies onto the masses of their dark matter halos. In one technique, semi-analytic models (SAMs) are used to predict the luminosities of galaxies within halos of different masses, by parametrizing models of the complicated processes of gas cooling, star formation, stellar evolution, and feedback. These techniques efficiently explore a wide variety of models. However, their utility is limited by the extent to which the simple recipes capture the relevant physics.

An alternative to SAMs utilizes the empirical relationship between velocities and luminosities in both spiral and elliptical galaxies to transform the observed galaxy luminosity function into a galaxy circular velocity function (GCVF), which is closely related to the mass function (Cole & Kaiser, 1989; Shimasaku, 1993; Gonzalez et al., 2000; Kochanek & White, 2001). While this approach avoids a number of assumptions required to assign luminosities to dark matter halos, baryons cannot be completely ignored. The baryonic mass distribution affects a galaxy's circular velocity profile significantly, while also changing the equilibrium configuration of the host dark matter halo through adiabatic contraction (Blumenthal et al., 1986). Baryons also determine the probability that a galaxy will be included in a given observational sample. However, the circular velocity directly traces the total enclosed mass of a galaxy, which is dominated by dark matter at sufficiently large radii. Therefore, models of the GCVF are less sensitive to inaccuracies in our understanding of star formation, stellar evolution, and feedback than those of the luminosity function. The observed GCVF therefore better constrains the mass function.

Recent comparisons between observed and theoretical field GCVFs indicate that low-mass halos with circular velocities $\lesssim 200\,\mathrm{km\,s^{-1}}$ are over-predicted by simulations (Gonzalez et al., 2000; Kochanek & White, 2001). It is now possible to extend the analysis of the GCVF to galaxies within clusters. The current generation of N-body simulations (Ghigna et al., 1998; Tormen et al., 1998; Klypin et al., 1999; Okamoto & Habe, 2000; Springel et al., 2001) has achieved the force and mass resolution necessary to capture the effects of tidal stripping, dynamical friction, and galaxy harassment, essential for predicting the GCVF in dense environments. Moore et al. (1999) used the Tully-Fisher relation to determine circular velocities for galaxies in the Virgo Cluster. They compared the resulting distribution to that in a standard CDM simulation of a Virgo-like cluster, and found good agreement down to $\sim$50 $\mathrm{km\,s^{-1}}$ without accounting for the effects of baryons on galaxy rotation curves. Coupling dark matter merging trees with SAMs which include strong feedback, Springel et al. (2001) were able to reproduce a wide variety of cluster properties. Although they did not directly compute the cluster GCVF, the agreement between a variety of observed and modeled cluster relations (morphology-density, luminosity function, Tully-Fisher, Faber Jackson) suggests that they would have found agreement for the cluster GCVF as well. Although these works represent significant progress in testing simulations of cluster substructure against observations, larger samples of both simulations and observations are required to assess whether the results are typical, and over what cluster mass range.

In order to test the predicted abundance of cluster galaxies as a function of circular velocity, we determined the GCVFs for 34 nearby clusters from the Sloan Digital Sky Survey (SDSS) and for 15 simulated clusters. To allow a comparison to the field, we also estimated the GCVF from ~22,000 SDSS field galaxies.

We first describe the SDSS data in §1.3 and our cluster sample in §1.4. Our method for determining the GCVFs for the SDSS sample is described in §1.5. In §1.6 we describe the simulations. Our results are discussed in §1.7. First we discuss the shape of the cluster GCVF as related to that of the cluster luminosity function (§1.7.1). Second, we investigate the claim of Moore et al. (1999) that the velocity distribution of substructure on all mass scales is self-similar when scaled by the host halo velocity (§1.7.2). Third, we present power-law fits to the cluster GCVF, quantify its dependence on cluster velocity dispersion, and make a comparison to dark matter cluster simulations (§1.7.3). Fourth, we examine how the adiabatic contraction of dark matter halos due to baryons affects the comparison between observed and simulated GCVFs (§1.7.4). Finally, we compare the observed cluster GCVF to that measured for the field (§1.7.5). A summary of our results can be found in §1.8.

Throughout we adopt $H_0 = 70\,\mathrm{km\,s^{-1}Mpc^{-1}}$, $\Lambda = 0.7$, and $\Omega = 0.3$.

1.3 The Sloan Digital Sky Survey

We took advantage of the large-scale, homogeneous spectroscopy and photometry of the Sloan Digital Sky Survey (SDSS) in order to study the cluster and field GCVF. The SDSS (York et al., 2000) is a photometric and spectroscopic survey being carried out at the Apache Point Observatory using a 2.5-m telescope equipped with modern CCD detectors (Gunn et al., 1998). This ambitious project will eventually cover the Northern Galactic Hemisphere, almost one quarter of the sky. The photometric survey provides nearly simultaneous imaging in five passbands (u, g, r, i, z; Fukugita et al., 1996). The spectroscopic survey consists of medium resolution ($\lambda/\Delta\lambda = 2000$)

spectra of galaxies, quasars, and stars selected systematically from the photometric catalogs.

The first public release of SDSS data occurred in June 2001, and is known as the Early Data Release (EDR; Stoughton et al., 2002). The EDR consists of imaging data covering approximately 460 square degrees of sky, as well as approximately 55,000 spectra.

The photometric and spectroscopic pipelines (Lupton et al., 2001; Stoughton et al., 2002) measure numerous quantities that are available as part of the EDR. Below we describe only those which will be used in the present analysis. Note that because the photometric system has yet to be finalized, we denote the current, temporary magnitudes with asterisks, while references to the bandpasses remain simply italicized.

The photometric pipeline computes two types of magnitudes appropriate for use on galaxies: model and Petrosian. To compute model magnitudes, the photometric pipeline fits a pure de Vaucouleurs profile and a pure exponential profile to the two dimensional r image of each galaxy. The best-fitting model is then applied, up to an amplitude change, to images in the other bands. All fits account for the effects of local seeing. A bug in the version of the SDSS photometric pipeline used in the EDR causes the model magnitudes of bright galaxies to be $\sim$0.2 magnitudes too bright. The inverse Fundamental Plane relation we use to estimate the circular velocities of early type galaxies (§1.5.1) was calibrated using model magnitudes afflicted by the same bug. For consistency with this calibration, we use parameters derived from the de Vaucouleurs fits to derive circular velocities for early type galaxies. Specifically, we use m_{deV}, the total apparent magnitude; r_{deV}, half the length of the major axis of the ellipse that encloses half the light of the galaxy; and q_{deV}, the minor-to-major axis ratio.

The inverse Tully-Fisher relation we applied to late type galaxies (1.5.1) was calibrated using magnitudes extrapolated to infinity assuming exponential surface brightness profiles. Correctly-calculated model magnitudes would be the optimal choice for consistency with this calibration. In their absence, we use Petrosian magnitudes ($m_{\rm pet}$) for late type galaxies. Petrosian magnitudes attempt to measure a constant fraction of the total light of a galaxy, independent of surface brightness, distance, or photometric model. The Petrosian radius is computed in the r band, and Petrosian magnitudes in all bands are based upon the amount of flux within two Petrosian radii. To estimate the extinction within late type galaxies, we additionaly use $q_{\rm exp}$, the minor-to-major axis ratio of the best-fitting exponential model.

Also available from the SDSS database are galactic extinction corrections as functions of position based upon Schlegel et al. (1998). All magnitudes in the remainder of this paper refer to reddening-corrected values.

For the computation of the field GCVF (§1.7.5), we use only galaxies with known redshifts. The SDSS spectroscopic pipeline determines both an emission and cross-correlation redshift. We use the redshift with the highest confidence interval.

1.4 Cluster Sample

Several cluster catalogs have been constructed from SDSS data, using a variety of identification algorithms (Bahcall et al., 2003). In order to compute accurate GCVFs down to the lowest possible circular velocities, we used the nearest clusters which had many spectroscopically-confirmed members. Miller et al., 2004 (in prep) have identified 62 clusters in the Equatorial Stripes of the SDSS using the C4 algorithm (Nichol et al., 2001; Gómez et al., 2003). This algorithm uses the observed phenomenon that galaxies in clusters have similar colors as well as locations. For each galaxy, the algorithm determines the number of neighbors in the seven-dimensional space spanning right ascension, declination, redshift, and the four SDSS colors. This number of neighbors is compared to the distribution found for 100 random field galaxies. Based upon this comparison, the probability that the galaxy is a field galaxy is computed. Galaxies that are probably not field galaxies are identified using the False Discovery

Table 1.1 Galaxy Cluster Sample

RA (J2000) h:m:s	DEC (J2000) °:′:″	z	$\sigma_{\rm cl}$ km s^{-1}	$\Delta\sigma_{\rm cl}$ km s^{-1}	$R_{\rm vir}$ Mpc	$V_{\rm compl}$ km s^{-1}	$\log_{10} N_{200}$	$\Delta \log_{10} N_{200}$	β	$\Delta\beta$	$\log_{10} N'_{200}$	$\Delta \log_{10} N'_{200}$
00:21:40.841	-00:55:34.17	0.105	370	71	0.77	65	-0.49	0.07	-1.46	0.33	-0.80	0.04
00:23:31.152	-00:48:10.08	0.063	540	97	1.20	48	-0.94	0.12	-3.10	0.49	-0.88	0.05
00:29:14.952	-00:08:42.36	0.060	716	109	1.59	47	-0.59	0.06	-3.20	0.27	-0.52	0.04
00:46:15.528	00:09:08.64	0.114	582	74	1.20	73	-0.81	0.11	-2.20	0.47	-0.95	0.06
00:47:20.400	-00:53:37.15	0.117	660	117	1.36	74	-0.39	0.05	-2.34	0.22	-0.50	0.03
00:56:00.120	00:37:56.74	0.067	557	81	1.23	49	-0.88	0.10	-3.81	0.39	-0.65	0.03
00:57:25.752	-00:31:12.00	0.044	465	40	1.06	37	-0.71	0.06	-2.17	0.18	-0.95	0.02
01:15:08.784	00:15:56.88	0.045	599	44	1.36	38	-0.53	0.04	-2.31	0.13	-0.69	0.03
01:16:39.816	00:37:25.68	0.044	601	48	1.37	37	-1.14	0.14	-3.23	0.35	-0.95	0.02
01:31:08.928	00:31:23.52	0.079	533	64	1.15	55	-0.66	0.08	-2.58	0.33	-0.73	0.04
01:34:49.824	-00:36:39.24	0.081	553	81	1.19	56	-0.74	0.11	-1.33	0.58	-0.99	0.11
01:37:25.704	-00:28:08.40	0.056	432	123	0.97	44	-1.03	0.19	-2.02	0.79	-1.22	0.08
02:02:15.600	-00:56:36.96	0.042	310	44	0.71	37	-1.02	0.08	-3.08	0.20	-0.90	0.01
03:06:17.376	-00:08:34.80	0.109	585	56	1.22	68	-0.68	0.08	-2.20	0.34	-0.83	0.06
03:26:23.232	-00:38:51.72	0.037	324	56	0.74	34	-1.12	0.14	-2.43	0.34	-1.27	0.01
10:07:55.441	00:35:29.04	0.097	493	49	1.04	64	-0.51	0.05	-1.83	0.22	-0.71	0.04
10:23:32.161	00:10:25.32	0.095	526	73	1.11	62	-0.75	0.19	-1.52	1.13	-1.23	0.12
10:49:15.839	00:57:15.84	0.106	474	78	0.99	67	-0.69	0.09	-1.63	0.40	-1.01	0.04
10:50:04.559	00:21:06.12	0.039	281	31	0.64	34	-0.93	0.12	-1.78	0.32	-1.36	0.01
12:46:54.240	00:18:31.32	0.089	844	89	1.80	62	-0.50	0.06	-2.50	0.28	-0.58	0.06
12:47:43.440	-00:09:07.20	0.088	994	102	2.13	61	-0.69	0.10	-3.04	0.45	-0.67	0.10
13:19:14.641	-00:53:58.20	0.083	704	73	1.52	58	-0.41	0.04	-3.34	0.15	-0.30	0.02
13:21:18.241	-00:44:19.32	0.108	873	131	1.82	70	-0.50	0.07	-2.78	0.33	-0.54	0.06
13:24:22.321	00:46:55.92	0.108	575	129	1.20	70	-0.95	0.12	-3.85	0.46	-0.75	0.04
13:45:05.760	00:13:55.20	0.089	284	43	0.61	63	-0.92	0.14	-2.97	0.54	-0.88	0.04
13:45:15.601	-00:08:30.84	0.088	362	42	0.77	60	-1.26	0.26	-3.27	1.00	-1.15	0.08
14:14:41.279	-00:24:20.44	0.137	761	80	1.52	80	-0.02	0.02	-2.04	0.16	-0.07	0.03
14:15:05.039	-00:29:08.16	0.141	930	113	1.85	83	-0.07	0.02	-2.11	0.22	-0.10	0.04
14:29:36.962	00;24:36.00	0.055	281	36	0.63	44	-0.96	0.14	-1.42	0.39	-1.52	0.04
15:08:31.919	-00:16:03.00	0.090	737	61	1.57	63	-0.40	0.05	-2.11	0.25	-0.51	0.05
15:11:19.918	-00:02:26.16	0.091	455	49	0.97	62	-0.59	0.06	-1.71	0.27	-0.75	0.07
15:16:23.522	00:06:09.00	0.119	675	120	1.39	75	-0.37	0.04	-1.62	0.19	-0.51	0.06
15:17:25.920	-00:38:24.36	0.116	758	92	1.56	75	-0.17	0.03	-2.52	0.12	-0.22	0.02
15:29:12.719	-00:15:07.92	0.087	459	54	0.98	59	-0.61	0.07	-2.41	0.27	-0.74	0.04

Rate thresholding technique (Miller et al., 2001). In order to create as large a sample as possible, we supplemented the C4 clusters with 51 nearby NED[1] clusters in the same area, of which 18 were duplicates.

In order to compare our observed GCVFs to each other and to models, we calculated them within a consistent aperture. The virial radius, R_{vir}, is a natural aperture to select. Girardi & Mezzetti (2001) present the following empirical expression for R_{vir}, the radius within which the average density is equal to $\Delta \sim 200$ times the critical density:

$$R_{\mathrm{vir}} \sim \frac{0.0017\sigma}{(1+z)^{3/2}} \ \ (\mathrm{km}^{-1}\ \mathrm{s}\ h_{100}^{-1}\ \mathrm{Mpc}). \tag{1.1}$$

Here σ_{cl} is the line-of-sight cluster velocity dispersion, which is straightforward to measure. First, we selected all galaxies with spectroscopic redshifts within a radius of either 1.5 Mpc or the largest radius allowed by the extent of the data, whichever was smaller. Galaxies were then ordered by recessional velocity, and gaps larger than 800 $\mathrm{km\,s^{-1}}$ were used to remove interlopers. A robust weighted gap estimator (Beers et al., 1990) was used to determine σ_{cl} from the remaining velocities. This process was performed iteratively until the velocity dispersion stabilized. The resulting velocity dispersion was divided by a factor of $(1+z)$ to correct it to the cluster frame (Danese et al., 1980). Errors were estimated using bootstrap re-sampling, and are typically 10–20 per cent.

In order to ensure accurate estimates of σ_{cl}, we rejected 36 clusters with fewer than 20 confirmed members. Five clusters with virial radii which extend beyond the SDSS data limits were also eliminated from the sample. We did not include an additional 20 clusters with data defects or that were not rich enough to yield high signal-to-noise GCVFs. The remaining sample of 34 clusters are listed in Table 1.1. The velocity

---

[1] The NASA/IPAC Extragalactic Database (NED) is operated by the Jet Propulsion Laboratory, California Institute of Technology, under contract with the National Aeronautics and Space Administration.

dispersions and errors for each cluster can be found in columns 4 and 5, and the bottom panel of Figure 1.2 shows the distribution of $\sigma_{\rm cl}$. Virial radii computed from Equation 1.1 are listed in column 6 of Table 1.1.

1.5 *Construction of the Observed Cluster Galaxy Circular Velocity Function*

In this section, we describe the construction of the GCVF for each cluster in the sample described in §1.4, including the determination of circular velocities for late and early type galaxies, the completeness velocities of the resulting GCVFs, our background substraction procedure, and possible sources of error.

1.5.1 Determination of Galaxy Circular Velocities

Each galaxy within $\rm R_{vir}$ and with $r^* < 21.5$ (the star/galaxy separation limit; Lupton et al., 2001) is given the designation of Early (E, S0, Sa) or Late (Sb, Sc, Irr) type. Strateva et al. (2001) find that $u^* - r^* < 2.22$ is optimal for separating these classes. For selecting early types, the completeness is 68 per cent, while the reliability is 81 per cent. For selecting late types, the completeness is 77 per cent, and the reliability is 96 per cent. We then translated the surface photometry of each galaxy into a circular velocity using the conversions described in the following two subsections.

Late Type Galaxies

Disk galaxies exhibit a tight correlation between luminosity and circular velocity. The Tully-Fisher relation (TFR) allows one to compute the former given the latter. We require the inverse TFR, which converts from luminosity to circular velocity. Neither the TFR nor the inverse TFR have been calibrated in SDSS passbands. We therefore follow Sheth et al. (2003) in adopting the inverse I-band relation presented by Giovanelli et al. (1997) for 360 spiral galaxies deemed to be members of 24 clusters (their "in" sample). Although it was calibrated using cluster data, we applied the following relationship to late type galaxies in the determination of both the field and cluster GCVFs:

$$\log_{10}(2V_c) - 2.5 = -\frac{21.10}{7.94} - \frac{(M_I - 5\log_{10} h_{100})}{7.94}, \tag{1.2}$$

where M_I is the k-corrected, extinction-corrected I-band absolute magnitude, extrapolated to infinity assuming an exponential surface brightness profile; and V_c is an estimate of the maximum rotational velocity of a galaxy. Although disk galaxy rotation curves exhibit a variety of shapes, the circular velocity generally increases with radius until it reaches a broad peak at ~10 kpc, beyond which it remains relatively constant. Thus V_c should be similar to the circular velocity measured at the flat part of the rotation curve.

In order to convert the observed SDSS magnitudes into those upon which the TFR is based, we first computed the r-band absolute total magnitude of each late type galaxy:

$$M_{\mathrm{pet},r} = m_{\mathrm{pet},r} - 5\log d_L(z) + 5 - K(z), \tag{1.3}$$

where $m_{\mathrm{pet},r}$ is the apparent r-band Petrosian magnitude, d_L is the luminosity distance in parsecs, and $K(z)$ is the k-correction, computed using KCORRECT V1_11 (Blanton et al., 2003). We then used the conversion from Fukugita et al. (1995) for late type galaxies: $M_{\mathrm{pet},r} - M_I \sim 0.9$.

Internal extinction corrections were estimated using the procedure of Tully & Fouque (1985):

$$A = -2.5\log\left[f\left(1+e^{-a}\right) + (1-2f)\left(\frac{1-e^{-a}}{a}\right)\right], \tag{1.4}$$

where $f = 0.1$ is the fraction of stars homogeneously mixed with a dust layer having opacity $\tau = 0.28$; $a = \tau \sec i$; and i is the inclination, estimated as:

$$\cos^2(i) = \frac{q_{\rm exp}^2 - q_0^2}{1 - q_0^2}. \qquad (1.5)$$

Here $q_0 = 0.20$ is the intrinsic thickness and $q_{\rm exp}$ is the r-band axis ratio determined from the best-fitting exponential model. The extinction is considered to be constant for $i > 80°$.

The internal extinction corrections were on the order of ~0.3 magnitudes.

Early Type Galaxies

Early type galaxies occupy a thin plane in the space defined by stellar velocity dispersion, physical size, and surface brightness. Given the velocity dispersion and surface brightness, one can use the Fundamental Plane relation (FP; Djorgovski & Davis (1987); Dressler et al. (1987)) to estimate the size. In order to construct the GCVF from SDSS photometry, we required a relation that yields the velocity dispersion (which is simply related to the circular velocity) given a size and surface brightness.

In a series of three papers, Bernardi and collaborators constructed a sample of ~9000 SDSS early type galaxies, from which they computed the joint distributions of $\sigma_{\rm los}$, the line-of-sight velocity dispersion measured through a circular aperture with a radius equal to one-eighth the half-light radius; I_0, the average surface brightness within the half-light radius; and R_0, the half-light radius in kpc (Bernardi et al.2003a,b,c). In order to determine the coefficients of the FP relation, they used the above joint distributions to minimize the sum of $\Delta_{FP}^2 = (\log_{10} R_0 - a\log_{10}\sigma_{\rm los} - b\log_{10} I_0 - c)^2$ over all galaxies in their sample. In order to compute the coefficients for the inverse FP relation,

$$\log_{10}\sigma_{\rm los} = a'\log_{10} R_0 + b'\log_{10} I_0 + c', \qquad (1.6)$$

we used the same distributions to minimize the sum of

$$\Delta^2_{\mathrm{invFP}} = (\log_{10}\sigma_{\mathrm{los}} - a'\log_{10}R_0 - b'\log_{10}I_0 - c')^2 \tag{1.7}$$

over all galaxies. Using their sample, we found $a' = 0.597$, $b' = 0.447$, and $c' = 5.449$.

For each early type galaxy, we estimated σ_{los} using Equation 1.6. Our method for computing R_0 and I_0 was identical to that adopted for the calibration sample. In determining R_0, the physical characteristic size, we first measured the angular characteristic size for each galaxy, $r_0 = r_{\mathrm{deV}}\sqrt{q_{\mathrm{deV}}}$. Because the inverse FP that we used was calibrated against galaxies at a variety of redshifts, the angular sizes measured in each band were linearly interpolated in order to determine the angular size at a rest wavelength corresponding to the central wavelength of each filter.

To determine I_0, we used the relation $\mu_0 = -2.5\log I_0$, where

$$\mu_0 = M_{\mathrm{deV},r} + 2.5\log(2\pi r_0^2) - K(z) - 10\log(1+z). \tag{1.8}$$

Here $M_{\mathrm{deV},r}$ refers to the deVaucouleurs model magnitude, and K(z) is as previously defined.

In order to plot early type galaxies on the same velocity scale as late types, we converted σ_{los} to V_{c}. Fitting non-parametric, spherical models to line profile and radial velocity dispersion data for 21 elliptical galaxies, Kronawitter et al. (2000) found that the circular velocity profiles of elliptical galaxies are flat to the 10 per cent level outside a radius of 0.3 effective radii. Gerhard et al. (2001) showed that there is a tight relation between the circular velocities in the flat regions of the rotation curves and the central velocity dispersions for these ellipticals. Ferrarese (2002) examined this relation, taking central velocity dispersions from Davies et al. (1987) and correcting them to an aperture of one-eighth the effective radius to find a relation between $\log_{10}V_{\mathrm{c}}$ and $\log_{10}\sigma_{\mathrm{los}}$. Using the same data as Ferrarese (2002), we found that the isothermal assumption ($V_{\mathrm{c}} = \sqrt{2}\sigma_{\mathrm{los}}$) systematically underpredicts V_{c}, but that the data are consistent with the following relation, which we use to determine V_{c}:

$$V_{\mathrm{c}} \approx 1.54\sigma_{\mathrm{los}}. \tag{1.9}$$

1.5.2 Completeness

Because our procedure distinguishes between morphological types, we could assign different values of V_{c} to galaxies of the same luminosity. Our requirement that $r^{*} < 21.5$ therefore leads to a cut in V_{c} that depends on both redshift and galaxy type. Figure 1.1 illustrates the effect our magnitude limit has on V_{c} for a representative cluster. The filled points represent early type galaxies, while the hollow points represent late type galaxies. For this cluster, 90 per cent of galaxies with $21 < \mathrm{r}^{*} < 21.5$ have $V_{\mathrm{c}} > 82\ \mathrm{km\,s^{-1}}$. Below this completeness velocity, V_{compl}, significant numbers of galaxies are missing from our sample. All GCVFs in what follows are truncated below V_{compl}, which was calculated independently for each cluster. The adopted values are listed in Table 1.1, column 7.

1.5.3 Background Subtraction

Because a spectrum is not available for every galaxy in the field of each cluster, our background subtraction is statistical. We calculated the circular velocity for every galaxy within the virial radius of each cluster under the assumption that it lies at the cluster redshift. Clearly, some galaxies have redshifts greater or less than that of the cluster, and our calculations were incorrect for these galaxies. This effect was removed during our background subtraction procedure. Again using the cluster redshift, we calculated the circular velocity for every galaxy within an annulus bounded by inner and outer radii of 3 and 5 Mpc, respectively. These galaxies should have a redshift distribution similar to that of the cluster interlopers. Thus, by subtracting the appropriately normalized GCVF of galaxies in the annulus, we corrected for the interlopers.

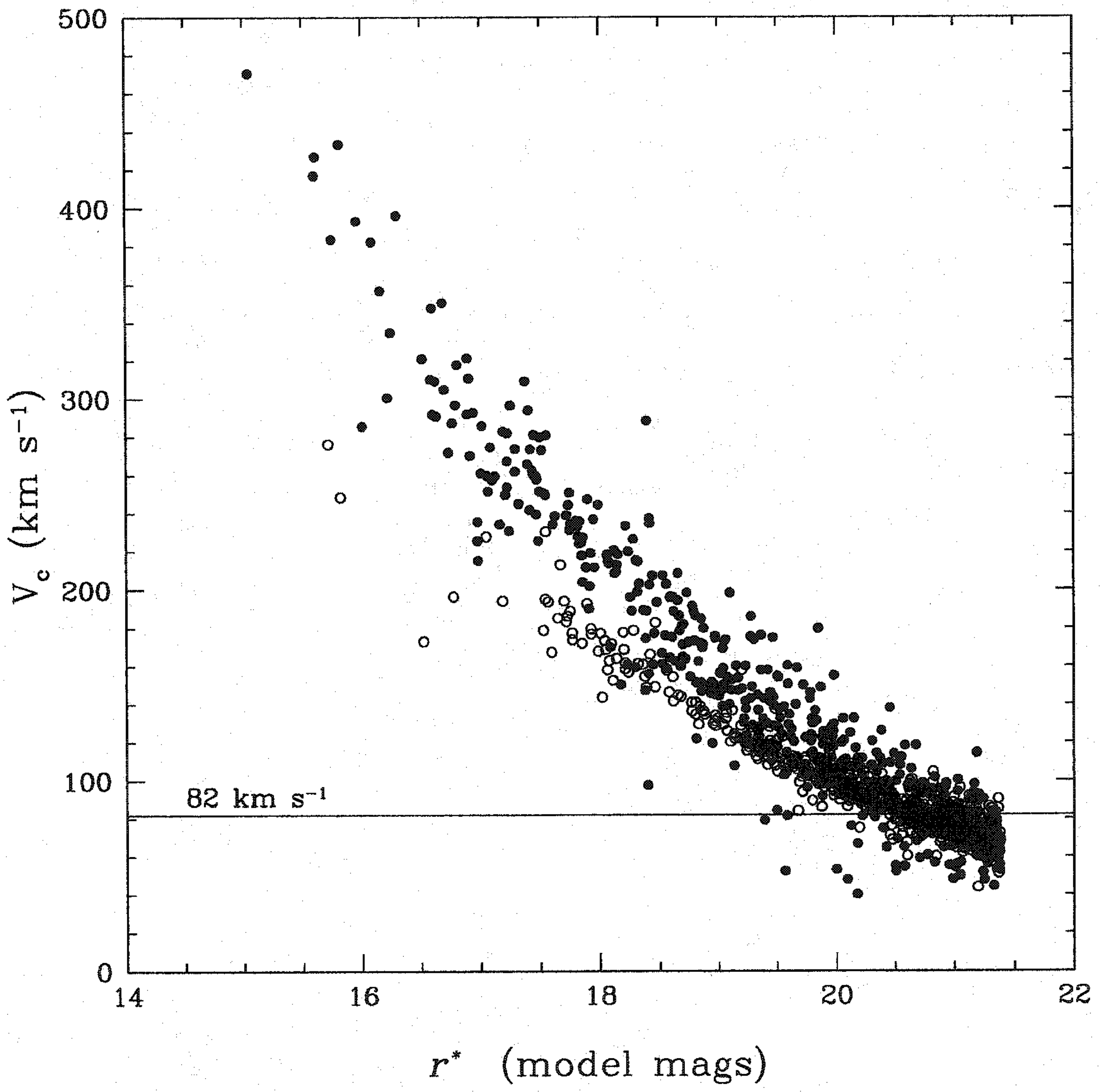

Figure 1.1 Illustration of the completeness limit for one cluster in our sample. Each point represents a galaxy within $R_{\rm vir}$ for a representative cluster in our SDSS sample. No background subtraction has been carried out. Filled circles are early type galaxies, and hollow circles denote late type galaxies. Ninety per cent of all galaxies with $21 > r^* > 21.5$ lie below the completeness velocity of $V_{\rm compl} = 82\,{\rm km\,s^{-1}}$ for this cluster.

The uncertainty in the number of galaxies in each circular velocity bin is calculated assuming Poisson statistics hold for both the total counts within the virial radius, $C_{\rm tot}$, and the counts within the background annulus, $C_{\rm background}$:

$$\sigma_N^2 = C_{\rm tot} + f^2 C_{\rm background}, \tag{1.10}$$

where f is the normalization factor applied to the background annulus counts to account for the difference in its area and that of the virialized part of the cluster ($0.02 \lesssim f \lesssim 0.3$).

The contribution to the total error from Poisson noise in the background counts decreases with increasing $V_{\rm c}$. Above ~200 $\rm km\,s^{-1}$, the contribution is less than 40 per cent.

1.5.4 Errors

As described in the previous subsection, the error bars for individual GCVFs are computed from the Poisson statistics associated with the background subtraction. While these are the major source of random errors in our analysis, in this section we consider important systematics.

The largest source of systematic errors is the scatter around the mean inverse Fundamental Plane (§1.5.1) and Tully Fisher (§1.5.1) relations, which we have used to estimate circular velocities from photometric parameters. Sheth et al. (2003) have shown that if the scatter is significant, the use of mean relations can significantly distort the shape of the GCVF. Therefore, in constructing our GCVFs, we accounted for the scatter by representing each galaxy's $V_{\rm c}$ as a probability distribution, rather than a single value. Because we calculated $V_{\rm c}$ using different relations for early and late type galaxies, this distribution depends on galaxy type.

The circular velocities for late type galaxies were computed directly from the inverse TFR (§1.5.1). We therefore adopted the model for the scatter around $V_{\rm c}$

provided by Giovanelli et al. (1997).

$$< \Delta^2_{\mathrm{invTF}} >= \frac{(-0.28(\log_{10}(2V_{\mathrm{c}}) - 2.5) + 0.26)^2}{63.04}. \qquad (1.11)$$

The circular velocities for early type galaxies were computed using Equations 1.6 and 1.9. Galaxies scatter around both of these mean relations. We estimated the scatter in the former by exchanging V and R in the expression for $< \Delta_1^2 >$ in Equation 4 of Bernardi et al. (2003) and using the joint distributions of σ_{los}, R_0, and I_0 presented in their Table 1. Doing so yielded a scatter of $< \Delta^2_{\mathrm{invFP}} >= 0.061$ in $\log_{10} \sigma_{\mathrm{los}}$. Sheth et al. (2003) found that the scatter in $\log_{10} \sigma_{\mathrm{los}}$ depends slightly on $\log_{10} \sigma_{\mathrm{los}}$. This was a small effect compared to our other sources of error; we therefore treated the scatter in the Fundamental Plane as constant. The conversion from σ_{los} to V_{c} (Equation 1.9) was calibrated on only $\sim$20 elliptical galaxies. Therefore a robust model of the scatter due to this conversion was not possible and we neglected it. Because the Fundamental Plane and Tully-Fisher relations were calibrated using samples created under more stringent selection criteria than we used, the above relations underestimate the scatter that exists in our data.

In addition to the fact that a range of velocities correspond to a given set of photometric parameters, our knowledge of photometric parameters is uncertain due to measurement errors. Our precision in determining velocities from the inverse TFR is limited by errors in measuring m_{pet} and q_{exp}. These errors are greatest for galaxies with low circular velocities. Ninety percent of galaxies in the lowest V_{c} bins have fractional uncertainties in the circular velocity of $\sigma_{V_{\mathrm{c}}}/V_{\mathrm{c}} < 0.1$. This is smaller than the binsize we have used. The error in measuring R_0 dominates the random uncertainty in calculating V_{c} for early type galaxies using the Fundamental Plane relation. Again, the magnitude of this error is greatest for galaxies with low circular velocities. Near the completeness limit, these errors become comparable to the binsize.

Because the PSF modeling was inaccurate in the EDR, one might suspect that the structural parameters q_{exp} (used to calculate the extinction correction for late type galaxies) and R_0 (used in the Fundamental Plane Relation for early type galaxies) suffer from systematic errors in addition to random errors. This deficiency in the EDR data has been corrected for the second data release (DR2), and the alorithm has been extensively tested with simulations (Abazajian et al., in prep). Therefore, in order to assess the magnitude of the systematics in the values of $q_{\rm exp}$ in the EDR catalog, we compared them with values found in the DR2 catalog. For 98 per cent of the ~5000 galaxies we tested, the axial ratios were consistent within the errors. Out of the 2 per cent of galaxies that showed a statistically significant difference in $q_{\rm exp}$ between reductions, only 20 per cent (less than 0.5 per cent of the whole sample) showed differences strong enough to result in errors in the extinction correction of greater than 0.2 magnitudes, which corresponds to a 6 per cent change in circular velocity. These errors are very small in comparison to the binsize, and we therefore neglect them. For early type galaxies, the situation is much simpler: because any systematics in R_0 also exist in the data used to calibrate the Fundamental Plane, they do not affect this work.

1.6 Methods: Simulations

In order to compare our observational results against simulations, we compiled a set of 15 simulations of the dark matter components of clusters. Each simulated cluster was evolved in the currently favored ΛCDM cosmology with Λ=0.7, $H_0 = 70$ $\rm km\,s^{-1}\,Mpc^{-1}$, $\Omega_0 = 0.3$, and $\sigma_8 = 1$. Ten are the most massive clusters from the zero redshift output of the $50^3\ h_{100}^{-3}\ \rm Mpc^3$ simulation described in Reed et al. (2003). This simulation has a particle mass of $1.9\times10^8 M_\odot$ and a force resolution of 7.14 kpc. An additional four clusters were simulated using the volume renormalization technique (Katz & White, 1993) and have $(0.5\text{-}0.9)\times10^5$ particles within the virial radius and force softenings of $\lesssim 1$ per cent of the virial radius. Further details on these four simulations can be found in Borgani et al. (2002).

Table 1.2 Simulation Sample

Run	$\sigma_{\rm cl}$	M$_{200}$	R$_{200}$	m$_{DM}$	N$_{DM}$	ϵ
	km s^{-1}	$10^{13} M_\odot$	h_{70} Mpc	$10^8 M_\odot$	10^6	kpc
Box01	525	29.4	1.73	1.9	1.5	7.14
Box02	458	26.6	1.67	1.9	1.4	7.14
Box03	383	21.7	1.56	1.9	1.1	7.14
Box04	456	18.4	1.48	1.9	0.97	7.14
Box05	451	17.9	1.46	1.9	0.94	7.14
Box06	342	15.4	1.39	1.9	0.81	7.14
Box07	388	13.0	1.32	1.9	0.68	7.14
Box08	332	11.6	1.27	1.9	0.61	7.14
Box08	369	10.3	1.22	1.9	0.54	7.14
Box10	366	8.9	1.26	1.9	0.47	7.14
Hickson	234	2.5	0.76	4.41	0.0486	2.5
Fornax	400	5.9	0.65	4.41	0.118	2.5
Virgo	565	30.4	1.75	14.9	0.179	1.25
Coma	1007	133.6	2.86	119.2	0.090	3.75
HR Virgo	600	30	1.75	3	1.00	1.25

Further details on the simulated clusters named Box01 – Box10 can be found in Reed et al. (2003). The simulations labelled Hickson, Fornax, Virgo, and Coma are described in Borgani et al. (2002). *Columns:* $\sigma_{\rm cl}$ is the velocity dispersion of the simulated cluster, R_{200} is the radius within which the average density is 200 times the critical density, M_{200} is the mass within R_{200}, m_{DM} is the mass of each dark matter particle, N_{DM} is the number of dark matter particles within R_{200}, and ϵ is the force softening.

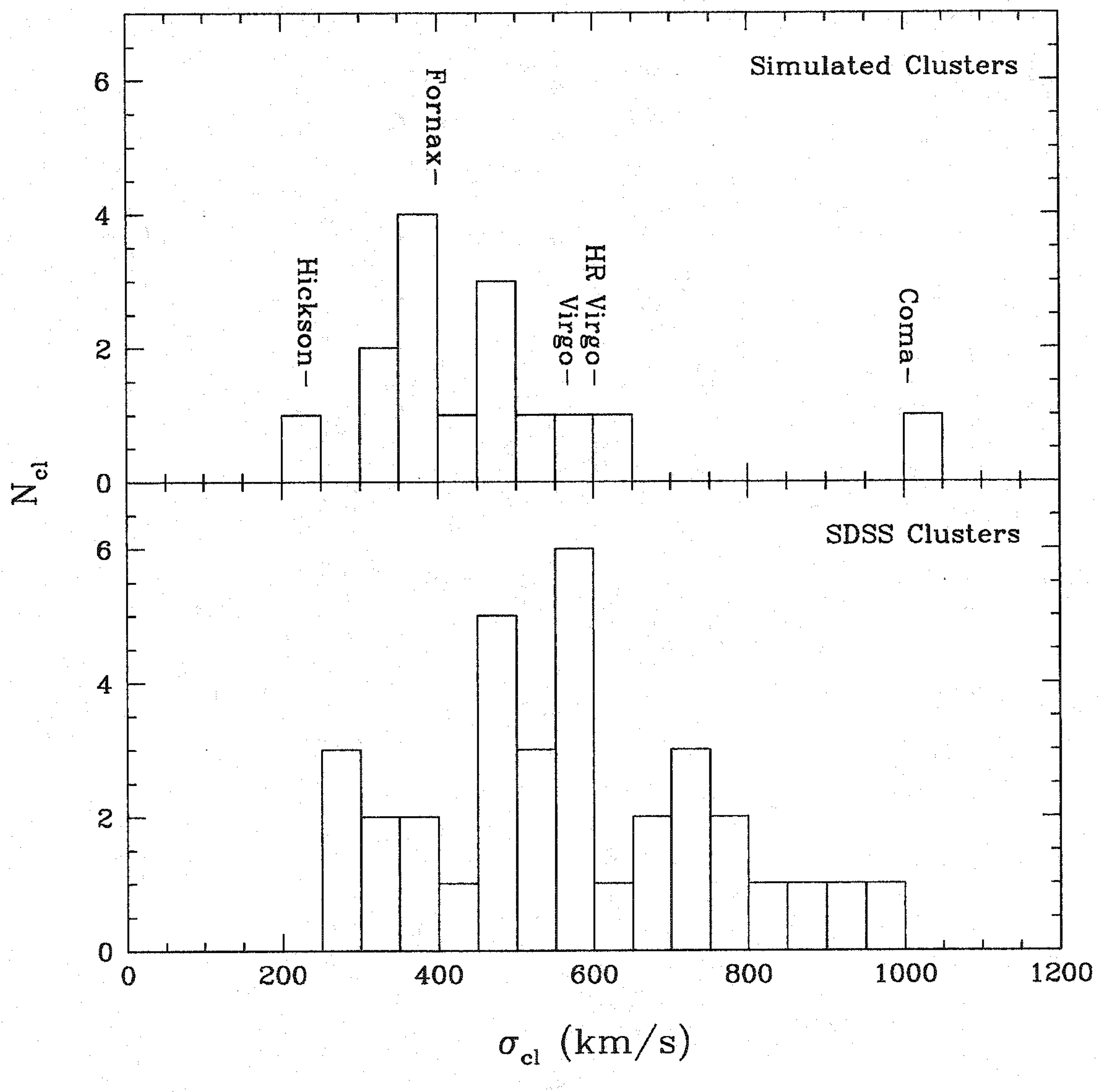

Figure 1.2 *Top Panel:* The distribution of cluster velocity dispersions for the 15 simulations described in §1.6. *Bottom Panel:* The distribution of cluster velocity dispersions, calculated by the methods described in §1.4, for our sample of 34 SDSS clusters.

The 14 cluster simulations were of sufficient resolution to robustly determine peak circular velocities in subhalos above the completeness velocities of our observed GCVFs (see §1.5.2 and Table 1.1). They were of insufficient resolution, however, to accurately trace subhalo internal density profiles. These were necessary to determine the effects of baryons on galaxy rotation curves, as we describe in §1.7.4. For this purpose, we used a very high resolution N-body simulation of a galaxy cluster with $\sigma_{\rm cl} = 600\,{\rm km\,s^{-1}}$ and $M_{\rm vir} = 3 \times 10^{14} M_{\odot}$, represented by approximately one million particles within $R_{\rm vir} = 1.75$ Mpc. It was evolved in a 100^3 Mpc^3 volume where the force spline softening was 1.25 kpc and the large scale structure was sampled at a lower resolution.

Subhalos were identified using SKID (Stadel, 2001; Governato et al., 1997), a halo finder based on local density maxima and particulary suited to finding subhalos within larger structures. Peak circular velocities were also output by SKID. We used `Tipsy`[2] to extract full density profiles from our highest resolution simulation.

1.7 Results

1.7.1 The Shape of the GCVF

A Press-Schechter mass function combined with $M \propto V^3$ and a value of $n = 2$ for the fluctuation-spectrum index gives

$$\frac{dN\left(V_{\rm pk}\right)}{dV_{\rm pk}} \propto V_{\rm pk}^{-4}. \tag{1.12}$$

Moore et al. (1999) and Ghigna et al. (2000) found the GCVF in a high resolution simulation of a Virgo-like cluster to be consistent with the above power law. Moore et al. (1999) also found the observed GCVF of Virgo to be consistent with it. In Figure 1.3 we plot the GCVFs for our sample of 34 clusters in three cluster velocity

---

[2] `http://www-hpcc.astro.washington.edu/tools/tipsy/tipsy.html`

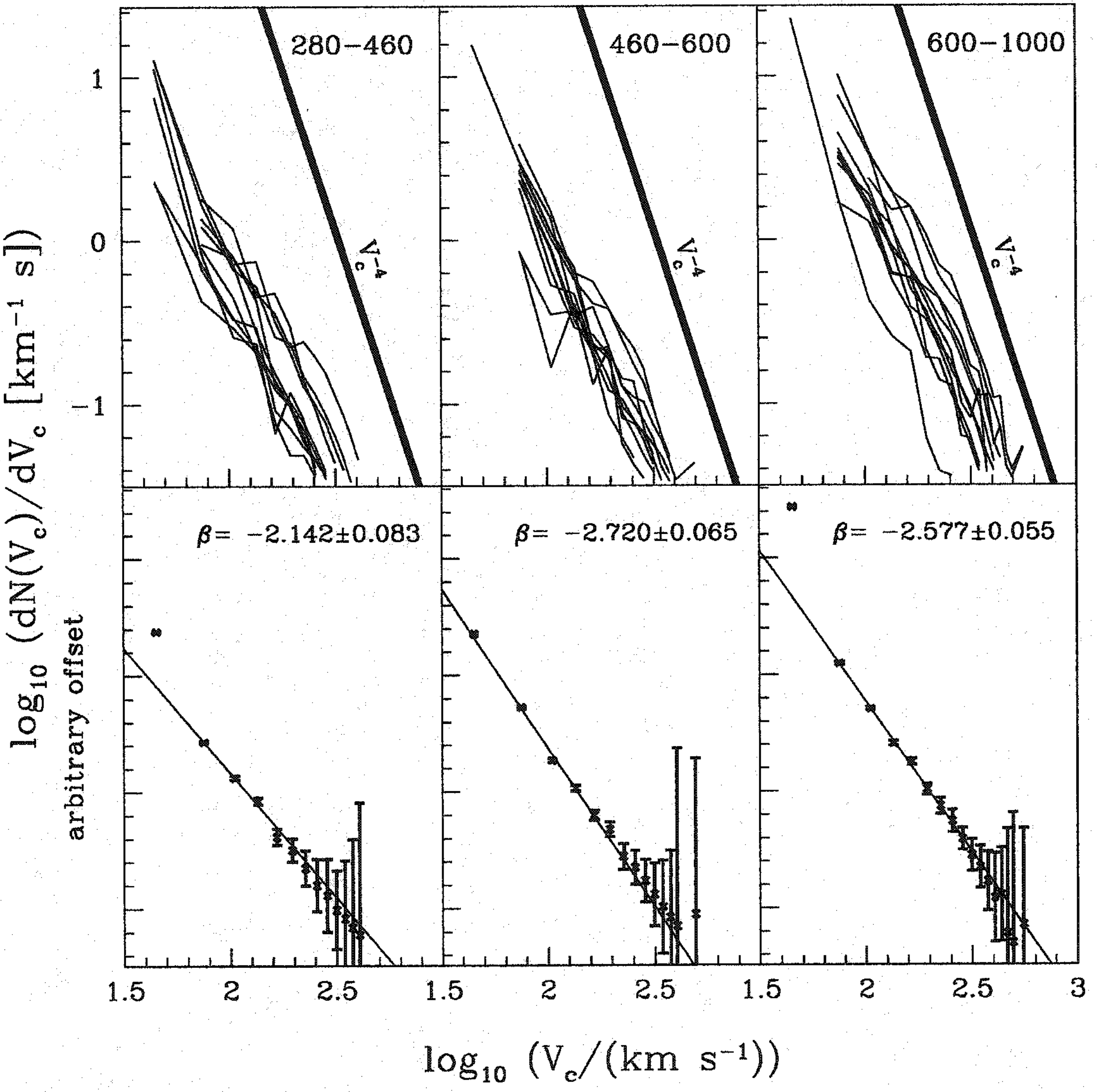

Figure 1.3 The observed CGVF, binned by cluster velocity dispersion. *Top panels:* Individual cluster GCVFs are shown with thin lines. The dark line in each panel has a slope of -4, and is provided for reference. Cluster velocity dispersion ranges are shown in the upper right of each panel, in $\mathrm{km\,s^{-1}}$. *Bottom panels:* Each panel shows the composite functions constructed from clusters having $\sigma_{\rm cl}$ in the range indicated in the panel directly above. Error bars take into account Poisson error in counting galaxies both within $R_{\rm vir}$ and in the background annulus. A power law (Equation 1.13) was fitted to these data, and is shown as a thin solid line. The slopes of the composite functions are shown in the upper right hand corner of each panel.

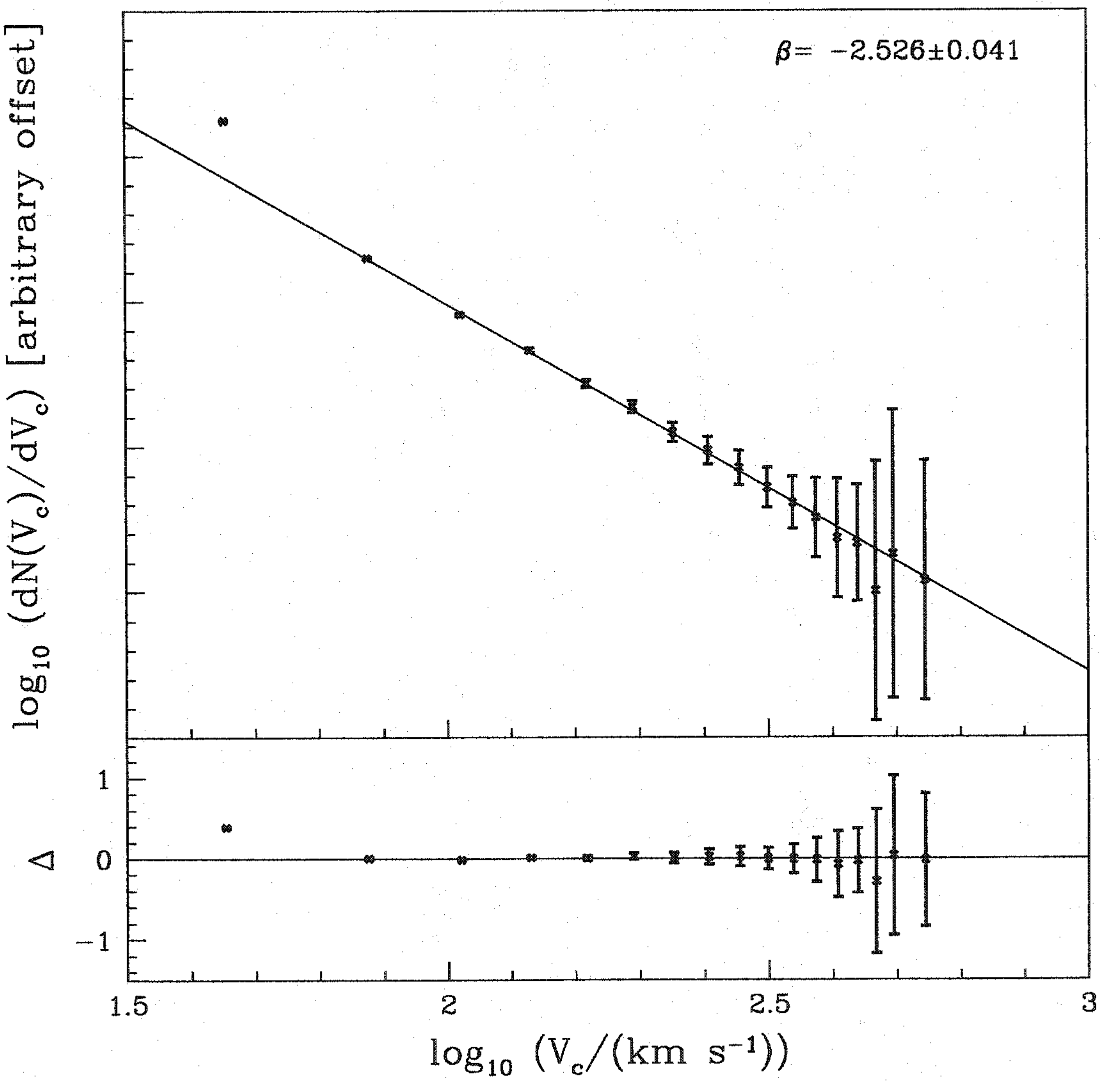

Figure 1.4 The composite GCVF, constructed from all 34 SDSS clusters in our sample. *Top panel:* The error bars were computed as in Figure 1.3. The best-fitting power law is shown as a thin solid line, and its slope is shown in the upper right hand corner. *Bottom panel:* The residuals of the composite cluster GCVF from the best fit power law.

dispersion bins. The bins were chosen such that each contains approximately the same number of clusters. The bold lines have a slope of -4 and are for reference only.

Motivated by theory, we fit a power law to our observed GCVFs.

$$\log_{10}\left[\frac{dN(V_c)}{dV_c}\right] = \log_{10} N_{200} + \beta \log_{10}\left(\frac{V_c}{200\ \mathrm{kms}^{-1}}\right), \tag{1.13}$$

where β represents the slope of the power law and N_{200} is the normalization at V_c=200 km s^{-1}. The results of the fit are reported in Table 1.1, columns 8–11.

We also tested whether the data could be better fit by a Schechter function, which is a power law that is exponentially damped at high circular velocities. We found that the best-fit power law resulted in a smaller weighted sum-of-squares than the best-fit Schechter function for the majority of clusters, despite the additional degree of freedom associated with the Schechter function. In the cases where the Schechter function resulted in a lower weighted sum of squares, it was not clear that the Schechter function provided a better fit, since it has an additional parameter. We therefore used the Akaike Corrected Information Criterion (AIC_c) to determine which model is more appropriate. For each model, we computed:

$$AIC_c = N\ln(S/N) + 2K + \frac{2K(K+1)}{N-K-1}, \tag{1.14}$$

where N is the number of data points, S is the weighted sum of squares, and K is the number of parameters being fit for plus one. We found that in all but four cases, the AIC_c resulting from the power law fit was lower than that resulting from the Schechter function fit. Thus, in general, a power law is adequate to describe the data.

The power law form of the cluster GCVF, while predicted analytically and numerically, is nonetheless somewhat surprising. The cluster luminosity function is usually described by a Schechter function. Because the luminosities of both early and late type galaxies are related to their circular velocities by power laws ($L \propto V^n$), it is not obvious that the galaxy population as a whole should obey both a Schecter luminosity function and a power law GCVF.

Part of the explanation are the facts that both early and late types contribute to the GCVF, that they have different relations between M_{r^*} and $V_{\rm c}$, and that they make up different fractions of the population with magnitude. Because the slope of the $V_{\rm c} - M_{\rm r}$ relation for early types is steeper than for late types, late type galaxies were mapped onto a smaller range of velocities than early types. Thus, late type galaxies that populate the knee in the luminosity function were mapped to lower velocities than early type galaxies with the same luminosity. The proportion of early and late type galaxies that make up the knee in the luminosity function affects the placement and prominence of the knee in the GCVF. In general, it was smeared out in the GCVF.

Another reason for the power law GCVF is that our completeness limits did not allow us to observe the shape of the GCVF at velocities dominated solely by galaxies from the flat part of the luminosity function, where we would expect the GCVF to flatten out. Thus, very few bins define the knee.

Finally, the signal-to-noise in each cluster GCVF is relatively low due to the small number of galaxies used. It would be difficult to trace the high velocity exponential drop-off if the GCVF did follow a Schechter function.

In order to increase the signal to noise in our determination of the cluster GCVF, we built composite cluster GCVFs using a technique analogous to that of Colless (1989) for building composite cluster luminosity functions. The number of galaxies in the jth $V_{\rm c}$ bin of the composite cluster GCVF is given by:

$$N_{{\rm c}j} = \frac{N_{\rm c0}}{m_j} \sum_i \frac{N_{ij}}{N_{i0}}, \tag{1.15}$$

where N_{ij} is the number of galaxies in the jth bin of the ith cluster GCVF, N_{i0} is the normalization used for the ith cluster GCVF (taken as the number of galaxies brighter than $100\,{\rm km\,s^{-1}}$), m_j is the number of clusters contributing to the jth bin, and $N_{\rm c0}$ is the sum of all the normalizations:

$$N_{\rm c0} = \sum_i N_{i0}. \tag{1.16}$$

The error on the composite cluster GCVF is:

$$\Delta N_{\rm cj} = \frac{N_{\rm c0}}{m_j} \left[\sum_i \left(\frac{\Delta N_{ij}}{N_{i0}} \right)^2 \right]^{\frac{1}{2}}, \tag{1.17}$$

where ΔN_{ij} is the error on the jth bin of the ith cluster.

The composite cluster GCVFs in the three $\sigma_{\rm cl}$ bins are shown in the bottom panel of Figure 1.3. The composite cluster GCVF constructed using all 34 clusters is shown in Figure 1.4.

1.7.2 Is cluster substructure self-similar?

Moore et al. (1999) found that the cumulative GCVF for a Virgo-like simulation is identical to that of subhalos within a Milky-Way-like simulation, provided the velocities are scaled by the velocity of the parent halo ($V_{\rm cl} = \sqrt{2}\sigma_{\rm cl}$). In the top panel of Figure 1.5, we have plotted the cumulative, scaled GCVF for all fifteen simulated clusters from Table 1.2. Our simulated clusters have very similar cumulative, scaled GCVFs, in agreement with the results of Moore et al. (1999).

In the bottom panel of Figure 1.5, we plot the same quantity for our sample of SDSS clusters. The slopes and offsets of the simulated and observed clusters cannot be compared directly, since the effects of baryons have not been included in the simulations. However, assuming that baryonic physics changes the shapes of all the GCVFs in a similar way, we can compare the scatter in the observed and simulated GCVFs. The observations display a significantly larger scatter than the simulations. Uncertainties in the measurement of $V_{\rm cl}$ and Poisson errors both contribute to the observed scatter. Taking the plot of $\log_{10}[N(>(V_{\rm c}/V_{\rm cl}))]$ versus $V_{\rm c}/V_{\rm cl}$ to be a power law, the variance in $\log_{10}[N(>(V_{\rm c}/V_{\rm cl}))]$ due to measurement errors in $\sigma_{\rm cl}$ is

$$\Delta^2_{\log_{10}[N(>(V_c/V_{\rm cl}))]} = \frac{1}{\ln 10}\frac{(\Delta V_{\rm cl})^2}{V_{\rm cl}^2}, \tag{1.18}$$

where $V_{\rm cl} = \sqrt{2}\sigma_{\rm cl}$. Using the values of $\sigma_{\rm cl}$ found in §1.4, and computing ΔV_{cl} from the errors in $\sigma_{\rm cl}$, we found that the scatter due to measurement errors in $\sigma_{\rm cl}$ is 0.009, while the scatter due to Poisson noise is 0.012. The total observed scatter is 0.064. Thus, the instrinsic scatter is ~0.043. This is very similar to the intrinsic scatter we measured in the simulations. Thus our observed GCVFs show the same degree of variations found in ΛCDM dark matter cluster simulations.

1.7.3 Trends in the Cluster GCVF with Cluster Velocity Dispersion

Figure 1.3 shows that the cluster GCVF depends upon the cluster velocity dispersion. The top panel of Figure 1.6 shows that the best-fitting power law slope, β, while showing a fair amount of scatter, does not vary systematically with $\sigma_{\rm cl}$. It has a mean value of $\overline{\beta} = -2.4 \pm 0.8$. The slope of the composite cluster GCVF shown in Figure 1.4 is -2.61 ± 0.04, consistent with the mean slope.

We compared the slopes of the observed GCVFs to those of the simulated GCVFs. The latter are plotted as open circles in the top panel of Figure 1.6. The dashed line is drawn at their mean value: $\overline{\beta_{sim}} = -3.4 \pm 0.8$. The average value of the simulations is somewhat steeper than that of the observations, although formally they agree within the uncertainties. It should be noted that the slopes are not directly comparable because the simulations do not account for the effects of baryons. These effects are discussed in the next subsection.

The normalizations of the individual cluster GCVFs are plotted in the middle panel of Figure 1.6 and show a clear systematic trend in the sense that higher mass clusters host more galaxies. The best fit line to these data are

$$\log_{10} N_{200} = (2.20 \pm 0.20)\log_{10}\sigma_{\rm cl} - (6.65 \pm 0.55). \tag{1.19}$$

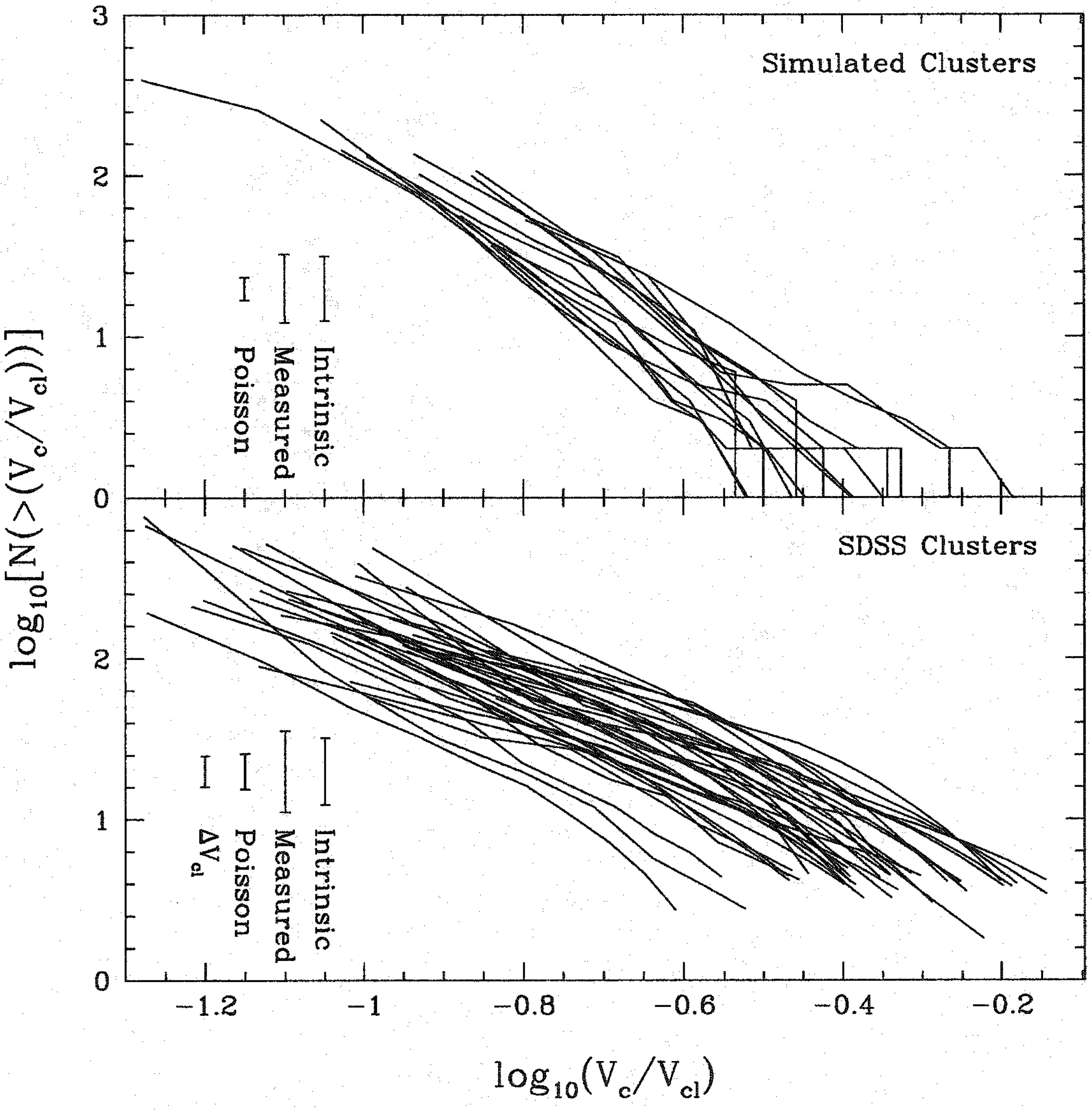

Figure 1.5 The simulated and observed SDSS CGVFs, with galaxy circular velocities scaled by cluster circular velocites. The error bars have length 2Δ, where Δ is the RMS scatter at $\log_{10}(V_c/V_{cl} \approx -0.7)$ due to various sources, as labelled. *Poisson* refers to Poisson noise in counting galaxies within R_{vir} for the simulated clusters and to Poisson noise in counting galaxies within R_{vir} and the background annulus for the SDSS clusters. *Measured* refers to the total measured scatter. ΔV_{cl} refers to the scatter in $\log_{10}[N(> (V_c/V_{cl}))]$ due to errors in measuring V_{cl}, and *Intrinsic* refers to the portion of the total measured scatter unaccounted for by Poisson scatter in the case of the simulations or by both Poisson scatter and that induced by ΔV_{cl} for the SDSS clusters.

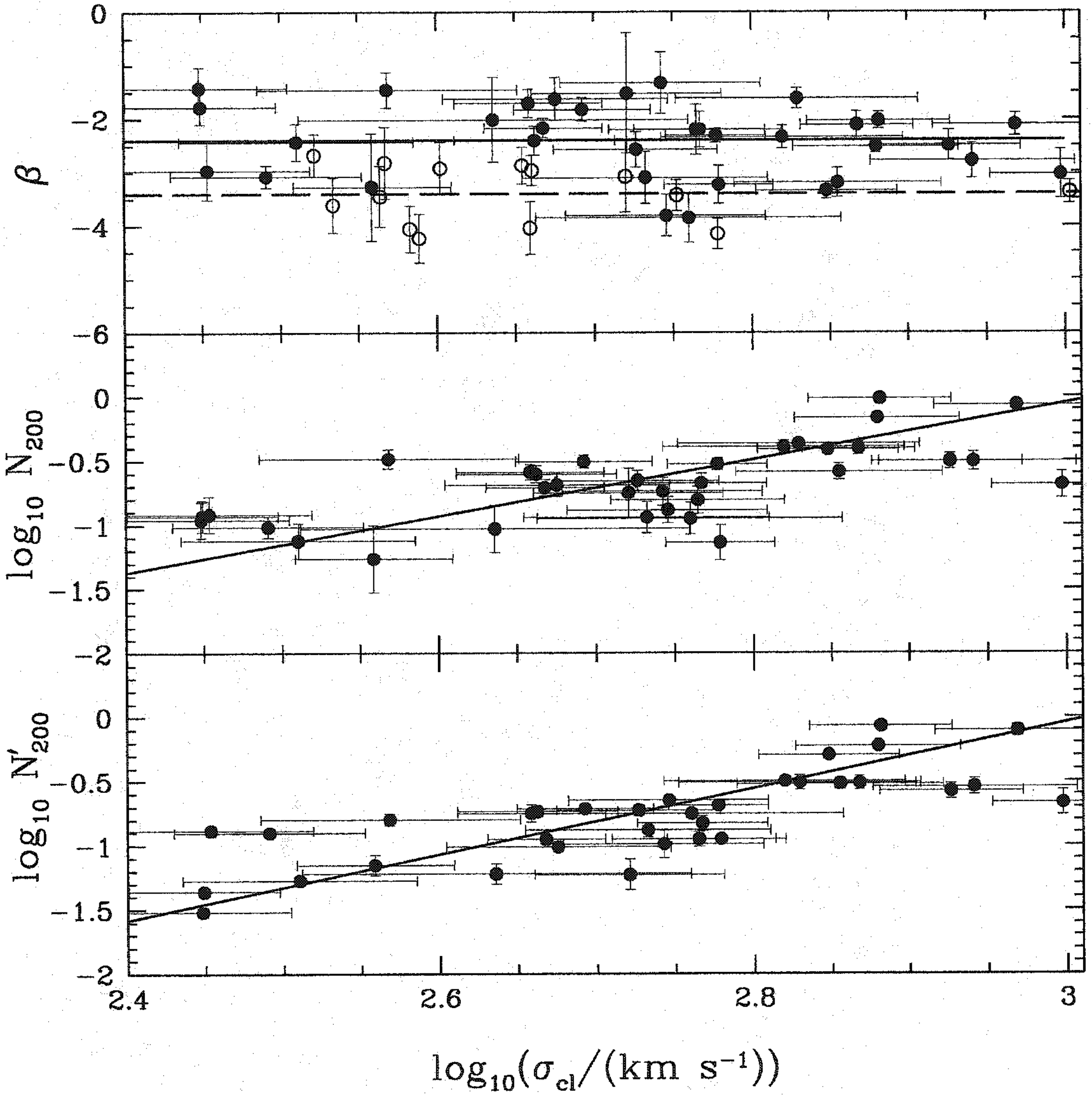

Figure 1.6 *Top Panel:* The slope of the cluster GCVF as a function of cluster velocity dispersion. Solid points are for the observed cluster GCVFs. The mean value is indicated by the solid line. Open points are for the simulated cluster GCVFs. The mean value is indicated by a dashed line. *Middle Panel:* The normalization of the observed cluster GCVF as a function of cluster velocity dispersion. High $\sigma_{\rm cl}$ clusters tend to contain more galaxies than low $\sigma_{\rm cl}$. The line that best fits this trend is given by Equation 1.19 and is overplotted. *Bottom Panel:* The normalizations of the fits for the observed cluster GCVFs were recomputed while holding the slope fixed to the mean value shown in the top panel. The new normalizations are plotted against $\sigma_{\rm cl}$ in the bottom panel. The line that best fits these data is given by Equation 1.20 and is overplotted.

Finally, we recalculated our normalizations with the slope fixed to its mean value of -2.4. These values of $\log_{10} N'_{200}$ and their errors can be found in Table 1.1, columns 12 and 13, and are plotted against $\sigma_{\rm cl}$ in the third panel of Figure 1.6. The best fit line to these data is

$$\log_{10} N'_{200} = (2.57 \pm 0.22)\,\sigma_{\rm cl} - (7.75 \pm 0.61)\,. \tag{1.20}$$

1.7.4 The Effects of Baryons on the Cluster GCVF

The results of the previous subsection suggest that subhalos in simulated clusters may have steeper GCVFs than measured for galaxies in clusters. We also noted that a more meaningful comparison would require taking into account the effects of both dark matter *and* baryons in the simulations, since the total circular velocity profile is given by:

$$V_{\rm c}^2(r) = V_{\rm c,b}^2(r) + V_{\rm c,DM}^2(r), \tag{1.21}$$

where $V_{\rm c,b}(r)$ is the circular velocity profile of the collapsed baryonic mass and $V_{\rm c,DM}(r)$ is the circular velocity profile of the dark matter halo.

A full description of the baryonic mass distribution is needed to compute $V_{\rm c,b}(r)$ and requires knowledge of the density profile shape (e.g. Hernquist for early types and exponential for late types), a normalization (total galaxy mass), and a scalelength (galaxy size). The challenge lies in populating the simulated subhalos with galaxies in a way that mimics, as closely as possible, observed empirical relations. Our method for populating the subhalos identified in our highest resolution simulation is described in Appendix A.

In addition to the direct contribution baryons make to the enclosed mass at small radii, they pull the dark matter into a more concentrated equilibrium configuration than it would have in their absence. We therefore modelled how $V_{\rm c,DM}(r)$, the circular velocity profile of the final contracted dark matter halo, differs from $V_{\mathrm{c,sim}}(r)$, the circular velocity profile measured from the dark matter simulation. We assumed that this collapse is slow and that the halo remains spherical. Under these conditions, a dark matter particle conserves angular momentum as it moves closer to the center of the potential (Blumenthal et al., 1986; Dalcanton et al., 1997; Mo et al., 1998):

$$M_{\mathrm{DM}}(r_{\mathrm{f}})r_{\mathrm{f}} = M_{\mathrm{sim}}(r_{\mathrm{i}})r_{\mathrm{i}}, \tag{1.22}$$

where M_{sim} is the mass profile measured from the dark matter simulation, M_{DM} is the final mass profile the dark matter assumes after adiabatic contraction, r_{i} is the initial mean radius of the particle, and r_{f} is the final mean radius of the particle. If f_{cool} is the fraction of the total mass in cooled baryons, then

$$M_{\mathrm{DM}}(r_{\mathrm{f}}) = M_{\mathrm{b}}(r_{\mathrm{f}}) + M_{\mathrm{sim}}(r_{\mathrm{i}})(1 - f_{\mathrm{cool}}), \tag{1.23}$$

where M_{b} is the baryonic mass profile. While the peak circular velocity, V_{pk}, was robustly measured from all of the simulations listed in Table 1.2, a reliable determination of $V_{\mathrm{sim}}(r_{\mathrm{i}})$ or $M_{\mathrm{sim}}(r_{\mathrm{i}})$ could only be made from the highest resolution, lowest softening simulation described in the last entry in Table 1.2. Using the $M_{\mathrm{sim}}(r_{\mathrm{i}})$ measured for each subhalo in the simulation, the values of f_{cool} described in §A.2, and the $M_{\mathrm{b}}(r)$ computed from the density profiles described in Appendix A, we calculated $M_{\mathrm{DM}}(\mathrm{r_f})$ from Equations 1.22 and 1.23. From $M_{\mathrm{DM}}(\mathrm{r_f})$ it was trivial to calculate $V_{\mathrm{c,DM}}(r)$.

Once the total circular velocity profile $V_{\mathrm{c}}(r)$ due to dark matter and baryons was determined from Equation 1.21, we measured a characteristic circular velocity, V_{c}, that is analogous to that deduced for our observed early and late type galaxies. We estimated V_{c} as the circular velocity at three scale lengths.

In Figure 1.7, we compare the simulated GCVF to that of SDSS clusters that have similar velocity dispersions. The dashed line represents the simulated cluster

GCVF with no correction for baryons and assuming that $V_c = V_{pk}$. The simulated cluster GCVF in this case is too steep, underpredicting the number of galaxies at high V_c. The bold solid lines bracket simulated GCVFs which have been corrected for the effects of baryonic infall. The baryonic correction increased the number of high V_c galaxies and decreased the number of low V_c galaxies, bringing the simulations into rough agreement with the observations. This effect held whether V_c was measured at 2, 3, or 4 scale lengths, but was strongest if V_c was measured at 2 scale lengths.

While ΛCDM models can reproduce the cluster GCVF, they overproduce the number of field galaxies with $V \lesssim 120\,\mathrm{km\,s^{-1}}$ (Gonzalez et al., 2000; Kochanek & White, 2001). Any solution to the disagreement in the field must preserve the agreement found in clusters. Modifications to CDM would affect the substructure within clusters as well as in the field, and tend to contradict other observations (Barkana et al., 2001; Gnedin & Ostriker, 2001; Hui, 2001; Miralda-Escudé, 2002). Supernova feedback alone fails to reproduce the luminosity function of the Local Group (Somerville, 2002), but a combination of feedback and squelching can. However, squelching cannot play a role at the circular velocities we have investigated here. It affects only galaxies with circular velocities $\lesssim 50\ \mathrm{km\,s^{-1}}$. The importance of supernova feedback at higher circular velocities is uncertain. Recent work by Mac Low & Ferrara (1999) suggests that it can only regulate star formation, not remove mass at these scales. Regardless, it should be equally important in clusters and in the field.

1.7.5 The Cluster Versus Field GCVF

The circular velocity function of dark matter halos within clusters is expected to be a function of environment. Although we found only small differences among the populations of massive clusters, there may still be substantial differences between clusters and the field. First, hierarchical clustering theory predicts that massive halos form from rarer density peaks and should therefore be more clustered than low mass halos (Kaiser, 1984; Davis et al., 1985; White et al., 1987, 1988; Governato et al.,

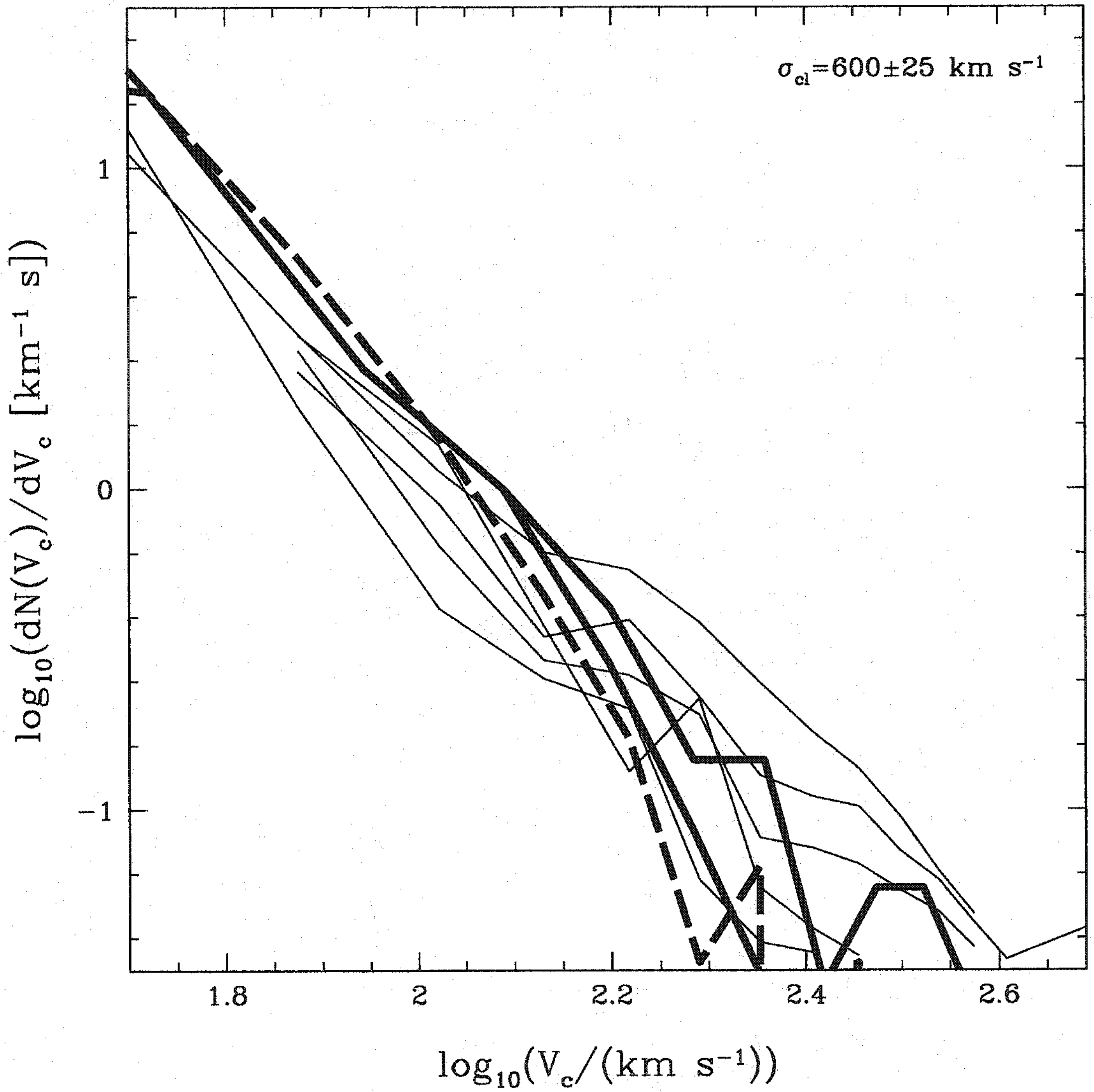

Figure 1.7 Comparison of the GCVF measured from our highest resolution galaxy cluster simulation (HR Virgo) to that measured in SDSS clusters with similar velocity dispersions. The dashed line is the simulated GCVF constructed using the $V_{\rm pk}$ values output by SKID. Thick solid lines represent the range of corrected GCVFs given uncertainties in how gas infall affects galaxy rotation curves (see Appendix A for details). Thin solid lines are the GCVFs of SDSS clusters with measured velocity dispersions within 25 km s^{-1} of that of the simulated cluster.

1998). Second, halos within clusters are subject to the mass-altering processes of tidal stripping, dynamical friction, and galaxy harrassment (Moore et al., 1996). Third, low mass halos in dense regions formed, on average, earlier than those in the field. Reionization can therefore preferentially suppress the late-time formation of galaxies within low mass field halos (Quinn et al., 1996; Tully et al., 2002; Benson et al., 2003; Somerville, 2002), although at velocites below what we can probe in this work.

Several attempts have been made to determine to the field GCVF. Cole & Kaiser (1989) determined the circular velocity function of field galaxies by starting with a Schechter luminosity function and assuming $L \propto V_{\rm c}^{3-4}$, not taking into account that a late type galaxy has a lower circular velocity than an early type galaxy with the same absolute magnitude, or that their relative abundances depend upon luminosity. Shimasaku (1993) computed the field GCVF galaxy-by-galaxy using both HI 21 cm line widths (~400) and the Tully-Fisher relation (~300) for spiral galaxies and stellar velocity dispersions (~100) and the Faber Jackson relation (~90) for early type galaxies. They found that early types dominate at the high velocity end.

Gonzalez et al. (2000) determined the field GCVF by performing variable transformations on the type-specific B-band luminosity functions determined from the SSRS2 survey. They found that, given the available Tully-Fisher and Faber Jackson Relations, all field galaxies could be treated as late types without changing the results. Doing so, they found that the number density of galaxies per unit velocity can be described by a Schecter function,

$$\tilde{\Psi}(V_{\rm c})dV_{\rm c} = \tilde{\Psi}_* \left(\frac{V_{\rm c}}{V_{{\rm c},*}}\right)^{\beta} \exp\left[-\left(\frac{V_{\rm c}}{V_{{\rm c},*}}\right)^{n}\right] \frac{dV_{\rm c}}{V_{{\rm c},*}}, \tag{1.24}$$

where $\tilde{\Psi}_* = (3.2 \pm 0.6) \times 10^{-2}$ Mpc^{-3} h^3, $\beta = -1.3 \pm 0.13$, $n = 2.5$, $V_{{\rm c},*} = 247 \pm 7$. Kochanek & White (2001) found similar results, although they took into account the different transformations for early and late types. Sheth et al. (2003) analyzed field early type galaxies within the SDSS, and found that accounting for the scatter around the mean Tully-Fisher and Faber Jackson or Fundamental Plane relations is extremely important for reproducing the high velocity end of the GCVF.

In order to allow a direct comparison to our cluster GCVFs, we constructed a field GCVF using the same survey data and relations that we used in the previous cluster analysis. We select galaxies from the SDSS EDR spectroscopic sample with $14.5 < r^* < 17.77$. Each of the resulting ~22,000 galaxies was assigned a weight equal to the inverse of the volume over which the galaxy could be observed, given the apparent magnitude limits. The value of the field GCVF in a given circular velocity bin is equal to the sum of the weights of the galaxies in that bin. The results are plotted as points with error bars in Figure 1.8, along with the field GCVF given by Gonzalez et al. (2000) (Equation 1.24; solid bold line). The thin solid lines are the cluster GCVFs measured in this work, normalized at the velocity bin where their average slope equals the slope of the field GCVF. The cluster GCVF is steeper than that of the field for $V_c \lesssim 200\,\mathrm{km\,s^{-1}}$.

Following the discussion in Section 1.7.3, the difference in the shapes of the field and cluster GCVFs may be explained by their different relative abundances of early and late type galaxies as a function of luminosity. It must be noted that our division of galaxies into early and late types depends upon the $u^* - r^*$ color, which is sensitive to star formation. There is some evidence that the cluster environment supresses star formation (Couch & Sharples, 1987; Barger et al., 1996; Poggianti et al., 1999). A field galaxy that falls into a cluster and experiences truncated star formation would redden, but its r^*-band luminosity would not change significantly, because r^* is sensitive to the total stellar mass. If the change in $u^* - r^*$ is large enough to change late types into early types, the cluster GCVF would have more high-velocity galaxies and fewer lower-velocity galaxies relative to the field, as is observed. While the trend is correct, detailed models are required to determine to what extent this effect can explain the observed differences between the field and cluster GCVFs.

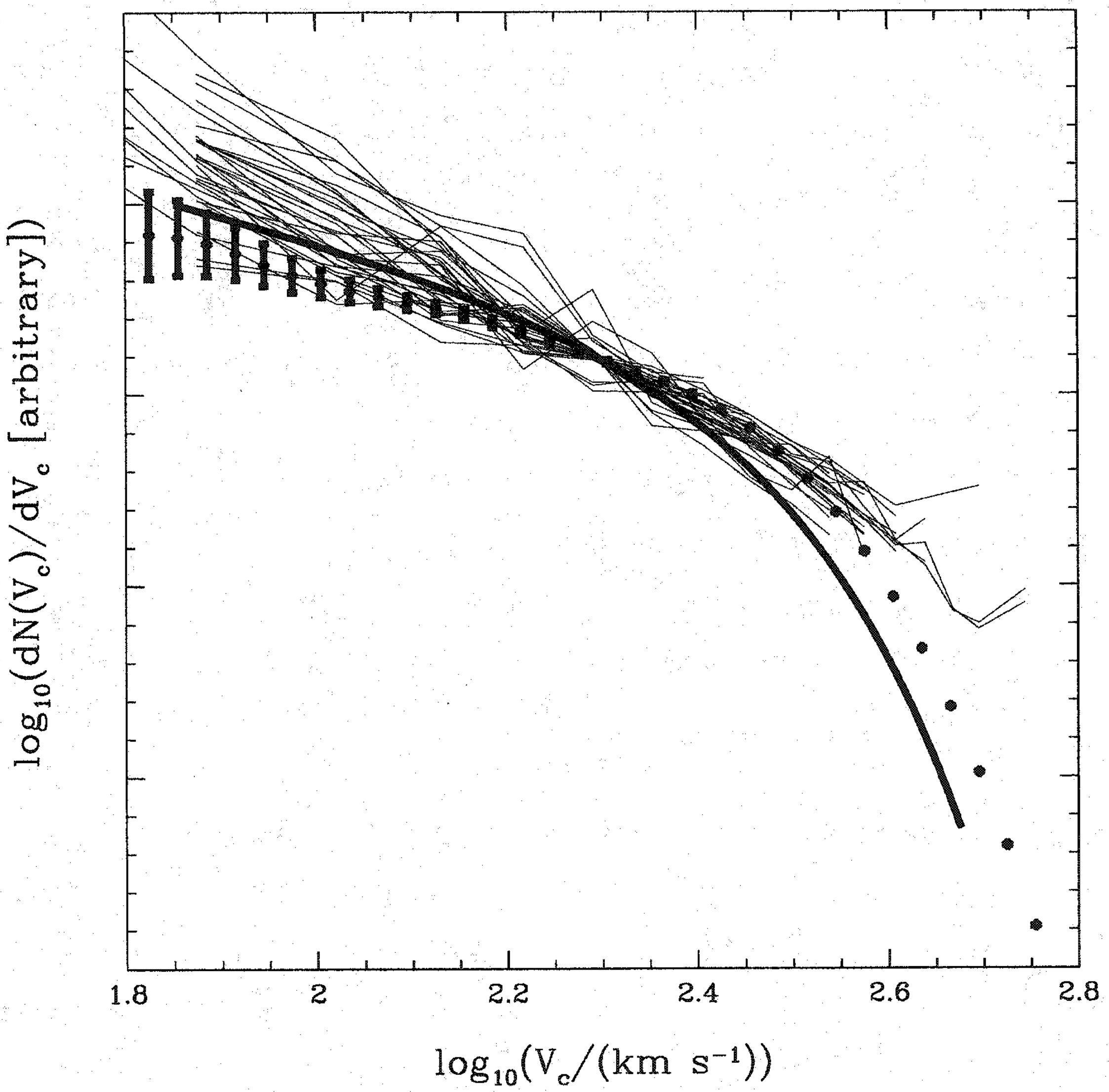

Figure 1.8 GCVFs for the SDSS cluster sample and the field. The thin lines represent the GCVFs for SDSS clusters, normalized at $\log_{10}(V_c/\ \mathrm{km\,s^{-1}}) \approx 2.3$. The solid bold line is the similarly normalized observed field GCVF as determined by Gonzalez et al. (2000). The points with error bars are the field GCVF determined from SDSS data as described in §1.7.5. Because of the arbitrary normalization, this plot is suitable only for assessing differences in the shape of the GCVF in clusters and the field. Although the cluster GCVFs display a range of slopes, they are steeper than the field for $V_c \lesssim 200$ and more shallow for $V_c \gtrsim 200$. The field GCVFs are consistent with one another within the error bars at $V_c < 200\,\mathrm{km\,s^{-1}}$. The field GCVF we determined lies above that measured by Gonzalez et al. (2000) at $V_c > 200\ \mathrm{km\,s^{-1}}$ because we took into account the scatter around the relations used to compute V_c for early type galaxies, which dominate the GCVF at large V_c.

1.8 Summary

We constructed the cluster and field galaxy circular velocity functions using data from the Sloan Digital Sky Survey Early Data Release. Circular velocities were determined using the inverse Tully-Fisher and Fundamental Plane relations on a galaxy-by-galaxy basis, rather than by performing a transformation of variables on a functional fit to the luminosity function. We also analyzed the GCVFs determined from 15 clusters simulated in the ΛCDM concordance cosmology. In general, we found good agreement between simulations and observations. Our results can be summarized as follows:

1. Given out completeness limits and errors, our observed cluster GCVFs were adequately fit by power laws.

2. We tested the self-similarity claimed by Moore et al. (1999) for our scaled simulated and observed cluster GCVFs. The simulated GCVFs are indeed very similar to one another, and show only a small scatter. The intrinsic scatter in the observed cluster GCVF is similar to that predicted.

3. The normalization of the observed cluster GCVF increases with cluster velocity dispersion, while the slope is constant. The average slope of the observed cluster GCVF is somewhat flatter ($\beta \approx -2.4$) than that computed from ΛCDM cluster simulations ($\beta = -3.4$). However, the errors on these average slopes are large, and overlap. If the difference between the simulated and the observed clusters is real, it is most likely due to the fact that the simulations do not include the effects of baryons on galaxy rotation curves.

4. We estimated the effects of baryons on the simulated GCVFs. Baryons can flatten the simulated GCVF enough to bring it into agreement with the GCVFs of observed clusters with similar velocity dispersions. This agreement between the amount of cluster substructure predicted by N–body simulations and that observed in real clusters has been found previously by Moore et al. (1999) for an SCDM simulation of a Virgo-like cluster. Our approach is different in that we treat early and late types

distinctly, as well as account for the effects of baryons on galaxy rotation curves. In addition, our simulated cluster has evolved in the concordance cosmology.

1.9 Acknowledgments

VD and DR acknowledge funding from the Graduate Student Researchers Program. JJD was partially supported through the Alfred P. Sloan Foundation. TRQ was partially supported by the National Science Foundation.

Simulations were run at the ARSC (Fairbanks) and CINECA (Bologna, Italy) supercomputing centers.

This research has made use of the NASA/IPAC Extragalactic Database (NED), which is operated by the Jet Propulsion Laboratory, Caltech, under contract with the National Aeronautics and Space Administration.

The Sloan Digital Sky Survey (SDSS) is a joint project of The University of Chicago, Fermilab, the Institute for Advanced Study, the Japan Participation Group, The Johns Hopkins University, the Los Alamos National Laboratory, the Max-Planck-Institute for Astronomy (MPIA), the Max-Planck-Institute for Astrophysics (MPA), New Mexico State University, the United States Naval Observatory, the University of Pittsburgh, Princeton University, and the University of Washington. Apache Point Observatory, site of the SDSS telescopes, is operated by the Astrophysical Research Consortium (ARC).

Funding for the project has been provided by the Alfred P. Sloan Foundation, the SDSS member institutions, the National Aeronautics and Space Administration, the National Science Foundation, the U.S. Department of Energy, the Japanese Monbukagakusho, and the Max Planck Society. The SDSS Web site is `http://www.sdss.org/`.

Chapter 2

THE MORPHOLOGICAL CONTENT OF TEN EDISCS CLUSTERS AT $0.4 < z < 0.8$

2.1 Abstract

We describe a new Hubble Space Telescope (HST) survey of ten high redshift ($0.4 < z < 0.8$) galaxy clusters from the ESO Distant Cluster Survey (EDisCS). Each cluster was imaged in the F814W filter (I band) for 8 orbits with the Advanced Camera for Surveys Wide Field Camera (ACS WFC). The imaging is one orbit deep over a $\sim$6.5$'\times$ 6.5$'$ region in the field of each cluster. This area corresponds to $\sim$2.5 Mpc $\times$ 2.5 Mpc at the redshifts of our clusters, assuming a Hubble constant of 70 km s^{-1} Mpc^{-1}. The 3.4$'\times$ 3.4$'$ region centered on the cluster was imaged for an additional 4 orbits, for an effective exposure time of 5 orbits on the region with the highest surface density of galaxies. Based on these data, we present visual morphological classifications for galaxies brighter than $I_{\rm auto} < 23$. This magnitude limit yields $\sim$700 galaxies per cluster. We utilize these catalogs, in conjunction with published data for clusters at other redshifts, to assess the evolution of the morphological content within the cores of rich clusters out to $z \sim 0.8$. We find that the scatter in the fractions of E, S0, and Sp+Irr galaxies between clusters is quite large. Despite these variations, the typical percentage of S0 galaxies in cluster cores has systematically increased from $\sim$15% to $\sim$55% over the last 7.5 Gyr. This growth in the S0 population is accompanied by a commensurate decrease in the spiral fraction. There is no trend in the elliptical fraction with redshift. These data support a scenario in which elliptical galaxies were assembled at high redshift ($z \gtrsim 3$) and infalling spiral galaxies are transformed into

S0 galaxies within the cluster.

2.2 Introduction

Since the initial recognition that early-type galaxies are more common in nearby rich clusters than in the low-density field (Spitzer & Baade, 1951), much progress has been made in characterizing the correlation between Hubble type and environment. Abell (1965) noted a relationship between the overall structure of a cluster and the morphologies of the galaxies within it: compact, regular clusters contain a high fraction of elliptical and S0 galaxies while open, irregular clusters host a morphological mix resembling that in the field. In a seminal paper, Gunn & Gott (1972) placed these observations within the developing theory of the growth of structure from primordial density perturbations. They suggested that the structure of a cluster is related to its dynamical state, such that irregular clusters are unevolved, while regular clusters have collapsed and virialized. They also introduced the idea that galaxies may change morphology in response to the extreme cluster environment. In their model, the hot intracluster medium strips gas from spiral disks, which then fade into the small, featureless disks associated with S0 galaxies. Oemler (1974) refined Abell's classification of local clusters based on structure and morphological content. He defined three categories, in order of increasing cluster concentration and regularity: spiral-rich, spiral-poor, and elliptical-rich. Following Gunn & Gott (1972), he concluded that spiral-rich clusters become spiral-poor through ram-pressure stripping as they virialize. However, lacking a mechanism to transform S0s into ellipticals, he hypothesized that the progenitors of present-day elliptical-rich clusters must have begun as the densest fluctuations in the early universe, evolved quickly, and are no longer present at low redshift. Importantly, he pointed out that ram-pressure stripping cannot operate in lower density regions where S0s are nevertheless found. Therefore, at least some S0s formed in a different way, perhaps as a result of the initial conditions of galaxy formation.

The relationship between the structure of local clusters and their morphological content suggest that the cluster environment may transform late-type galaxies into early types. Observations of clusters at higher redshift provide more direct evidence of such a transformation. Ground-based observations of clusters out to $z = 0.5$ have revealed that the fraction of blue galaxies increases with redshift, indicating that the star-forming properties of galaxies within clusters have evolved over the last 6 Gyr (Butcher & Oemler, 1978, 1984). Several groups have searched for evidence that the evolution in star formation is accompanied by evolution in the clusters' morphological content. Early work using high-quality ground-based and pre-refurbishment HST imaging of 5 clusters at $0.35 \lesssim z \lesssim 0.55$ revealed the blue galaxies to be spirals, a significant fraction of which show signs of recent disturbance (Lavery et al., 1992; Couch et al., 1994; Dressler et al., 1994; Wirth et al., 1994; Oemler et al., 1997).

Additional studies of the morphological content of clusters revealed that the S0 population may also have experienced significant evolution since $z \lesssim 0.6$. The largest of these studies was carried out by the MORPHS collaboration, which obtained post-refurbishment imaging for 10 clusters at $0.37 < z < 0.56$, including 5 which had not previously been observed with HST (Smail et al., 1997; Dressler et al., 1997). In addition to confirming the increase in the spiral fraction with increasing redshift, they discovered a commensurate decrease in the S0 fraction. Their findings bolstered the notion that the cluster environment triggers the transformation of spiral galaxies into S0s. However, their data also shows that the elliptical population was already in place at $z \lesssim 0.6$.

The trends discovered by MORPHS have been confirmed both in lower and higher redshift clusters. Couch et al. (1998) found similar results with post-refurbishment HST imaging of 3 clusters at $z \sim 0.3$, and Fasano et al. (2000) confirmed these findings in a ground-based study of 9 clusters at $0.1 < z < 0.25$. These trends have been traced to higher redshifts based on only two clusters. van Dokkum et al. (2000) found that the early-type fraction (E+S0) in the X-ray luminous cluster MS1054-03 at $z = 0.83$ is significantly lower than that in lower redshift clusters, as expected if ellipticals assembled early and infalling spirals have been transformed into S0s. Similar results are found for CL1324+3011 at $z = 0.76$ by Lubin et al. (2002).

Although low S0 or early-type fractions have been measured in distant clusters by several groups, the claim of evolution has been contested. Stanford et al. (1997) examined HST images of 19 galaxy clusters at $0.3 < z < 0.9$, including 8 of the 10 MORPHS clusters. They found that the fraction of early-type galaxies remains constant over this redshift range. Lubin et al. (1998) analyzed the morphological content of CL0023+042 ($z = 0.83$) and CL1604+4304 ($z = 0.90$). The former consists of 2 groups or poor clusters which may or may not be merging, and has a morphological mix similar to that of the field. The latter, however, is a relaxed cluster (which was also included in the Stanford study) with an elliptical- and S0-rich morphological mix more similar to that of rich clusters at $z = 0$ than to the S0-poor MORPHS clusters.

Discrepant results regarding the evolution of the S0 population in clusters stem from at least two causes. First, S0 galaxies are difficult to distinguish from ellipticals, especially at high redshift (Stanford et al., 1997; Andreon et al., 1997; Andreon, 1998; Jones et al., 2000). Second, distant clusters tend to be younger and less evolved than nearby examples. Thus, the scatter in morphological fractions is expected to be high. In this chapter, we address the second uncertainty by analyzing the morphological content of ten clusters at $0.4 < z < 0.8$ drawn from the ESO Distant Cluster Survey (EDisCS; §2.3). This sample greatly increases the number of well-studied clusters in this redshift range. Galaxy morphologies were measured from images taken in the F814W filter with HST/ACS. These data are described in §2.4. In §2.5 we describe our classification procedure and provide revised Hubble types for all galaxies with total magnitudes brighter than 23rd magnitude in the I band. In §3.3 we describe our method of analyzing the morphological content. Morphological fractions are presented in §2.7, and our conclusions regarding them can be found in §4.9.

Unless otherwise noted, all calculations assume $\Omega_0 = 1$, $\Lambda = 0$, and $H_0 = 50$ km s^{-1} Mpc^{-1}, to maintain consistency with previous work.

2.3 The EDisCS Sample

The EDisCS program was carried out with the goal of studying galaxy clusters to $z = 0.8$ (corresponding to a lookback time of ~9.5 Gyr) in enough detail to enable quantitative comparisons both to parallel, low-redshift studies such as the 2dF and SDSS and to N–body and semi-analytic models of structure formation. It consists of ground-based optical and infrared imaging and optical spectroscopy for nineteen intermediate redshift ($0.4 \lesssim z \lesssim 0.8$) clusters from the Las Campanas Distant Cluster Survey (Dalcanton, 1996; Zaritsky et al., 1997; Gonzalez et al., 2001, LCDCS). It is worth briefly describing the verification process of the EDisCS clusters because the LCDCS cluster candidates were selected at optical wavelengths, and optical selection can yield spurious superpositions of galaxies. Additionally, since this work draws upon the full survey, and not just the HST portion, we briefly describe the available data.

The redshifts of the LCDCS cluster candidates were initially estimated from the apparent magnitude of the brightest cluster galaxy (BCG). The candidates were divided into an intermediate redshift group ($0.45 < z_{\rm est} < 0.55$) and a high redshift group ($0.75 < z_{\rm est} < 0.85$). Ten EDisCS clusters were selected from among the brightest candidates in each of these two groups, for a total sample of twenty clusters. Shallow two-color imaging was obtained at the Very Large Telescope (VLT) to verify the presence of both a BCG of the appropriate magnitude and a red sequence. These twenty clusters were then imaged more deeply at the VLT in BVI (45 minutes) for the $z \sim 0.5$ candidates and in VRI (2 hours) for the $z \sim 0.8$ candidates. These data are presented in White et al.(in preparation). Additional infrared imaging was obtained with SOFI at the New Technology Telescope (NTT) in K_s for the

Table 2.1 Properties of the EDisCS HST Sample.

Name	RA (J2000) h:m:s	Dec (J2000) °:′:″	z	Offset	Dates of Observation	$I_{\mathrm{auto,lim}}$	Σ_{field} arcmin^{-2}	Classifiers
cl1037-1243	10:37:52.51	-12:43:45.53	0.58	SW	20 Mar – 02 Apr, 2003	21.63	3.98	AAS,VD
cl1040-1155	10:40:40.38	-11:56:04.22	0.70	NW	21 – 30 Mar, 2003	21.95	4.89	JJD,VD
cl1054-1146	10:54:24.37	-11:46:19.47	0.70	SE	23 Mar – 01 Apr, 2003	21.95	4.89	VD,BMP
cl1054-1245	10:54:43.58	-12:45:51.85	0.75	NW	19 – 27 Mar, 2003	22.04	4.89	AAS
cl1103-1245	11:03:43.04	-12:45:37.06	0.70	SE	26 Mar – 23 Apr, 2003; 11 May 2004	21.95	4.89	JJD,BMP
cl1138-1133	11:38:10.04	-11:33:37.90	0.48	SE	02 Apr – 24 Mar, 2003	21.33	2.64	JJD
cl1216-1201	12:16:45.33	-12:01:17.60	0.79	NE	01 – 18 May, 2003	22.09	4.89	AAS,VD,PJ,BMP
cl1227-1138	12:27:53.64	-11:38:17.32	0.64	NE	24 – 31 May, 2003; 4 – 24 May 2004	21.81	3.98	AAS
cl1232-1250	12:32:30.15	-12:50:36.37	0.54	SW	09 – 31 May, 2003	21.51	3.25	AAS,VD
cl1354-1230	13:54:9.712	-12:31:01.50	0.76	SE	27 May – 09 Jun, 2002	22.05	4.89	BMP

The RA, Dec coordinates are the positions of the brightest cluster galaxy. The redshift, z, was taken from Halliday et al. (in preparation). We observed a $6.5' \times 6.5'$ region in the field of each cluster. This area was first tiled by four slightly overlapping single orbit (1020 seconds) pointings of the $3.5' \times 3.5'$ ACS field of view. The center of the cluster was then imaged for an additional four orbits. In order to cover the same field of view as the EDisCS ground-based optical data, the center of each ACS mosaic is offset from the cluster center by one arcminute in the direction indicated in column 5. In column 6 we indicate the range of dates over which the observations were taken. Column 7 is the ground-based I-band limiting apparent magnitude limit used in the determination of the morphological fractions presented in this work. Column 8 contains the expected surface density of field galaxies down to $I_{\mathrm{auto,lim}}$, based on the counts presented in Postman et al. (1998). The last column contains the initials of the authors who classified galaxies in the field of each cluster.

$z \sim 0.5$ candidates and in JK_s for the $z \sim 0.8$ candidates (Aragon-Salamanca et al., in preparation). The combined optical and infrared imaging allow a determination of photometric redshifts, which is described in Pelló et al.(in preparation). An initial phase of spectroscopy consisted of relatively short exposures of a single slit mask per cluster. One cluster with an estimated redshift of $z \approx 0.8$ was revealed as a superposition of weak groups, and was rejected from the sample. Two hour ($z \sim 0.5$) and four hour ($z \sim 0.8$) exposures of 4–6 masks per cluster resulted in high quality spectra for ~50 members in each cluster. These spectra revealed that the remaining nineteen clusters have redshifts evenly distributed in the range of $0.4 \lesssim z \lesssim 0.8$. The spectroscopic observations are described in Halliday et al.(in preparation), and are of sufficient quality to obtain information about the stellar populations and dynamics of the target galaxies. Wide-field imaging data was procured at the ESO/MPG 2.2 m telescope in V (1 hour), R (2 hours), and I (1 hour). Clowe et al.(in preparation), present these data and what they reveal about the large-scale structure around the EDisCS clusters.

The ground-based EDisCS imaging and spectroscopy goes a long way towards characterizing both the clusters themselves and the galaxies within them. At the high redshifts of the EDisCS sample, however, only HST can provide the spatial resolution necessary to provide robust morphologies. Motivated by the issues discussed in §4.2, we obtained HST imaging for the 10 highest redshift EDisCS clusters. Table 2.1 provides basic physical parameters for these 10 clusters, and Figure 2.1 plots the distributions of cluster richnesses, velocity dispersions, and lookback times.

2.4 *HST/ACS Data*

The HST observations were designed to coincide as closely as possible with the coverage of the ground-based optical imaging and spectroscopy, within guide star constraints. The ground-based data cover a $6.5' \times 6.5'$ region around each cluster, with

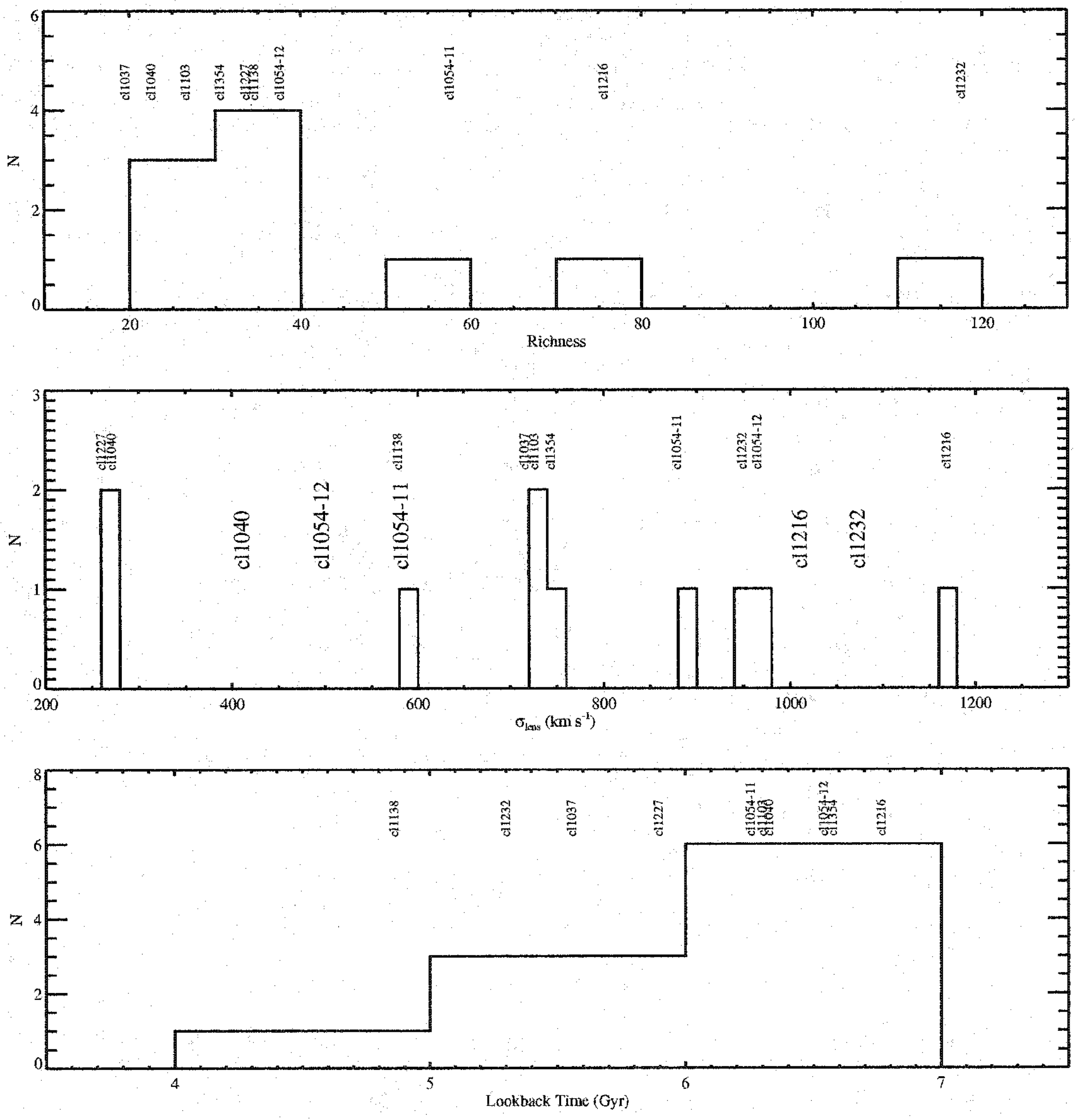

Figure 2.1 Distributions of cluster richness, velocity dispersion, and lookback time for the EDisCS HST sample. The richness is the number of red-sequence galaxies within 1 Mpc of the brightest cluster galaxy and brighter than the apparent I_{auto} which evolves passively to M_V = -18.7 at $z = 0$ (White et al., in preparation). The velocity dispersions were determined from the weak lensing signal measured from the ground-based VLT data. Velocity dispersions based on spectroscopic data are available for several EDisCS clusters; these are indicated in bold. In some cases, the labels have been shifted by a small amount in order to improve readability where they overlap.

the cluster center displaced by $1'$ from the center of the region, to avoid placing the center of the cluster in the center of the CCD. The direction of this displacement is noted in Table 2.1. For reference, the ACS WFC has a field of view of roughly $3.5' \times 3.5'$. Balancing scientific motives for going deep over the entire spectroscopic field against a limited number of available orbits, we tiled each $6.5' \times 6.5'$ field in four pointings, with one additional deep pointing on the cluster center. The deep central pointing probes to lower surface brightness, fainter magnitudes, and larger galactic radii in the region of the cluster containing the most galaxies. All exposures were taken under LOW SKY conditions to maximize our surface brightness sensitivity.

The ACS calibration pipeline, CALACS v4.3 (6-June-2003) debiased, dark-subtracted, and flat-fielded our ACS images "on the fly" when they were requested from the HST archives. Known bad pixels and saturated data were also flagged in accompanying data quality (DQ) arrays. Approximate World Coordinate System (WCS) headers were provided. The resulting images were returned by the archive with the FLT suffix. In addition, images that were cosmic-ray split were combined and returned with a CRJ suffix.

In order to produce a mosaic, we required precise offsets between the 32 FLT images retrieved for each cluster. The approximate WCS headers provided were insufficient for this purpose. We found that the offsets between cosmic-ray split images were negligible. We therefore computed the necessary shifts between pointings using the higher signal-to-noise CRJ images. The shifts could not be computed using the retrieved CRJ files because they had not been undistorted. We therefore drizzled each CRJ image separately, using the approximate WCS headers provided. Because each undistorted CRJ image overlaps the central pointing, one of the images centered on the cluster center was chosen as the reference image. Shifts between the reference image and each undistorted CRJ image were then computed using cross-correlation.

Combination of the FLT images using the resulting shifts was accomplished using *MultiDrizzle*, a Python code written by Anton Koekemoer to run under PyRAF, the

Python-based interface to IRAF. *MultiDrizzle* automatically removes cosmic rays and combines dithered images using *PyDrizzle*, which has been developed by the Science Software Branch at the Space Telescope Science Institute. For each of the 32 FLT images per cluster, *MultiDrizzle* included negative bad pixels in the data quality array, subtracted the sky, and separately drizzled and undistorted each image. Next, it created a median image from these separately drizzled images using shifts computed from the headers along with the user-supplied refinement shifts described above. This median image, relatively free of cosmic rays, was compared to the input images to identify cosmic rays. The median image was then re-distorted using *blot* in order to create cosmic ray masks. These masks were used in the final image combination step using *drizzle* and the *lanczos3* kernel, which provided optimal noise properties.

2.5 Visual Morphologies

We visually classified all galaxies brighter than $I_{\rm auto} = 23$. Here $I_{\rm auto}$ is the SExtractor AUTO magnitude measured on the I-band VLT images, and is an estimate of the total magnitude of a galaxy. This limit was set both to ensure robust classifications and to provide a tractable sample. In addition, we classified all galaxies in our spectroscopic sample, regardless of magnitude. The resulting sample contains 7393 morphologically classified galaxies, 1093 of which were observed spectroscopically.

Our classifications are most useful if they conform to systems adopted by previous studies. For this reason, each classifier trained on MORPHS data, using the same procedure described in Smail et al. (1997). The galaxies in each EDisCS cluster were classified by one or more of the authors, as indicated in Table 2.1.

For uniformity, each classifier used the same IRAF script to examine and classify EDisCS galaxies. This script displays two side-by-side versions of a 200 × 200 cutout centered on each galaxy meeting the magnitude limits described above. One version is on a log scale between -0.1 – 2 DN/s, while the other is on a log scale between -0.1

– 25 DN/s. Together, these displays allowed classifiers to inspect the galaxies from their high surface brightness cores to their low surface brightness outer features. In general, we found that the depth and quality of the EDisCS ACS data were similar to or better than the MORPHS WFPC2 data for lower redshift clusters.

For a given galaxy, the final Hubble type was based on the classifications of one or more people. First, the Revised Hubble Type was translated into a T-type according to the scheme presented in Table 2.2. Classifications appended by one colon or question mark were given half weight; those appended by two colons or question marks were given one-quarter weight. If a classifier specified two types separated by a slash, the first was given three-quarters weight and the second was given one-quarter weight. All submitted T types were then ranked. If there were two submitted classifications, one was chosen randomly. If there were three submitted classifications and two or more were identical, that one was chosen. If all three classifications were different, the differences in T types were computed between consecutive types. If there were no gaps smaller than 3 T types, the median value of the three was chosen. If there was one gap smaller than 3 T types, one of the two similar classifications was chosen at random. If there was more than one gap smaller than 3 T types, the median value of all classifications was chosen. Figure 2.2 shows the difference in Hubble T types between pairs of classifiers as a function of apparent I-band magnitude. In general, the agreement between classifiers is good. As was done in Dressler et al. (1997), galaxies that could not be assigned a Revised Hubble type were not included in the following analysis. Table 2.3 lists the numbers of galaxies classified as stars, galaxies which are too compact to classify, ellipticals, S0s, spirals, irregulars, and unclassifiable.

Following the example of MORPHS, classifiers also estimated the degree of disturbance of each galaxy, as well as an interpretation of the disturbance. Table 2.2 provides a summary of these parameters. Morphological catalogs containing classifications by individuals as well as final Hubble types can be obtained by request from the author.

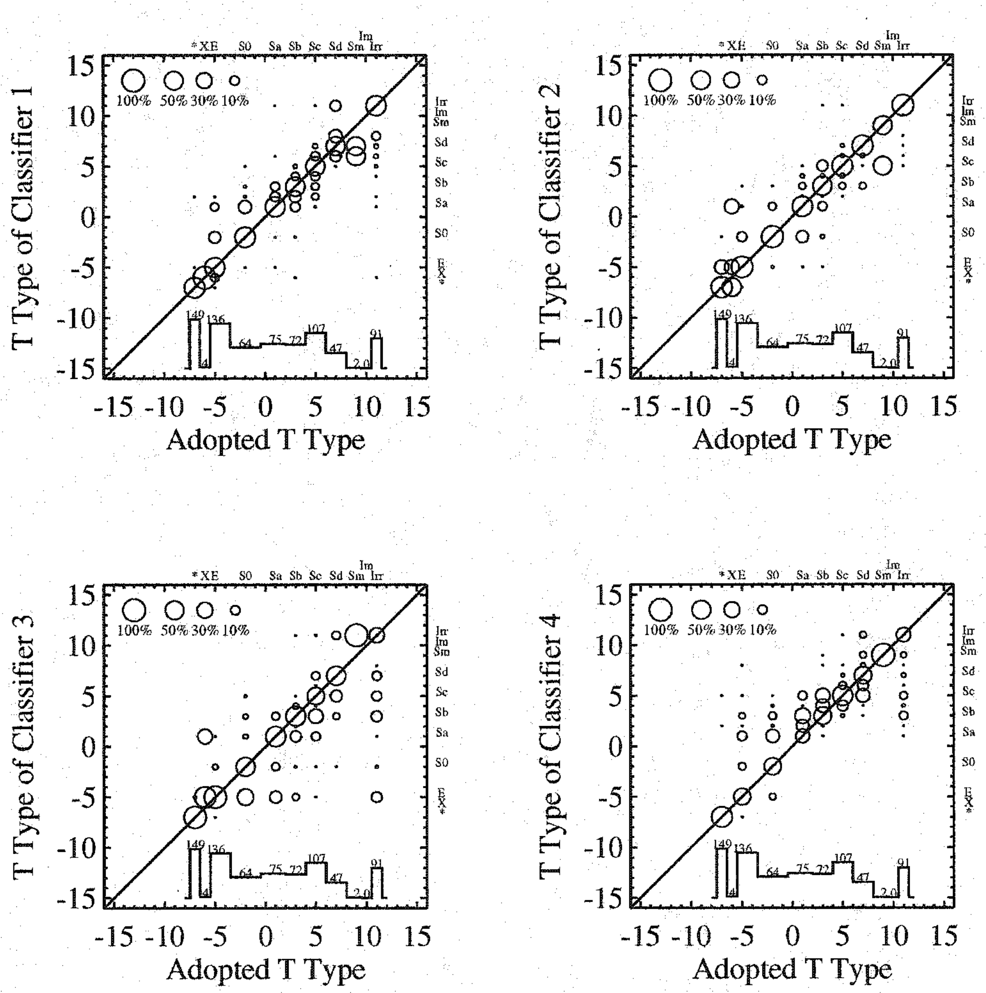

Figure 2.2 Consistency of Galaxy Classifications. The galaxies in one cluster, cl1216, were visually inspected by four of the five classifiers. Thus, we can use this cluster to assess the consistency of our classifications. Each panel is a plot of the T type assigned by a given classifier versus the consensus classification adopted by the method described in §2.5. The size of the circles is proportional to the $\log_{10}$ of the percentage of galaxies included in the point. For instance, 100% of galaxies classified as compact in the final, merged catalog were also classified as compact by Classifier 1. The histogram in each panel gives the total number of objects in the final catalog as a function of T type, and provides a sense of the significance of each point. For visual clarity, intermediate T types (Sab, Sbc, Scd, Im) have have been omitted.

Table 2.2 Notes on Parameters in Morphological Catalogs

Heading	Description
ID	EDisCS ID, as presented in Simard et al. (in preparation)
$I_{\rm auto}$	Total I magnitude; SExtractor MAG_AUTO parameter measured from ground-based I-band images and published in Simard et al. (in preparation)
Class	E – Elliptical or Spheroidal
	S(B)0 – Lenticulars, or a spheroid with an armless disk
	S(B)a
	S(B)b
	S(B)c star formation, B/D, tightness of spiral arms are all taken into account
	S(B)d
	Sm – transition stage to Magellanic Irregulars
	Im – Magellanic Irregulars
	Irr – Irregulars; galaxies which do not fit into the above classifications
	X = non-stellar but too compact to see structure
	* = stellar image
	? = unclassifiable
	Where a slash (/) is used, the first classification is deemed more likely.
T-type	E=-5, S0=-2, Sa=1, Sb=3, Sc=5, Sd=7, Sm=9, Irr=10
D	Disturbance Index:
	0 = normal
	1 = moderate asymmetry (e.g. due to distribution of HII regions)
	2 = strong asymmetry
	3 = moderate distortion (e.g. due to tidal or interaction-related features)
	4 = strong distortion
Int	Interpretation of disturbance classes:
	M = merger
	I = tidal interaction with neighbor
	T = tidal feature
	C = chaotic
Comments	Classifier's comments: If the B/D ratio is small but the disk is featureless, this is noted as "S0 featureless disk", "SB0 featureless disk", or "SO featureless disk edge-on"

Table 2.3 Summary of Classified Galaxies

Cluster Name	$N_{\rm tot}$	$N_{\rm star}$	$N_{\rm compact}$	$N_{\rm E}$	$N_{\rm S0}$	$N_{\rm Sp}$	$N_{\rm Irr}$	$N_{\rm noclass}$
cl1037-1243	831	150	48	70	35	356	66	106
cl1040-1155	670	119	35	63	17	253	112	71
cl1054-1146	838	121	36	72	17	326	56	210
cl1054-1245	577	122	16	28	35	303	55	18
cl1103-1245	502	110	8	44	16	207	50	67
cl1138-1133	696	119	14	67	46	297	149	4
cl1216-1201	914	149	4	136	64	364	91	106
cl1227-1138	791	171	15	59	33	330	148	35
cl1232-1250	869	142	99	66	37	278	139	108
cl1354-1230	722	193	0	40	25	303	20	141

Columns: $N_{\rm tot}$ is the total number of objects brighter than $I_{\rm auto} = 23$ in each cluster field. In order, the remaining columns are the number of objects classified as stars, galaxies that are too compact to properly classify, ellipticals, S0s, spirals (Sa through Im), irregulars, and unclassifiable.

2.6 Analysis

The goal of this chapter is to quantify the morphological content of the EDisCS clusters. In particular, we will discuss the overall fractions of elliptical (E), S0, and spiral (Sp) galaxies in our clusters and compare them to the fractions found in clusters at other redshifts. To facilitate a fair comparison with other samples, we compute the morphological fractions as consistently as possible with previous work. Below, we describe the key elements of our analysis.

(i) **Magnitude Range:** Early types preferentially occupy the bright end of the galaxy luminosity function, while late types dominate the faint end. Thus, morphological fractions depend upon the range of absolute magnitudes sampled. Morphological fractions in the MORPHS clusters were determined using apparent magnitude cuts in I_{814} designed to correspond to $M_V = -20 - 5\log_{10} h_{50}$ (Dressler et al., 1997), but in actuality corresponding to $M_V = -19 - 5\log_{10} h_{50}$ due to a transcription error

(Fasano et al., 2000). However, Fasano et al. (2000) re-analyzed the MORPHS data with the intended limiting absolute magnitude and additionally analyzed nine clusters with $0.1 < z < 0.25$ in the same manner, providing an ideal comparison sample for the EDisCS clusters. We therefore adopt a faint absolute magnitude limit of $M_V = -20 - 5\log_{10} h_{50}$. The apparent magnitude in the I-band is then given by

$$I_{\mathrm{auto,lim}} = M_{\mathrm{V}} + 5\log_{10}(d_{\mathrm{L,pc}}) - 5 - (k_{\mathrm{I}} - k_{\mathrm{V}}), \tag{2.1}$$

where $d_{\mathrm{L,pc}}$ is the luminosity distance is parsecs, and k_{I} and k_{V} are the k-corrections in the I and V bands, respectively. We adopted the k-corrections presented in Poggianti (1997) for an Sc galaxy. The adopted values of $I_{\mathrm{auto,lim}}$ are provided in column 7 of Table 2.1.

(ii) **Aperture:** Clusters exhibit a radial gradient in their morphological fractions: the centers of clusters contain a larger fraction of ellipticals than the outskirts. Thus, in comparing the overall morphological fractions across clusters, one must choose a consistent aperture. The MORPHS project has set the standard for the aperture within which to compute morphological fractions. Most studies of the morphological fractions of galaxy clusters at other redshifts have used a similarly-sized aperture. So that we may assess the level of evolution between the morphological studies presented in the literature and those conducted with EDisCS data, we also adhered to this precedent and adopted a circular aperture of diameter $600h_{50}^{-1}$ kpc.

(iii) **Correction of Morphological Fractions for Field Contribution:** Because the morphological mix of field galaxies differs substantially from that of cluster populations, morphological fractions computed without regard to field contamination will underestimate the fraction of early types and overestimate the fraction of late types in clusters. We can correct the observed fraction of galaxies with morphology i by using the following equation:

$$f_{i,\mathrm{corr}} = \frac{f_{i,\mathrm{obs}} - P_i P_{\mathrm{field}}}{1 - P_{\mathrm{field}}}, \tag{2.2}$$

where $f_{i,\mathrm{obs}}$ is the observed fraction of galaxies that have morphology i; P_i is the fraction of field galaxies that have morphology i; and P_{field} is the fraction of the observed galaxies that are expected to be field members.

For each cluster, we derived P_{field} through

$$\mathrm{P}_{\mathrm{field}} = \Sigma_{\mathrm{field}} A / N_{\mathrm{obs}}, \tag{2.3}$$

where A is the area of the aperture described in (ii) and N_{obs} is the total number of galaxies meeting the magnitude criterion within that aperture. The surface density of field galaxies, Σ_{field}, is determined by integrating the I-band differential number counts in Table 1 of Postman et al. (1998) down to $I_{\mathrm{auto,lim}}$. The resulting values of Σ_{field} are presented in column 8 of Table 2.1.

We computed P_i, the percent of field galaxies of each morphological type, using data from the Medium Deep Survey (MDS; Griffiths et al., 1994), a Hubble Telescope Key Project that cataloged the morphologies of intermediate-redshift field galaxies down to $I_{814} \sim 22$. In particular, we used the classifications of Richard Ellis listed in Table 1 of Abraham et al. (1996). We determined that the fraction of E/S0/Sp galaxies is 10%/10%/80% down to $I_{\mathrm{auto}} = 22$, the limiting magnitude of the MDS catalog. We assume that the fractions do not change substantially down to the magnitude limit of our analysis, $I_{\mathrm{auto}} = 23$.

(iv) **Error Analysis:** The probability of measuring a given morphological fraction is the product of the Poisson probability of measuring the total number of cluster members times the binomial probability of measuring the observed number of a given morphology. We use the approximation presented in Equations 21 and 26 of Gehrels (1986) to derive 1-σ error estimates based on this premise.

2.7 Morphological Fractions

We now compare our results with similar but lower-redshift studies in order to assess the degree of evolution in the morphological content of rich clusters of galaxies. We employ four comparison samples of clusters out to $z \sim 0.5$. These samples were originally analyzed by different groups in different ways, but have recently been reanalyzed in a uniform manner by Fasano et al. (2000). They have kindly provided these data points so that we may extend their study to higher redshifts. We briefly describe the samples in Fasano et al. (2000). The first is the previously-mentioned MORPHS sample of 10 clusters at $0.37 < z < 0.5$ (Dressler et al., 1997). The second is the Fasano sample of 9 clusters at $0.1 < z < 0.25$. The third sample consists of three clusters at $z \sim 0.3$ (Couch et al., 1998), plus A2218 and A1689 at $z = 0.18$, for which archival HST/WFPC2 data were available. Following Fasano et al. (2000), we refer to these last clusters as the C98+ sample. The fourth sample includes 55 low redshift clusters originally analyzed by Dressler (1980a) and reanalyzed by Dressler et al. (1997), and will be referred to as the D80 sample.

Figure 2.3 shows the morphological fractions measured in rich clusters as a function of redshift. The MORPHS, Fasano, C98+, and D80 clusters are plotted in black, while the higher-redshift EDisCS clusters analyzed in this chapter are plotted in red. The addition of the EDisCS clusters represents a significant increase in the lookback time over which morphological fractions have been determined; we are now probing galaxy evolution over the last half of the age of the universe.

The top panel shows the fraction of elliptical galaxies in clusters at $z < 0.8$. The cluster-to-cluster variations in the elliptical fraction at any given redshift are large, highlighting the importance of a large cluster sample. Although the fraction of ellipticals ranges from 20% to 45%, there is no systematic trend with redshift. The lack of a trend implies that cluster ellipticals were assembled earlier than $z \sim 0.8$. This result is consistent with the early formation time ($z \gtrsim 3$) found for the stellar populations of cluster ellipticals (see §2.2 of Chapter 4). However, it is in conflict with the claim by van Dokkum et al. (1999) that ~50% of ellipticals in present-day clusters were assembled via mergers since $z \sim 1$. This claim is based on the large number of mergers between luminous red galaxies found in just 1 cluster at $z = 0.83$. We examine the merging populations of the EDisCS HST sample in Chapter 4, to discern whether the result presented in van Dokkum et al. (1999) is typical.

The middle and bottom panels of Figure 2.3 show the redshift dependence of the S0 and Sp+Irr fractions, respectively. Both fractions range from 0% to 60% over the probed redshift range. Even given the large scatter, it is clear that the S0 and Sp+Irr populations vary systematically with redshift: the S0 fraction has increased over the last 7.5 Gyr and the Sp fraction has decreased commensurately. This systematic change with redshift supports the idea that infalling spiral galaxies are being transformed into S0 galaxies. Most of the change in these fractions has occurred over the redshift range $0.2 < z < 0.4$. At higher redshifts the S0 fraction flattens to a typical value of ~10%, while the spiral fraction at high redshift is approximately 50%.

The largest source of systematic error in the morphological fractions plotted in Figure 2.3 arises from the background subtraction. Figure 2.4 illustrates the effects of adopting different field morphological ratios (P_i; see §3.3). Instead of using $P_i = 10\%$, 10%, 80% for E, S0, and Sp+Irr galaxies, respectively, this figure was constructed using $P_i = 15\%$, 15%, 70%. Although the individual morphological fractions are affected, the overall trends remain.

As previously noted, the morphological fractions presented in Figure 2.3 exhibit a large scatter at any given redshift. Given the large error bars, the data are consistent with there being a single universal morphological fraction at each redshift. However, we consider this possibility unlikely given both the young ages of the clusters and the evidence for correlations between morphological fractions and global cluster properties at $z = 0$ (see §4.2). Similarly, the clusters with low S0/E ratios in the Fasano sample

Table 2.4 Morphological Fractions within EDisCS Clusters

Cluster	f_{E}	σ_{l}	σ_{u}	f_{S0}	σ_{l}	σ_{u}	$f_{\mathrm{Sp+Irr}}$	σ_{l}	σ_{u}
cl1037	0.29665	0.12437	0.15496	0.00000	0.00000	0.10760	0.70335	0.15496	0.12437
cl1040	0.49398	0.16580	0.16689	0.00000	0.00000	0.12880	0.50602	0.16689	0.16580
cl1054-11	0.27262	0.07653	0.09012	0.04074	0.02894	0.06267	0.68664	0.09172	0.08065
cl1054-12	0.34925	0.10016	0.11288	0.27700	0.09175	0.11078	0.37375	0.10248	0.11310
cl1103	0.51733	0.21084	0.20605	0.17895	0.12620	0.22351	0.30372	0.16907	0.22477
cl1138	0.20461	0.09219	0.12679	0.25216	0.10145	0.12998	0.54322	0.13110	0.12627
cl1216	0.38908	0.07307	0.07775	0.14505	0.04956	0.06532	0.46587	0.07619	0.07763
cl1227	0.45992	0.14118	0.14670	0.11161	0.07329	0.13412	0.42847	0.13822	0.14810
cl1232	0.29577	0.06840	0.07749	0.21746	0.06061	0.07339	0.48677	0.07855	0.07914
cl1354	0.42134	0.23181	0.26265	0.57866	0.26265	0.23181	0.00000	0.00000	0.25143

Columns: The first three columns after the cluster name are, respectively, the elliptical fraction, the size of the lower error bar on this fraction, and the size of the upper error bar on this fraction. These are followed by the same three quantities for the S0 fraction and then for the Sp+Irr fraction.

at $0.15 < z < 0.25$ have higher physical concentrations of elliptical galaxies. In Figure 2.5 we plot the S0/E (top panel) and S0/Sp (bottom panel) ratios for the MORPHS, Fasano, C98+, and D80 clusters (black points), as well as for the EDisCS clusters (red points, tabulated in Table 2.5) as a function of redshift. Fasano et al. (2000) determined the concentrations of the first 4 samples. Their high concentration clusters are represented with filled points, and their low concentration clusters are represented with hollow points. The concentrations of the EDisCS clusters have not yet been determined, due to the limited field of view afforded by the VLT and HST data. However, the large scatter is certainly suggestive of intrinsic variations in the morphological mix, as is the obvious variation among the cluster morphologies seen in Figures 2.6 through 2.10. Upcoming wide-field imaging will be used to determine the concentrations of the EDisCS clusters, and to measure the extent to which scatter in these ratios is due to variations in cluster morphology.

Table 2.5 E/S0 and S0/(Sp+Irr) in EDisCS Clusters

Cluster	$N_{\mathrm{S0}}/N_{\mathrm{E}}$	σ_{l}	σ_{u}	$N_{\mathrm{S0}}/N_{\mathrm{Sp+Irr}}$	σ_{l}	σ_{u}
cl1037	0.00000	0.00000	0.20848	0.00000	0.00000	0.08793
cl1040	0.00000	0.14332	0.15164	0.00000	0.00000	0.14803
cl1054-11	0.14945	0.15763	0.17953	0.05934	0.03443	0.07032
cl1054-12	0.79314	0.45792	0.40586	0.74116	0.34983	0.37623
cl1103	0.34592	0.54606	0.42430	0.58921	0.57954	0.73851
cl1138	1.23240	1.08517	0.81217	0.46420	0.22746	0.27671
cl1216	0.37281	0.16297	0.17638	0.31135	0.11638	0.14539
cl1227	0.24267	0.24684	0.25942	0.26049	0.17513	0.27911
cl1232	0.73524	0.31533	0.30546	0.44675	0.15209	0.17549
cl1354	1.37338	1.93062	1.11560	0.00000	0.00000	0.00000

Columns: The first three columns after the cluster name are, respectively, the S0 to elliptical ratio, the size of the lower error bar on this ratio, and the size of the upper error bar on this ratio. The last three columns are the same quantities for the S0 to Sp+Irr ratio.

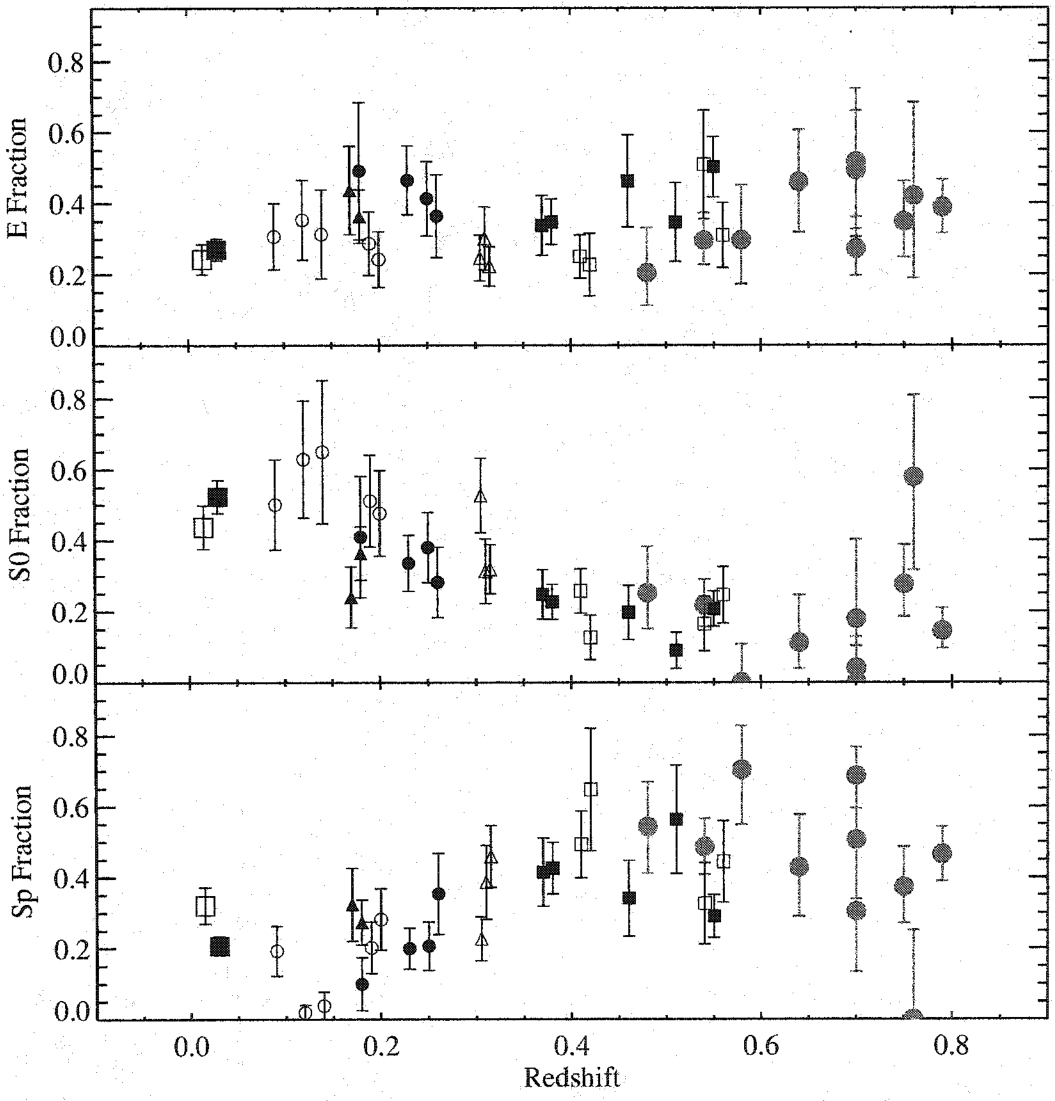

Figure 2.3 The evolution of the E, S0, and Sp+Irr fractions in rich clusters. EDisCS clusters are plotted in red; the Fasano sample is plotted as black circles; MORPHS clusters are small squares; triangles represent the C98+ sample; and the large squares represent the D80 sample. For non-EDisCS data, concentrated clusters are represented by filled points, while less concentrated clusters are represented by hollow points. The EDisCS clusters are all solid, as our current data do not allow us to calculate the concentration accurately.

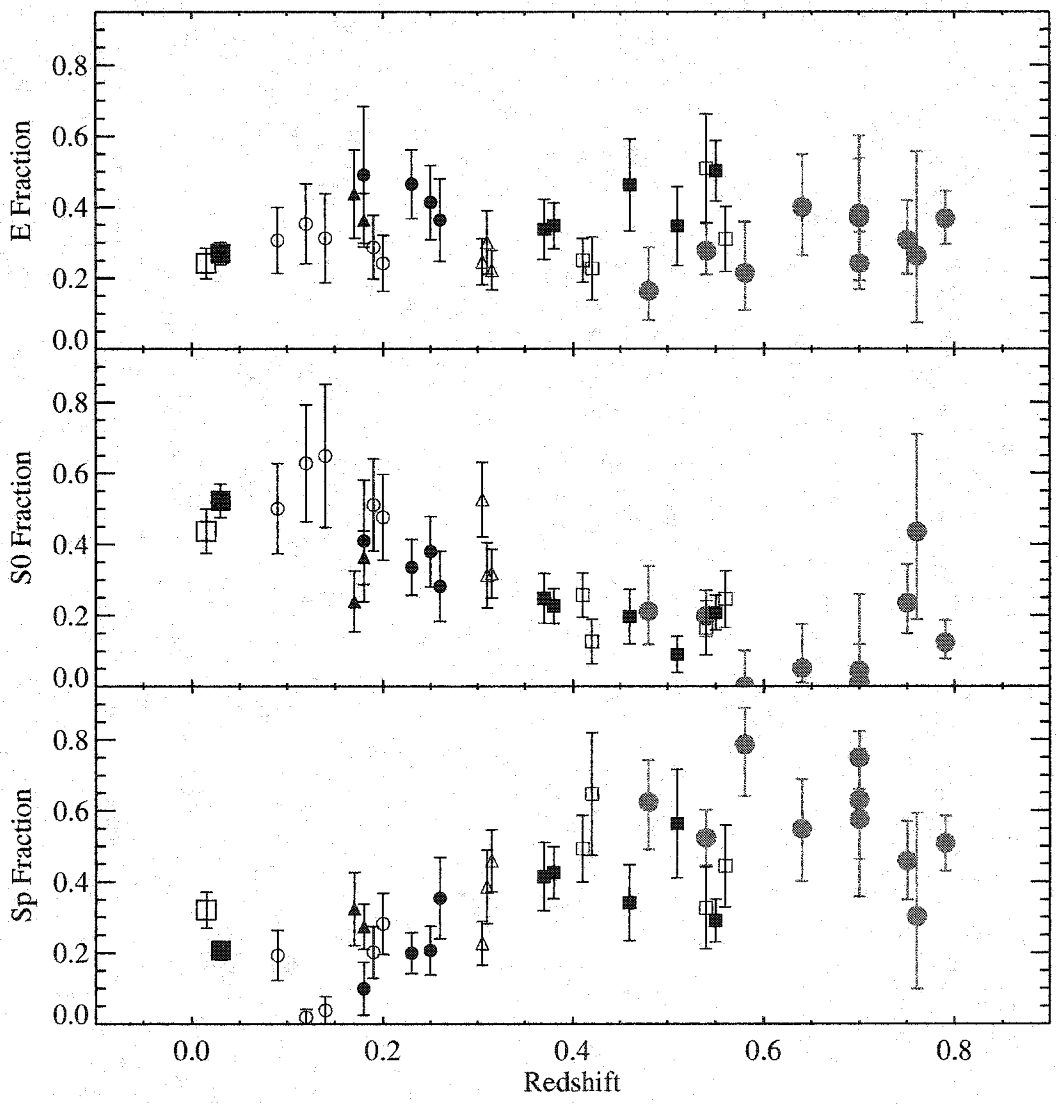

Figure 2.4 Same as Figure 2.3, but with the proportions of field galaxies set to 15%/15%/70% for E, S0, and Sp+Irr galaxies, respectively.

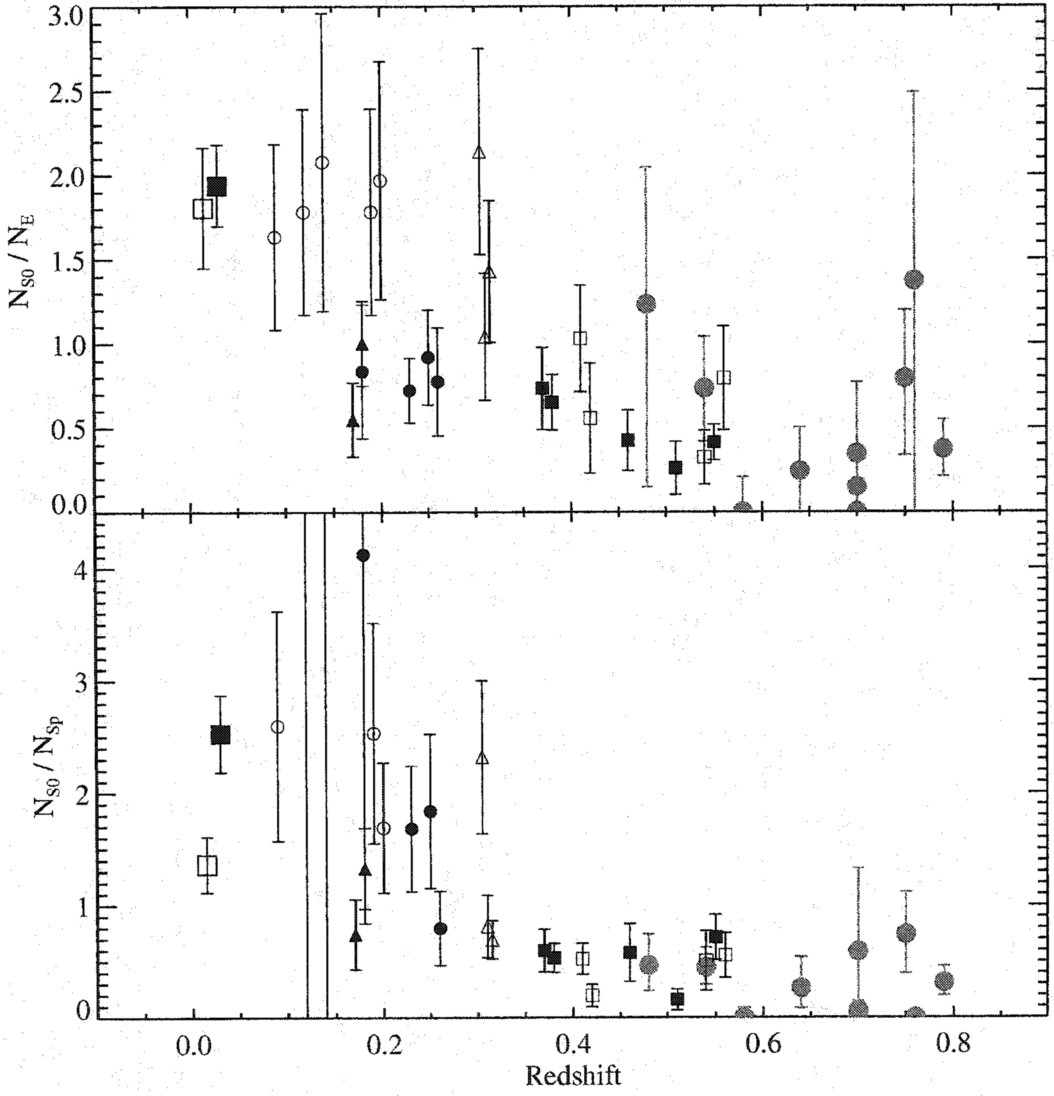

Figure 2.5 Evolution of the E/S0 and S0/(Sp+Irr) ratios in rich clusters. Symbols are as in Figure 2.3. The high concentration clusters (filled symbols) clearly have a systematically lower fraction of S0s compared to ellipticals. Some of the scatter among the EDisCS clusters (red points) may be due to a continuation of this trend to higher redshift.

Figure 2.6 VLT Color Composites of cl1037 and cl1040. Each image is $3' \times 3'$ and is centered on the BCG. North is at the top and east is to the left.

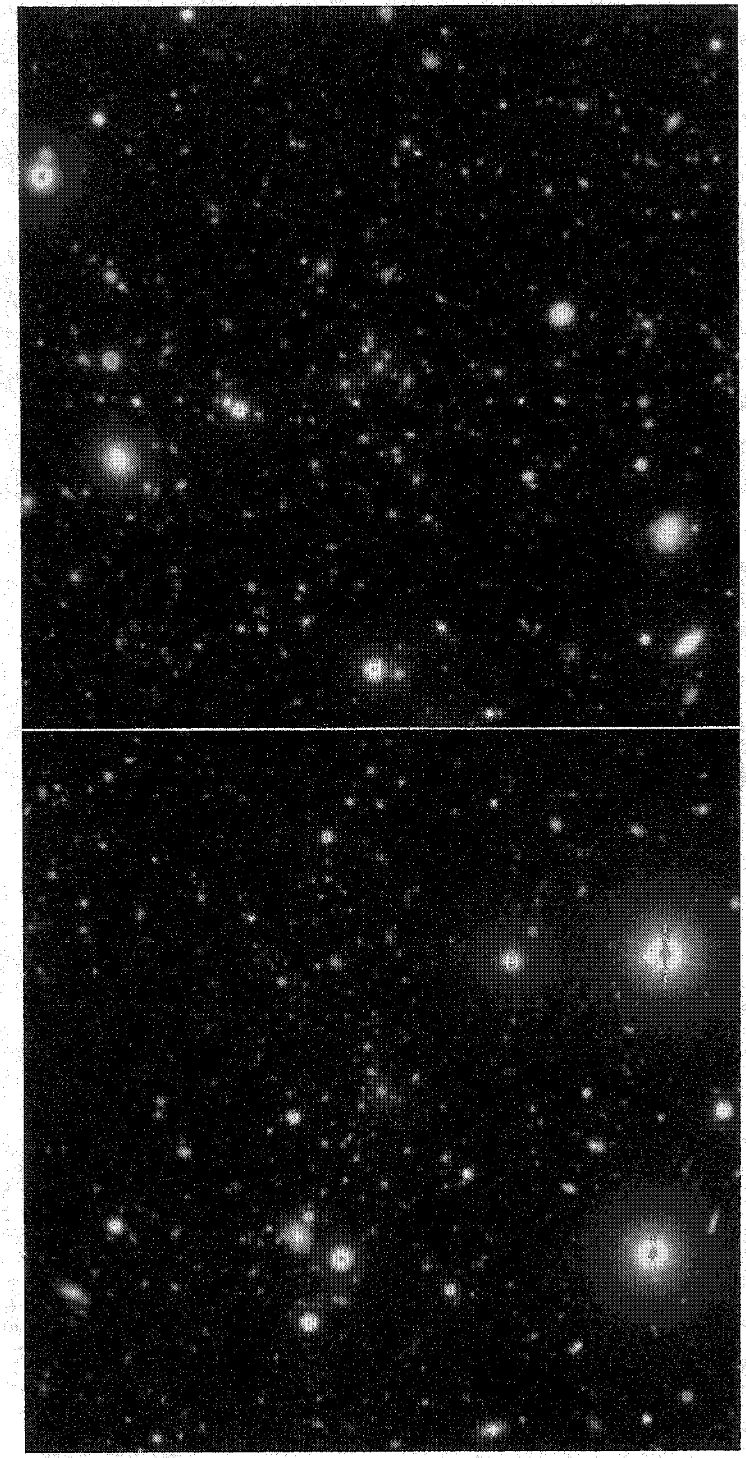

Figure 2.7 VLT Color Composites of cl1054-11 and cl1054-12. Each image is $3' \times 3'$ and is centered on the BCG. North is at the top and east is to the left.

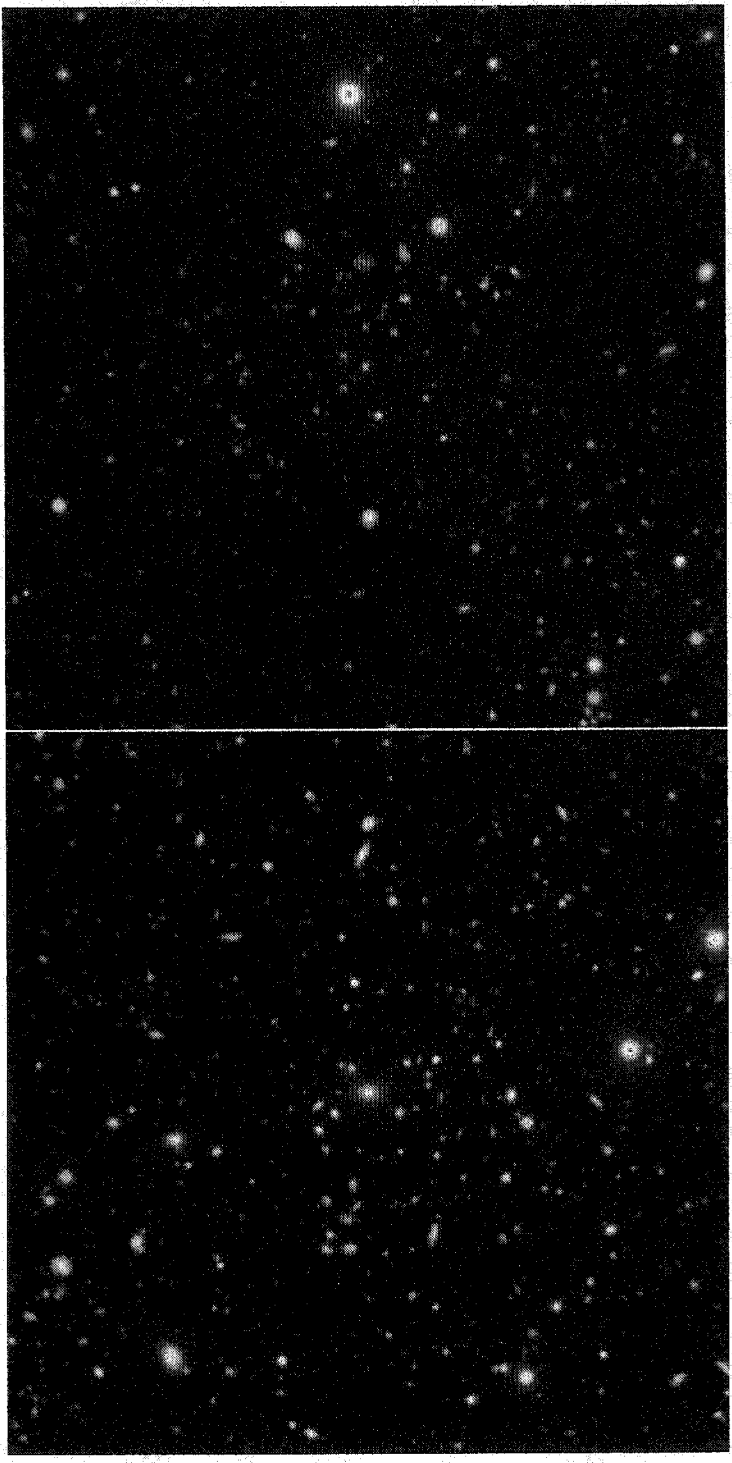

Figure 2.8 VLT Color Composites of cl1103 and cl1138. Each image is $3' \times 3'$ and is centered on the BCG. North is at the top and east is to the left.

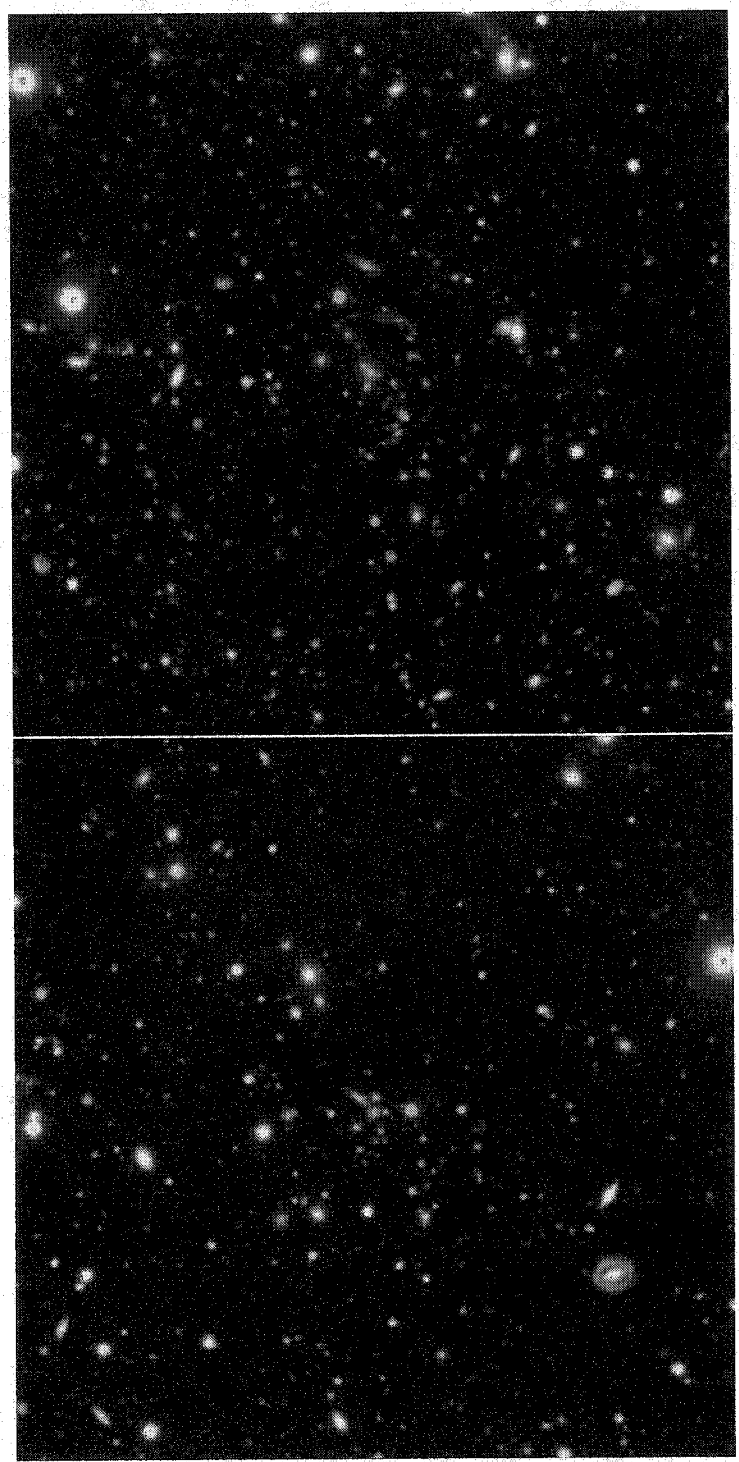

Figure 2.9 VLT Color Composites of cl1216 and cl1227. Each image is $3' \times 3'$ and is centered on the BCG. North is at the top and east is to the left.

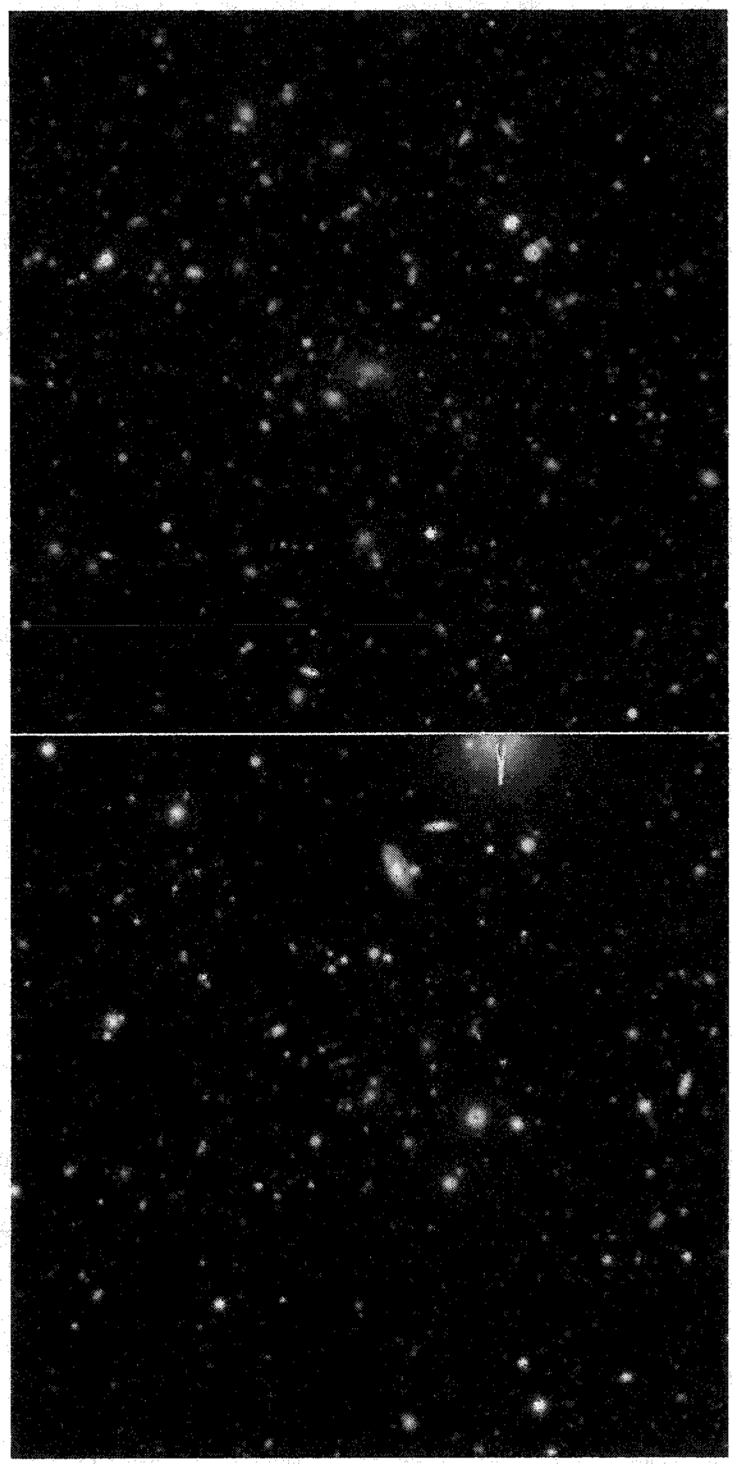

Figure 2.10 VLT Color Composites of cl1232 and cl1354. Each image is $3' \times 3'$ and is centered on the BCG. North is at the top and east is to the left. Note that cl1232 was observed in different bands, and has a different color scale than the other clusters.

2.8 Summary

We have presented morphological catalogs for ∼7000 galaxies in the fields of ten EDisCS clusters at $0.4 < z < 0.8$. These catalogs will be useful for many studies of galaxy evolution in the cluster environment.

In this chapter, we have compared the morphological fractions in EDisCS clusters to those measured in lower redshift clusters. Our findings can be summarized as follows:

1. The elliptical fraction has remained relatively constant since $z \sim 0.8$, suggesting that cluster ellipticals formed at an earlier epoch. This result is consistent with the old ages found for the stars in ellipticals, but may be at odds with recent results implying that a significant fraction of ellipticals have formed via mergers since $z \sim 1$.

2. Since $z \sim 0.8$ the S0 fraction has systematically increased at the expense of the Sp+Irr fraction, strongly suggesting that late-type galaxies have transformed into S0 galaxies within the cluster environment.

3. The large cluster-to-cluster variations in the observed morphological fractions may be due to variations in the spatial concentration of cluster galaxies. A full analysis of such an affect will be carried out with upcoming wide-field imaging data, which will allow a more accurate assessment of cluster concentration in comparison to current resources.

2.9 Acknowledgments

We greatly appreciate the timely and cheerful assistance of Galina Soutchkova in planning the HST observations. We also warmly thank Giovanni Fasano for providing the non-EDisCS data points for Figures 2.3 through 2.5. Many thanks to Andrew

West for help with spherical geometry. VD acknowledges funding from the Graduate Student Researchers Program. This work was supported by NASA grant HST-GO-09476.01. JJD was partially supported by the Alfred P. Sloan Foundation. The Medium Deep Survey catalog is based on observations with the NASA/ESA Hubble Space Telescope, obtained at the Space Telescope Science Institute, which is operated by the Association of Universities for Research in Astronomy, Inc., under NASA contract NAS5-26555. The Medium-Deep Survey analysis was funded by the HST WFPC2 Team and STScI grants GO2684, GO6951, GO7536, and GO8384 to Prof. Richard Griffiths and Dr Kavan Ratnatunga at Carnegie Mellon University.

Chapter 3

THE MORPHOLOGY-DENSITY RELATION IN TEN EDISCS CLUSTERS AT $0.4 < z < 0.8$

3.1 Abstract

The morphologies of galaxies in nearby clusters have long been known to differ from those of the general galaxy population. These differences have been generalized to a relation between the local environment of a galaxy and its morphology. Specifically, the fraction of elliptical galaxies increases with local density, while the late-type fraction decreases, and the S0 fraction remains flat. The morphology-density relation and its evolution provide important constraints on models of the environmental dependence of galaxy evolution. In this chapter, we investigate the dependence of galaxy morphology on local galaxy density for 10 clusters at $0.4 < z < 0.8$. These clusters were observed with the Advanced Camera for Surveys (ACS) on board the Hubble Space Telescope (HST) as part of the larger ESO Distant Cluster Survey (EDisCS). We found that the morphology-density relation was already in place 7.5 billion years ago. We then compared this high-redshift relation to that found in the 10 intermediate redshift ($0.37 < z < 0.6$) MORPHS clusters and the 55 low redshift clusters assembled by Dressler (1980a,b). At all densities, the EDisCS clusters exhibit a lower fraction of ellipticals than both of these lower redshift samples. We discuss possible reasons for this offset. Finally, we compare our results to recent work on the morphology-density relation in even higher redshift ($z \sim 1$) clusters (Smith et al., 2004). Several independent lines of evidence imply that spirals infalling onto clusters can be transformed into S0 galaxies. Smith et al. (2004) claim to have observed a

dependence of the rate of galaxy transformation upon density. We provide arguments against this interpretation of the data.

3.2 Introduction

The environmental dependence of galaxy evolution is a subject that has received much attention from observers and theorists in recent years, but is still poorly understood. It has long been recognized that the fraction of early-type galaxies (ellipticals and S0s) is higher in nearby rich clusters than in the general field (Spitzer & Baade, 1951). The morphological mix of galaxies within clusters also seems to vary systematically with the structure of the cluster. The more compact and relaxed a cluster, the more dominant the early-type population (Abell, 1965; Oemler, 1974). Gunn & Gott (1972) suggested that the structure of a cluster is indicative of its dynamical state: regular clusters are more evolved than irregular clusters. Based on this supposition they introduced the idea that the cluster environment could trigger the transformation of infalling spiral galaxies into S0 galaxies. In their ram-pressure stripping model, the hot intracluster medium strips gas from spiral disks, which then fade into the small, featureless disks associated with S0 galaxies. This transformation would be more complete in dynamically evolved clusters, leading to the observed dependence of galaxy morphologies on cluster structure.

The morphological mix varies not only with cluster structure, but also with clustercentric radius within a given cluster. This effect was first observed by Melnick & Sargent (1977), who explored the radial distribution of Hubble types within six nearby X-ray clusters and found that the fraction of early-types increases towards the cluster center. Additionally, they noted a correlation between cluster velocity dispersion and the S0 fraction. Both results are expected if ram-pressure stripping transforms spirals into S0s.

The centers of very irregular clusters are difficult to define, motivating Dressler

(1980a,b) to explore the relationship between galaxy morphology and local galaxy surface density, rather than radius, within 55 nearby clusters. He found that galaxy morphology correlates more closely with density than with radius, in the sense that early-type galaxies are preferentially found in high-density regions. He noted that the morphology-density relation exists even for irregular clusters, where ram-pressure stripping should be inefficient. He also argued that the bulges and bulge-to-disk ratios of S0 galaxies are larger than those of spiral galaxies at all densities, although this has been disputed by Solanes et al. (1989). Finally, he presented the alternative idea that a high local galaxy density may hinder the slow growth of disks.

The local morphology-density relation extends to low density environments. Postman & Geller (1984) observed that the population fractions are independent of density for densities less than 5 galaxies Mpc^{-3}, the fraction of S0 galaxies becomes greater than the fraction of spiral galaxies at a density of 600 galaxies Mpc^{-3}, and the elliptical fraction rises steeply at densities greater than 3000 galaxies Mpc^{-3}. They noted that the dynamical time in a given region is dependent upon the local density. Therefore, the three density regimes can be understood by realizing that the dynamical time is comparable to the Hubble time over the range of densities which show no morphological dependence. When the density is high enough, the dynamical time becomes less than a Hubble time, and the environment can affect galaxy morphologies. Echoing Dressler (1980b), they argued that at the highest densities, the collapse time is shorter than the time scale required for disk formation. More recently, Goto et al. (2003) used Sloan Digital Sky Survey data to study the morphology-density relation out to the low-density field. Their results were qualitatively similar to those of Postman & Geller (1984).

Helsdon & Ponman (2003) studied the morphology-density relation in nearby groups. They found that only when the group relation is corrected for the higher expected merging rate does the group morphology-density relation join smoothly with that of clusters. This suggests that the morphology-density relation may be driven by two-body interactions. They also found that the fraction of S0 galaxies in X-ray-bright groups is as high as in clusters. However, group S0s are not likely to be the product of ram-pressure stripping.

The morphology-density relation has also been studied in the cores of clusters at higher redshifts. Using HST/WFPC2 observations of the MORPHS clusters at $0.37 < z < 0.6$, Dressler et al. (1997) found that the relation exists only in regular clusters. In a ground-based study of 9 clusters at $0.1 < z < 0.25$, Fasano et al. (2000) confirmed that it was established in irregular clusters only within the last 1–2 Gyr.

The dependence of galaxy morphology on local density has just begun to be studied in low-density regions at high redshift. Treu et al. (2003) extended the morphology-density relation of one of the $z \sim 0.4$ MORPHS clusters out to 5 Mpc, spanning 3 orders of magnitude in local projected density. The observed fraction of early-type galaxies falls steeply out to 1 Mpc, and then more gradually until it asymptotes to the field value. The authors suggested that the shallow gradient outside of the cluster virial radius is most likely explained by the starvation of galaxies within small groups. Starvation occurs when a galaxy's halo gas becomes unavailable to replenish disk star formation, and can explain the observed homogeneity of cluster ellipticals and S0 galaxies. Also, the scatter in the local density at any given radius outside 0.5 Mpc is large, and is small only in the centers of the clusters. Therefore, it seems that infalling subgroups remain intact until they reach the center of the cluster. Smith et al. (2004) also measured the morphology-density relation over three orders of magnitude in galaxy density, but at $z \sim 1$. They found that the morphology-density relation was established at $z \sim 1$, and that it is similar to that observed at $z \sim 0.5$, but shallower than that observed at $z \sim 0$.

In this chapter we analyze the morphology-density relation within 10 high-redshift clusters ($0.4 < z < 0.8$) drawn from the ESO Distant Cluster Survey (EDisCS). The EDisCS HST mosaics extend to clustercentric radii of approximately 2 Mpc. Thus, these data represent a large increase in the amount of high-resolution imaging data in the outskirts of high-redshift clusters. The details of the survey, together with the determination of galaxy morphologies, are described in detail in Chapter 2. In §3.3 we describe our method of determining the morphology-density relation. In §3.4 we present the resulting relations both for each individual cluster and for various combinations of clusters, and compare the results to other work at lower and higher redshift. Our conclusions are summarized in §4.9.

3.3 Analysis

We will present the morphology-density relation as a plot of the fraction of elliptical galaxies as a function of local galaxy surface density. Below we describe the details of our determinations of the elliptical fraction and the local galaxy surface density.

(i) **Magnitude Range:** Because the luminosity function varies systematically with galaxy morphology, morphological fractions depend upon the magnitude range considered. For consistency with previous work, we adopt a faint absolute magnitude limit of $M_V = -20 - 5\log_{10} h_{50}$. The corresponding I-band total apparent magnitudes were computed in §1.6 of Chapter 2, and can be found in Table 2.1 of that chapter.

(ii) **Calculation of Local Galaxy Density:** In order to compute the morphology-density relation, we require an estimate of the local surface density of all cluster members satisfying the magnitude cut described in (i). We use a method similar to that described in Dressler et al. (1997). For each galaxy, regardless of cluster membership, we calculate the area of the circular aperture with a radius equal to the angular distance α to the tenth nearest neighbor. Taking into account spherical geometry, the area of this aperture is:

$$A = 2\pi(1 - \cos(\alpha)). \tag{3.1}$$

We make a zeroth-order estimate of the density by simply dividing the number of galaxies within the aperture (11) by this area. However, if α is longer than the distance between the galaxy and the edge of the chip, this density estimate will be incorrect and the galaxy is not included in the sample. For galaxies in extremely high densities, the area encompassing the ten nearest neighbors will be small and will contain a small number of field galaxies. Therefore, the zeroth-order density will be fairly accurate. However, the zeroth-order densities calculated for galaxies in low density regions will be severely biased by field galaxy contamination. We therefore correct the zeroth-order densities to account for field contamination. Based on the surface density of field galaxies listed in Table 2.1 of Chapter 2, we compute $N_{\rm field}$, the number of field galaxies expected within the area encompassing the ten nearest neighbors. The corrected density is then computed as

$$\Sigma_{\rm corr} = (11 - N_{\rm field})/A. \tag{3.2}$$

When the numerator is negative, $\Sigma_{\rm corr}$ is set to zero. This happens for about 6% of galaxies.

(iii) **Correction of Morphological Fractions for Field Contribution:** In §1.6 of Chapter 2, we discussed the correction of the global morphological fractions for field contamination. The correction of morphological fractions as a function of density is identical except for the determination of $\mathrm{P}_{\rm field}$, the fraction of the observed galaxies that are expected to be field members. Assuming a uniform surface density of field galaxies, $\mathrm{P}_{\rm field}$ can be computed as:

$$P_{\rm field} = \frac{\Sigma_{\rm field}}{\Sigma_{\rm corr} + \Sigma_{\rm field}}, \tag{3.3}$$

where $\Sigma_{\rm field}$ is the expected field galaxy surface density and $\Sigma_{\rm corr}$ is the measured, field-corrected local galaxy surface density.

(iv) **Error Analysis:** See §1.6 of Chapter 2.

3.4 EDisCS Morphology-Density Relation

In Figure 3.1 we show the fraction of ellipticals as a function of local galaxy surface density for each individual EDisCS cluster. The data show strong variations from cluster to cluster, with some (cl1037, cl1040, cl1216) showing an obvious increase in the elliptical fraction at high densities and others (cl1103, cl1138, cl1354) showing weak or non-existent trends. The large error bars in this figure highlight the necessity of using a large sample of clusters to study the morphology-density relation. Therefore, we use all ten clusters to plot the same relation as the dark histogram with error bars in the bottom panel of Figure 3.2. The field corrections, which depend upon the apparent magnitude limit, were computed separately for each cluster. Because of our large field of view, we are able to probe to lower densities than was possible with the MORPHS clusters. From this figure, we can see that the ellipticals within the EDisCS clusters display a clear morphology-density relation: there is a steep increase in the elliptical fraction for $\log_{10}(\Sigma[\mathrm{Mpc}^{-2}]) \gtrsim 2$. In Chapter 2 we showed that the global elliptical fraction in clusters has remained constant since $z \sim 0.8$, implying that the majority of cluster ellipticals formed very early. Not only were the ellipticals already in place at $z \sim 0.8$, corresponding to a lookback time of 7.5 Gyr, but they have already segregated from the other Hubble types.

We now investigate differences in the morphology-density relations of various subsets of the EDisCS sample. First, we omit cl1037 from the analysis in Figure 3.3 because it may have an erroneous redshift. Although the spectroscopy shows a peak at the adopted redshift, the color-magnitude diagram shows a weak red sequence at the corresponding magnitude and a stronger red sequence at bluer colors (White et al., in preparation). The omission of cl1037 does not have a strong effect on the morphology-density relation.

Because the EDisCS clusters span a relatively large range of lookback times (see Figure 2.1 in Chapter 2), we divide the sample into high- and low-redshift subsamples. The high-redshift sample consists of cl1227, cl1054-11, cl1103, cl1040, cl1054-12, cl1354, and cl1216, and the corresponding morphology-density relation is plotted in Figure 3.4. The main change in the relation occurs at high densities, where the steep increase in the elliptical fraction does not occur until the highest density bin, which is populated by less than 10 galaxies.

The low-redshift sample consists of cl1138, cl1232, and cl1037, and the corresponding morphology-density relation is plotted in Figure 3.5. Although the error bars are large due to the much smaller number of galaxies, there is the suggestion of an anti-correlation between the elliptical fraction and the surface density over the range $\log_{10}(\Sigma[\mathrm{Mpc}^{-2}]) \lesssim 2$. However, the familiar sharp increase in the elliptical fraction can be seen at $\log_{10}(\Sigma[\mathrm{Mpc}^{-2}]) \gtrsim 2$.

The field correction of both the elliptical fractions and the galaxy surface densities assume that the surface density of field galaxies is uniform over the area of the imaging. This will not be the case if there are clusters at different redshifts within the same field-of-view of the EDisCS clusters. Only 5 of the clusters have complete spectroscopy which can be used to detect such structures: cl1040, cl1054-11, cl1054-12, cl1216, and cl1232. Their redshift histograms are presented in Halliday et al. (in preparation). The only cluster which shows significant structure at redshifts substantially different from the EDisCS cluster is cl1040. In Figure 3.6 we plot the morphology-density relation for the other four clusters, which have clean redshift histograms. These four clusters produce a relation which has a more constant slope than the relation produced with all 10 EDisCS clusters. These clusters also happen to be the four richest clusters, and the clusters with the highest velocity dispersions, as determined through weak-lensing (see Figure 2.1 in Chapter 2).

It is easy to see that the cluster sample can have a significant impact on the shape of the morphology-density relation. This is not surprising, since Dressler et al. (1997) found that concentrated clusters have a very different morphology-density relation than unconcentrated clusters. It is therefore imperative to characterize the global properties of the input clusters. At its conclusion, the EDisCS program, with its spectroscopic, wide-field imaging, and X-ray facets, should provide further insight into the global properties which most affect the density segregation of elliptical galaxies.

3.4.1 Comparison with Lower-Redshift Relations

Figure 3.2 plots not only density dependence of the elliptical fraction, but also the S0 fraction for the EDisCS clusters (dotted line), the approximate E+S0 fraction for galaxies at $z \sim 1$ (solid line without error bars; Smith et al., 2004), the elliptical fraction for the high-concentration MORPHS clusters (light shading), and the elliptical fraction for all 55 low redshift clusters studied by Dressler (1980a,b) (D80; dark shading). The EDisCS morphology-density relation exhibits two main differences from the relations found in the lower redshift clusters. First, the lower-redshift relations display a fairly constant slope, while the EDisCS relation appears to flatten at densities $\log_{10}(\Sigma[\mathrm{Mpc}^{-2}]) \lesssim 2$. Second, the elliptical fraction appears to be systematically lower in the EDisCS clusters.

The first difference may be due to the fact that we have not isolated the high-concentration EDisCS clusters in plotting Figure 3.2. The morphology-density relation of the MORPHS clusters also flattens at $\log_{10}(\Sigma[\mathrm{Mpc}^{-2}]) \lesssim 2$ when the low-concentration clusters are included (see Figure 4 of Dressler et al. (1997)). We plan to investigate the dependence of the morphology-density relation on cluster concentration using our wide-field imaging data, since an accurate estimate of concentration requires a wide field of view.

The comparatively low elliptical fraction in the EDisCS clusters may have several explanations. First, it could be the result of intrinsic cluster-to-cluster variations in the morphological mix. In Chapter 2 we found that the global morphological fractions can vary significantly from cluster to cluster. Second, the discrepancy could be due to systematic classification differences. The EDisCS S0 morphology-density relation is relatively flat, but has a slight excess over the density range where the elliptical fraction shows the largest deficit. We are currently undertaking a study of the elliptical versus S0 classifications of both the EDisCS and MORPHS clusters to address this possibility.

3.4.2 Comparison with Higher-Redshift Relation

Smith et al. (2004) recently used HST WFPC2 archival observations of clusters at $0.75 < z < 1.25$ to perform the only other analysis of the morphology-density relation at $z > 0.6$. They extended their analysis to low densities by using photometric redshifts to isolate the field galaxies in the wide-field HST mosaic of the MORPHS cluster cl0024 (Treu et al., 2003). They did not distinguish between elliptical and S0 galaxies, choosing instead to determine the fraction of all early-type galaxies (E+S0) as a function of local galaxy surface density. As can be seen in Figure 3.2, the Smith et al. (2004) morphology-density relation (solid line without error bars) is much higher than the EDisCS relation, even when the EDisCS S0 and elliptical galaxies are lumped together. How can our low early-type fractions be reconciled with the higher values observed by Smith et al. (2004)? There are at least two possibilities:

1. The EDisCS clusters appear to be spiral-rich compared to the Smith et al. (2004) clusters. It would be interesting to test whether this discrepancy can be linked to differences in the dynamical states of clusters in the two samples.

2. There may be a systematic difference in the classifications between the two samples, due both to the different sets of classifiers and to differences in the data sets used. Our exposure times with ACS ranged from 5100 seconds in the cluster center to 1020 seconds in the cluster outskirts. The set of clusters used by Smith et al. (2004) had WFPC2 exposures ranging from 6500 seconds to 28000 seconds. While the exposure times used in the Smith et al. (2004) work are longer, a) their clusters extend to significantly higher redshift, b) the ACS is a factor of four times more sensitive than the WFPC2, and c) the EDisCS

clusters were observed under the LOW-SKY constraint, which means that the sky background was minimized. In a future work, we will evaluate the relative surface brightness limits of these different data sets to determine if they could be responsible for differences in classifications.

If the morphology-density relation presented by Smith et al. (2004) turns out to be correct, what can be said about the environmental dependence of galaxy formation? In comparing their $z \sim 1$ morphology-density relation to those derived at lower redshifts, Smith et al. (2004) found the interesting result that the early-type fraction has increased steadily since $z \sim 1$ in the densest regions ($\Sigma = 1000$ Mpc^{-2}), has increased only since $z \sim 0.5$ in moderate density regions ($\Sigma = 100$ Mpc^{-2}), and has remained constant at ~0.4 since $z \sim 1$ in the lowest density regions ($\Sigma < 10$ Mpc^{-2}). They suggested two effects which could result in this differential evolution in the early-type fraction. The first is related to the hierarchical nature of structure growth. The densest regions at any redshift collapsed the earliest. Therefore, the densest regions have been dense for the longest time. Thus, if environmental processes can modify a universal initial mix of morphologies (most likely through a transformation from late to early types), these processes would have had a longer time to operate in increasingly dense regions. Secondly, the efficiency of such transformations could well be density-dependent. An example would be ram-pressure stripping.

While these arguments are compelling when ellipticals and S0 galaxies are grouped together, they become incomplete when these groups are considered separately. Smith et al. (2004) comment that measurements of the S0 fraction at lower redshifts are limited to higher density regimes than those they considered. However, the low-redshift clusters reanalyzed by Dressler et al. (1997) go down to $\log_{10}(\Sigma[\mathrm{Mpc}^{-2}]) = 0.2$. The S0 population greatly outnumbers the elliptical population at low densities at this redshift (see Figure 3 in Dressler et al. (1997)). In contrast, the MORPHS data at $z \sim 0.5$ goes down to only $\log_{10} = 1.2$. However, at this density, the S0 fraction is lower than the elliptical fraction (see Figure 6 in Dressler et al. (1997)). It would require an unreasonable behavior at lower densities for the S0 to elliptical ratio at $z \sim 0.5$ to equal that at $z = 0$. Therefore, it is not the case that no evolution in the early-type fraction has occurred at low densities. We know that, at least since $z = 0.5$, the ratio of galaxies making up the early type fraction has changed. This is also the case at higher densities, but these changing ratios are balanced by a change in the spiral fraction. In fact, this decrease in the spiral fraction accompanying an increase in the S0 fraction is a strong argument for the hypothesis that late types transform into early types. It is strange that, at low densities, it is the S0 and early type fractions that balance to reach a constant fraction since $z = 1$. One possibility is that the transformation of late types to S0s is exactly balanced by late-type infall.

3.5 Summary

We have investigated the morphology-density relation in 10 high-redshift ($0.4 < z < 0.8$) clusters drawn from the ESO Distant Cluster Survey (EDisCS). We first examined the relation for each cluster individually, and found that there are not enough galaxies within the field of a given cluster to trace the morphology-density relation with high signal-to-noise. We therefore combined the galaxies from all 10 EDisCS clusters. We observed a sharp increase in the elliptical fraction at densities greater than $\log_{10}(\Sigma[\mathrm{Mpc}^{-2}]) \gtrsim 2$, showing that cluster ellipticals are already segregated by density at $z \sim 0.8$, or 7.5 Gyr ago. We isolated the high-redshift clusters to show that this trend is not driven entirely by the few clusters at $z < 0.6$.

We then compared the morphology-density relation observed in EDisCS clusters to those observed in the intermediate-redshift ($0.37 < z < 0.6$) MORPHS clusters and the low-redshift D80 clusters. We found that, although all three samples exhibit the trend of increasing elliptical fraction with density, both the slope and the amplitude of the EDisCS relations differ from those measured at lower redshift. These differences

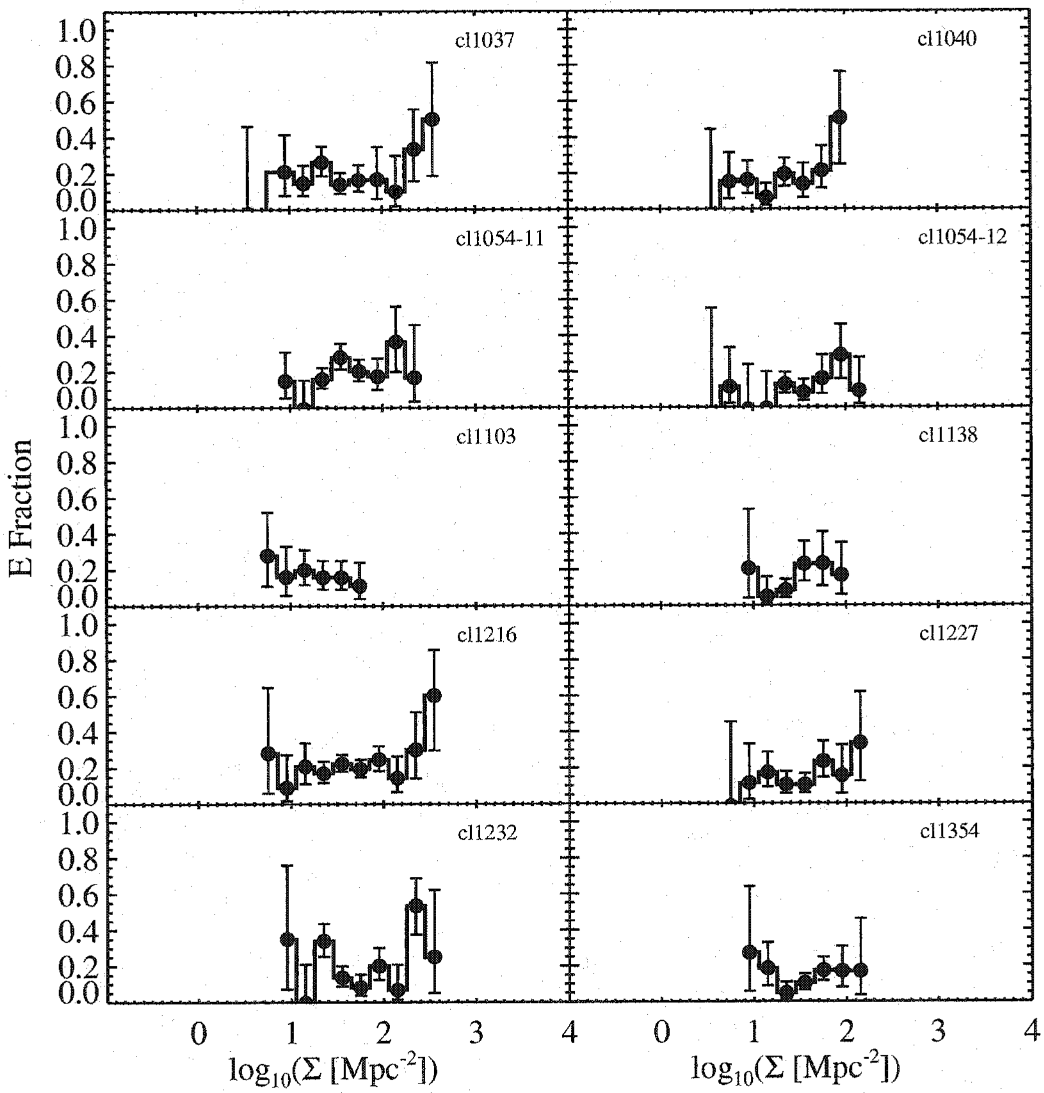

Figure 3.1 Morphology-Density Relation for Individual Clusters

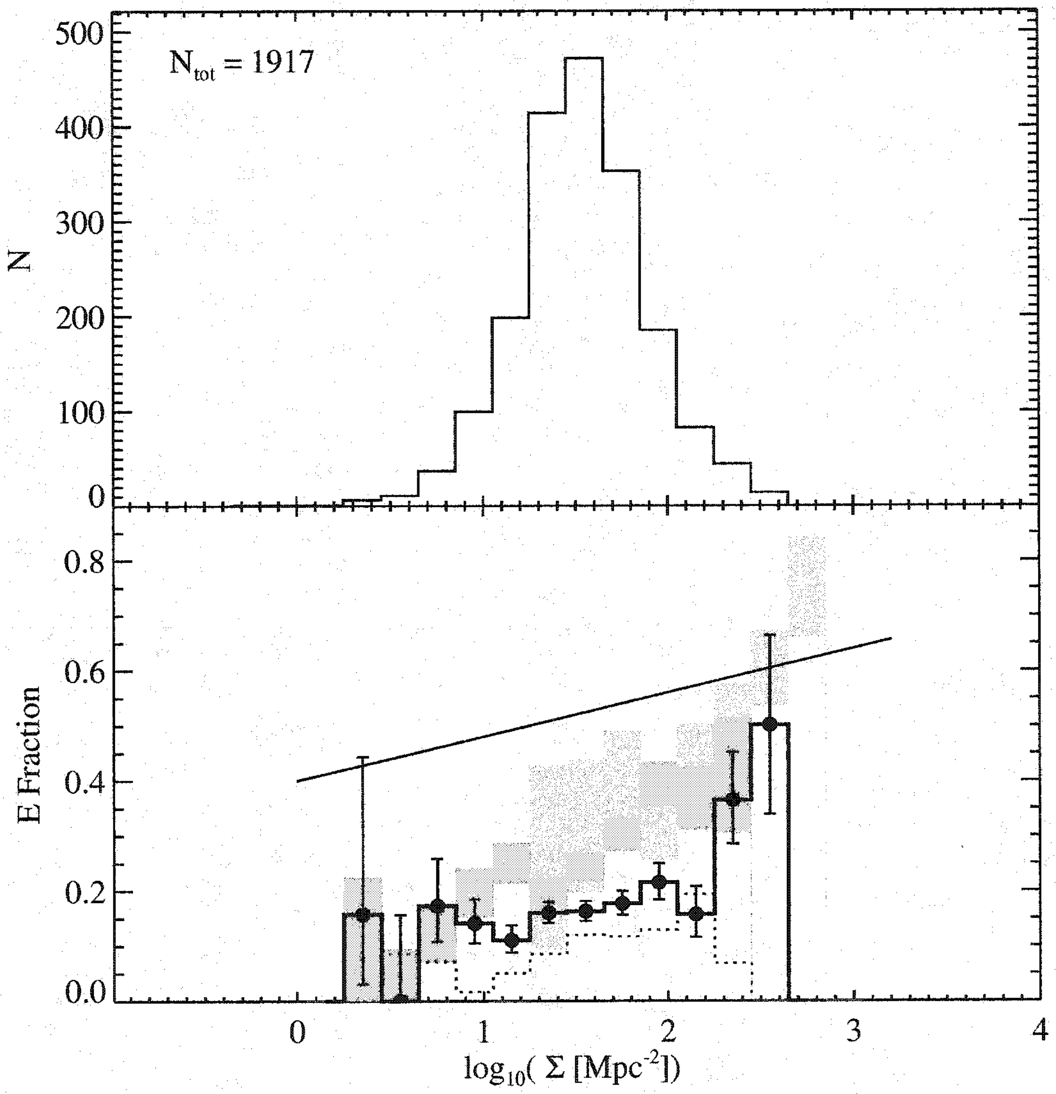

Figure 3.2 The T-Σ relation for 10 clusters with $0.4 < z < 0.8$. The top panel shows the number of galaxies in each bin. The bottom panel shows the fraction of E (solid line), and S0 galaxies (dotted line) as a function of local surface density. The lighter shading is the fraction of elliptical galaxies as a function of density for the concentrated clusters at $z \sim 0.5$ from Dressler et al. (1997). The darker shading is the elliptical fraction as a function of density for all of the clusters at $z \sim 0$ from Dressler et al. (1997). The solid line without error bars is the approximate E+S0 fraction as a function of density for galaxies at $z \sim 1$ (Smith et al., 2004).

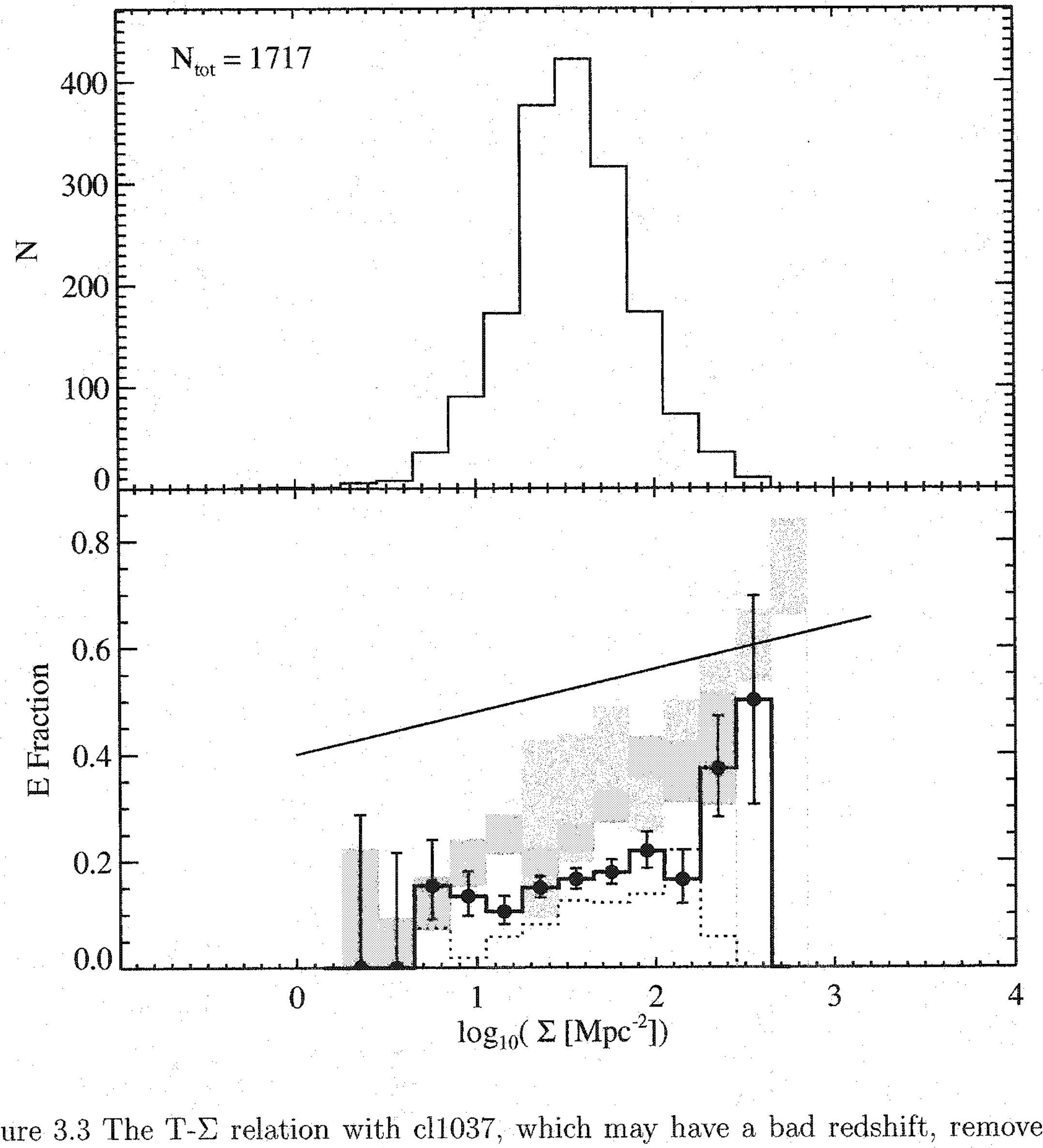

Figure 3.3 The T-Σ relation with cl1037, which may have a bad redshift, removed. The symbols are the same as in Figure 3.2.

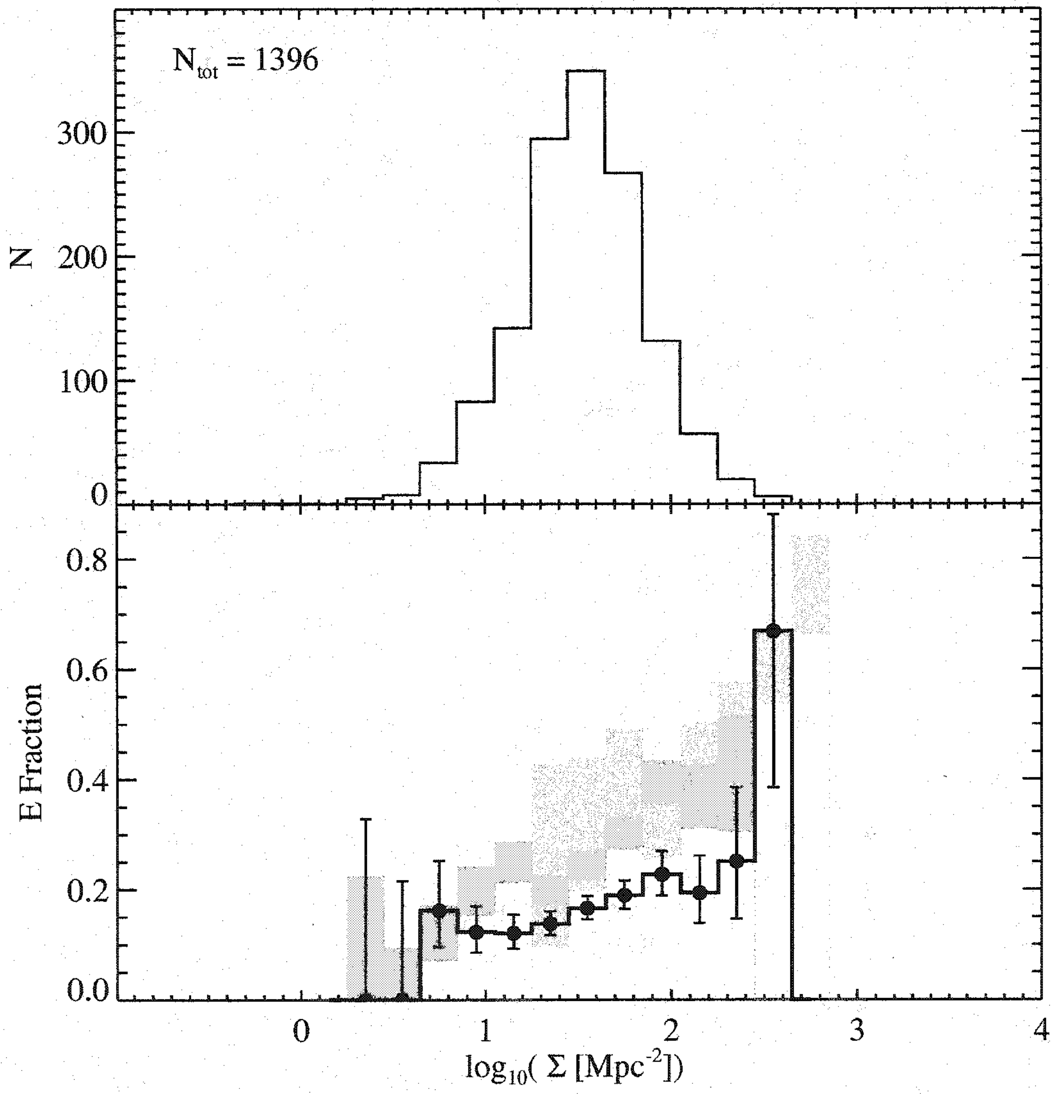

Figure 3.4 The T-Σ relation for the highest-redshift clusters: cl1227, cl1054-11, cl1103, cl1040, cl1054-12, cl1354, and cl1216 (see Figure 2.1 in Chapter 2). The symbols are the same as in Figure 3.2.

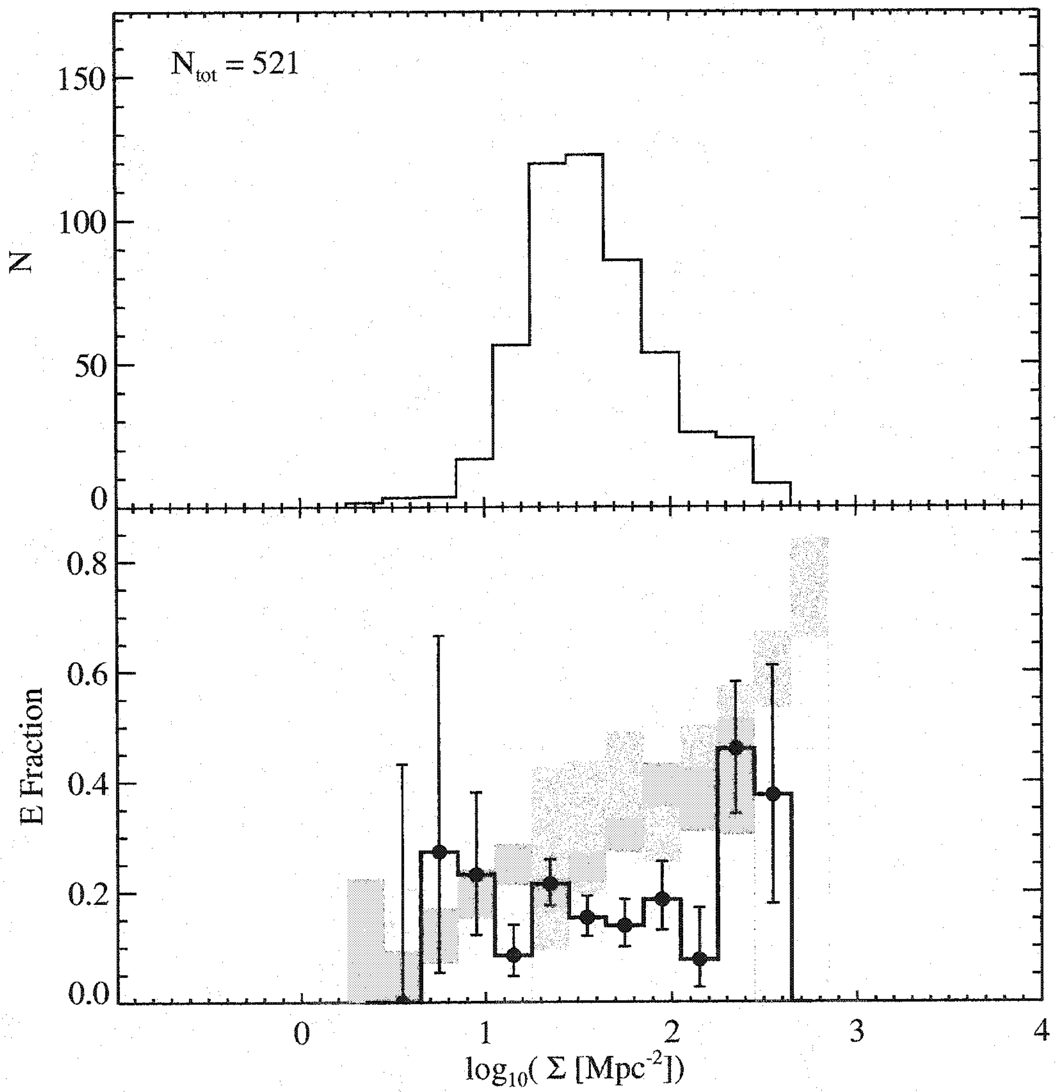

Figure 3.5 The T-Σ relation for the lowest-redshift clusters: cl1138, cl1232, and cl1037 (see Figure 2.1 in Chapter 2). The symbols are the same as in Figure 3.2.

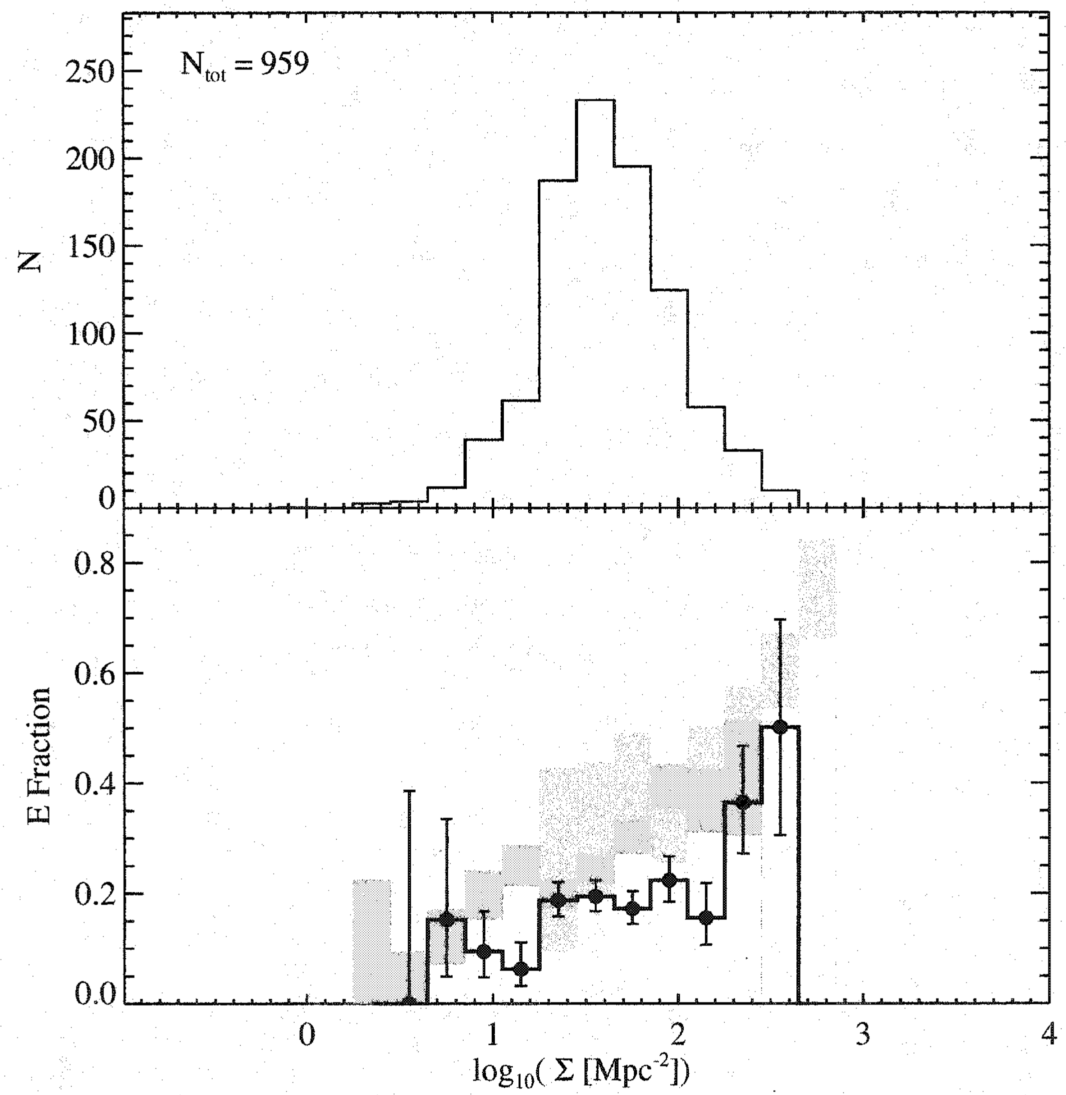

Figure 3.6 The T-Σ relation for those clusters with clean redshift histograms: cl1054-11, cl1054-12, cl1216, and cl1232. These also happen to be the four richest clusters, and the clusters with the highest velocity dispersions, as determined from weak lensing (see Figure 2.1 in Chapter 2). The symbols are the same as in Figure 3.2.

may be real, they may be due to systematic differences in galaxy classification, or they may result from differences in the global properties of the clusters analyzed. We are undertaking studies to try to eliminate the latter two possibilities.

We also compared our results to the only other available analysis of the morphology-density relation at high-redshift, carried out by Smith et al. (2004). We found that the morphology-density relation derived for the EDisCS clusters is inconsistent with their $z \sim 1$ sample. They measure early-type (E+S0) fractions which are much higher at all densities than those found in the EDisCS clusters. We suggest that this discrepancy is due either to the selection of different types of clusters in the two samples, or to systematic classification errors. We plan to investigate these possibilities in a future work.

Finally, taking the $z \sim 1$ morphology-density relation presented in Smith et al. (2004) at face value, we revisit their interpretation of the observed evolution in the morphology-density relation. They claim that there has been no evolution in the morphology-density relation at low densities ($\Sigma < 10$ Mpc^{-2}). We dispute this claim based upon an inspection of the E/S0 ratios in the lower-redshift comparison samples.

Chapter 4

A SEARCH FOR THE MERGING PROGENITORS OF LUMINOUS ELLIPTICAL GALAXIES IN NINE EDISCS CLUSTERS AT $0.4 < z < 0.8$

4.1 Abstract

When did elliptical galaxies form? The most straightforward interpretation of the observational data is that the stellar populations of ellipticals are old, with the bulk of stars having formed at $z \gtrsim 3$. In contrast, hierarchical models of structure formation predict that half of all ellipticals should be assembled through mergers at $z < 1$. A possible resolution to this discrepancy was recently proposed by van Dokkum et al. (1999), based upon their observation of a large number of major mergers involving luminous, red, bulge-dominated galaxies in the outskirts of the X-ray luminous cluster MS1054-03 at $z = 0.83$. Their findings, if typical, suggest that as many as 50% of the ellipticals found in present-day clusters were assembled in major mergers at $z < 1$, as expected in hierarchical models of structure formation. The red colors of the merging galaxies indicate that their stars are old, in keeping with the available observational constraints. If this high merger rate is typical, then the old stellar populations of ellipticals could be consistent with their late assembly. In this chapter, we use a sample of 9 clusters at $0.4 < z < 0.8$ to test whether mergers between red, bulge-dominated galaxies are typical in high-redshift clusters.

Our cluster sample is drawn from the ESO Distant Cluster Survey (EDisCS). Mergers were identified from high-resolution mosaics taken with the Advanced Camera for Surveys (ACS) aboard the Hubble Space Telescope (HST). Each mosaic covers

a $\sim 6.5' \times 6.5'$ region, allowing us to detect mergers within a large $\sim$7.5 Mpc^2 area around each cluster, similar to the area probed in the study of MS1054-03. All of the galaxies down to $I_{\rm auto} < 23$ were visually classified (see Chapter 2), and we searched for mergers among the E, S0, and Sa galaxies. We found 200 mergers in total (98 involving ellipticals, 19 involving S0s, and 83 involving Sas), over all fields. Using a combination of ground-based optical spectroscopy and photometric redshifts computed with ground-based optical and infrared imaging, we estimate that $\lesssim 97$ of these may be cluster members (64 involving ellipticals, 8 involving S0s, and 35 involving Sas). However, our photometric redshifts are calibrated to provide a complete, rather than pure, cluster sample. Therefore, a significant fraction of these potential cluster members are actually interlopers.

We find that the number of mergers varies substantially from cluster to cluster, highlighting the importance of a large cluster sample. If we assume that all of the potential mergers are cluster members, and estimate the number of elliptical cluster members using a statistical background correction, the number of mergers is comparable to the number of ellipticals, although the error bars in the latter quantity are quite large. This calculation overestimates the number of mergers and underestimates the number of cluster ellipticals. We conclude that the actual number of mergers is significantly less than the number of elliptical members. Therefore, the number of mergers in MS1054-03 is atypically large, and most cluster ellipticals were probably assembled at $z \gtrsim 3$.

4.2 Introduction

Most models for the formation of elliptical galaxies are based on either of two approaches. In the monolithic scenario, massive galaxies dissipationally collapse out of protogalactic gas clouds, and the bulk of stars form at high redshift, possibly regulated by galactic winds. The galaxy then evolves passively as an isolated system (e.g.

Larson, 1969; Tinsley, 1972; Larson, 1975; Arimoto & Yoshii, 1987; Matteucci & Tornambe, 1987; Bressan et al., 1994; Tantalo et al., 1996; Pipino & Matteucci, 2004). In hierarchical models, the luminous parts of galaxies reside in cold dark matter halos, which grow through mergers (White & Rees, 1978; White & Frenk, 1991; Lacey & Cole, 1993). Numerical simulations of merging galaxy pairs demonstrate that major mergers can result in remnants with structure similar to that of observed ellipticals (Toomre & Toomre, 1972; Barnes, 1988, 1989; Hernquist, 1992; Hernquist et al., 1993; Barnes & Hernquist, 1992). Semi-analytic models predict that a significant fraction of the stellar mass of ellipticals was formed in bursts of star formation accompanying major mergers at $z < 1$ (Kauffmann, 1996; Baugh et al., 1996; Cole et al., 2000). Recent simulations combined with semi-analytic models, however, push the major epoch of star formation to higher redshifts (Springel & Hernquist, 2003). These new results, if confirmed, eliminate one of the major differences between the monolithic collapse and the hierarchical growth models: the stars within massive elliptical galaxies may form at high redshifts in either model.

Elliptical galaxies follow several relations that have been used to constrain the ages of their stellar populations. These include the color-magnitude relation (Bower et al., 1992; Aragon-Salamanca et al., 1993; Ellis et al., 1997; Kodama & Arimoto, 1997; Stanford et al., 1998; Kodama et al., 1999; Terlevich et al., 2001; van Dokkum et al., 2000, 2001), the fundamental plane relation (van Dokkum & Franx, 1996; Kelson et al., 1997; Bender et al., 1998; van Dokkum et al., 1998; Jørgensen et al., 1999; van Dokkum & Stanford, 2003), the luminosity-radius relation (Barger et al., 1998; Ziegler et al., 1999; Schade et al., 1999), the $\mathrm{Mg_b}$-σ relation (Bender et al., 1996; Jørgensen, 1999; Colless et al., 1999), and the $\mathrm{M_{BH}} - \sigma$ relation (Gebhardt et al., 2000; Ferrarese, 2002). The tightness and/or evolution of these relations in rich clusters indicate that the bulk of the stellar mass in elliptical galaxies is old (for a review, see Peebles, 2002). However, there is some evidence that a small fraction of the stellar mass in field ellipticals is young (Jørgensen, 1999; Trager et al., 2000).

Although most of the stars in ellipticals are old, it is clear that some ellipticals are assembled through mergers (e.g. Schweizer, 2000). However, the fraction of elliptical galaxies assembled as a function of redshift is unknown. Galaxy clusters are an appealing place to look for the answer. Although they may represent an atypical environment for ellipticals, the high density of ellipticals in clusters is observationally convenient. Also, one can hope to track the evolution of a galaxy population by studying clusters at different redshifts (subject to the assumption that rich clusters at high redshift evolve into rich clusters at low redshift). van Dokkum et al. (1999) observed a large number of mergers between bright, red, bulge-dominated galaxies in the outskirts of the luminous X-ray cluster MS 1054-03 at $z = 0.83$. The fraction of observed mergers implies that 50% of ellipticals in present-day clusters assembled at $z < 1$, although their stars formed earlier. The authors posit that these merging galaxies are consistent with previous observations of a passively evolving population of elliptical galaxies because of the progenitor bias: the progenitors of today's youngest elliptical galaxies are not included in samples at high redshift. The progenitor bias allows us to have both hierarchical formation and old stellar populations. Unfortunately, these results are based on only one cluster.

In this work, we greatly increase the amount of high-resolution imaging data in the outskirts of high-redshift clusters. Specifically, we search for the merging progenitors of present-day ellipticals in the fields of 9 clusters at $0.4 < z < 0.8$ from the ESO Distant Cluster Survey (EDisCS). Each cluster has been imaged over a $6.5' \times 6.5'$ ($\lesssim 3$ Mpc × 3 Mpc) in F814W with the Advanced Camera for Surveys (ACS) aboard the Hubble Space Telescope (HST). The spheroidal mergers observed by van Dokkum et al. (1999) were found within an area of 2 × 3 Mpc. If the spatial distribution of mergers within MS1054-03 is typical, our data should cover a sufficient area to find their counterparts in the EDisCS clusters.

In §4.3, we briefly describe the EDisCS data. In §4.4, we describe our search for mergers. In §4.5 we isolate those candidate mergers that may be cluster members. In

§4.6 we estimate the fraction of merging progenitors of elliptical galaxies compared to the fraction of non-merging ellipticals. In §4.7, we discuss the possible end states of the merger candidates. In §4.8 we discuss the spatial distribution and color-magnitude diagrams of the merger candidates. Our results are summarized in §4.9.

4.3 Data

The ESO Distant Cluster Survey (EDisCS) sample consists of 19 optically-selected clusters between $0.4 < z < 0.8$ (White et al., in preparation). The data set accumulated for these clusters includes optical and infrared imaging as well as optical spectroscopy. Ten of the EDisCS clusters were imaged in F814W with the Advanced Camera for Surveys (ACS) aboard the Hubble Space Telescope (HST). Their positions and redshifts are provided in Chapter 2. The HST imaging data cover a $6.5' \times 6.5'$ region in 8 orbits under LOW SKY conditions in the field of each cluster. The ACS calibration pipeline, CALACS v4.3 (6-June-2003), debiased, dark-subtracted, flat-fielded, and flagged known bad pixels and saturated data. Shifts between images were calculated using cross-correlation. Combination of the images, including distortion-corrections and removal of cosmic rays, was accomplished using *MultiDrizzle*, a Python code written by Anton Koekemoer to run under PyRAF, the Python-based interface to IRAF. Further details on the reduction are available in Chapter 2.

All galaxies with $I_{\rm auto} < 23$ were visually classified. Here, $I_{\rm auto}$ is the SExtractor AUTO magnitude measured on the I-band VLT images. In addition, bulge+disk models were fit to all galaxies except for cl1227, which was the last cluster scheduled for HST observations. We therefore omit this cluster and will present an analysis of its merging galaxies in a future work.

Further details on the data acquisition, reduction, and visual classification can be found in Chapter 2. Information on the bulge+disk fits can be found in Simard et al. (in preparation).

4.4 Search for Mergers

To compare with previous results, we mimic the merger selection criteria of van Dokkum et al. (1999). Mergers in MS1054-03 were identified among elliptical (E), S0, and Sa galaxies displaying double nuclei, tidal tails, distorted doubles, or separations of $\lesssim 1''$ within a common envelope. Table 4.1 lists the numbers of E, S0, and Sa galaxies down to the classification limit ($I_{\rm auto} < 23$) in each EDisCS field. For each of the 1420 E, S0, and Sa galaxies, two classifiers (Professor Julianne J. Dalcanton and the author) examined $6'' \times 6''$ cutouts from the color VLT image, greyscale HST images at two stretches, and the residuals of the HST image once a smooth bulge+disk model was subtracted. The soft stretch of the HST image allowed us to identify structure near the galaxy core, such as double nuclei. The hard stretch aided in the identification of lower surface brightness disturbances in the outer regions of the galaxy. The residual image brings out low surface brightness tidal tails and common envelopes that may be swamped by the more regular features of the galaxy in the HST image. The color VLT image was not used to identify mergers, but provides a useful visual impression of the star formation rate of the merger candidates.

The process of selecting mergers is subjective, as is the visual classification of galaxies. We therefore classified mergers as either "definite" or "possible". Definite mergers displayed double nuclei, tidal tails, or clear signs of disturbance. Possible mergers were typically very close companions which did not show the above typical signs of interacting. Out of the 1420 galaxies inspected, 200 were identified as either definite or possible mergers. Images of the candidate mergers are provided in Figures 4.1 through 4.6. The images are sorted by type and by likelihood of being a merger. Within each category, images are ordered from bright to faint in $I_{\rm auto}$. Tables 4.2 though 4.4 provide basic information for each merger candidate. The last column indicates whether the merger is definite (1) or possible (0). Among ellipticals, 60 were definite, 38 were possible. Among S0 galaxies, 12 were definite, 7 were possible.

Table 4.1 Number of E, S0, and Sa galaxies in EDisCS fields

Cluster	Area arcmin^2	N$_\mathrm{E}$	N$_\mathrm{S0}$	N$_\mathrm{Sa}$	N$_\mathrm{tot}$
cl1037-1243	41.6968	73	37	73	183
cl1040-1155	42.2500	67	22	57	146
cl1054-1146	41.5099	74	21	77	172
cl1054-1245	37.2024	29	35	85	149
cl1103-1245	34.5816	46	17	13	76
cl1138-1133	39.2226	65	46	32	143
cl1216-1201	41.6104	136	64	72	272
cl1232-1250	41.6763	69	35	97	201
cl1354-1230	41.7689	33	25	20	78
total		592	302	526	1420

Among Sa galaxies, 53 were definite, 30 were possible.

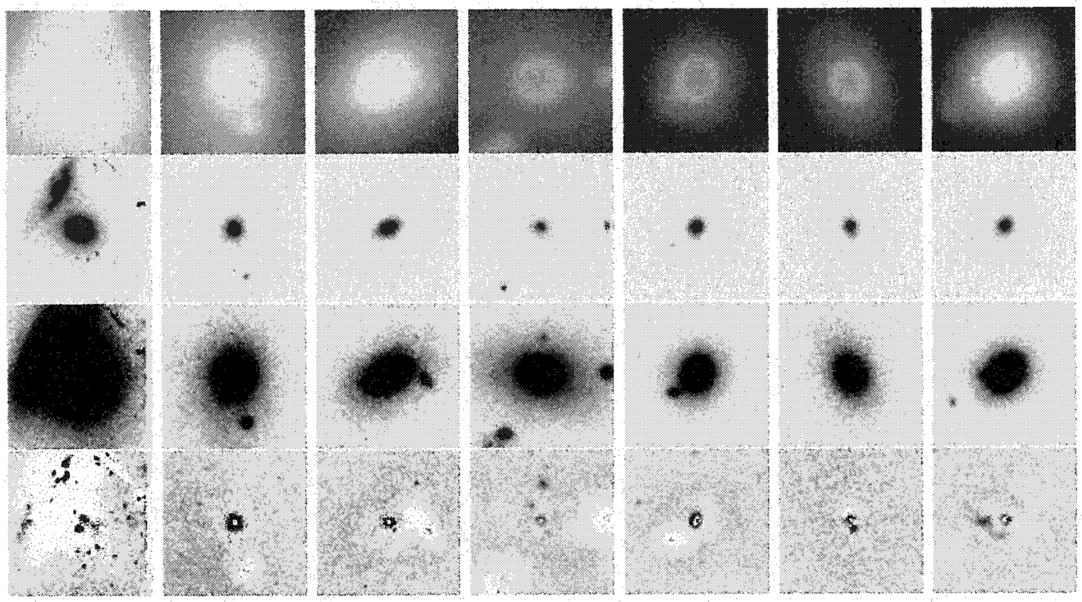

1103329-1244065 1037539-1241367 1138010-1135275 1232303-1250364 1232304-1251184 1232207-1252016 1037418-1244345

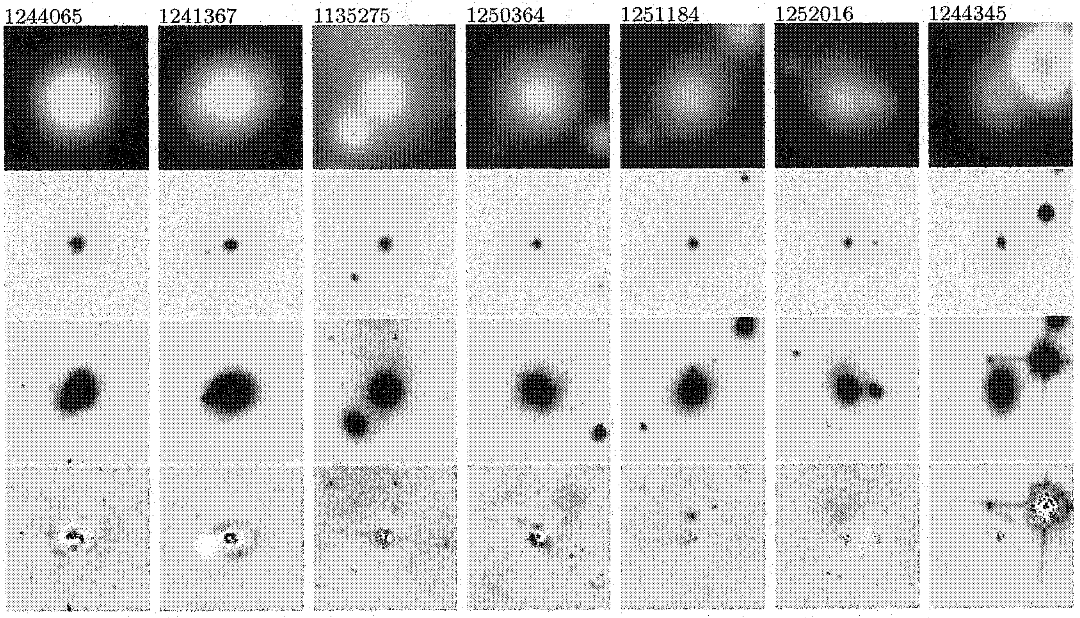

1054187-1144023 1103462-1243242 1037539-1241421 1040314-1153567 1054244-1146194 1054303-1149132 1232350-1250103

Figure 4.1 Definite Mergers Involving Ellipticals

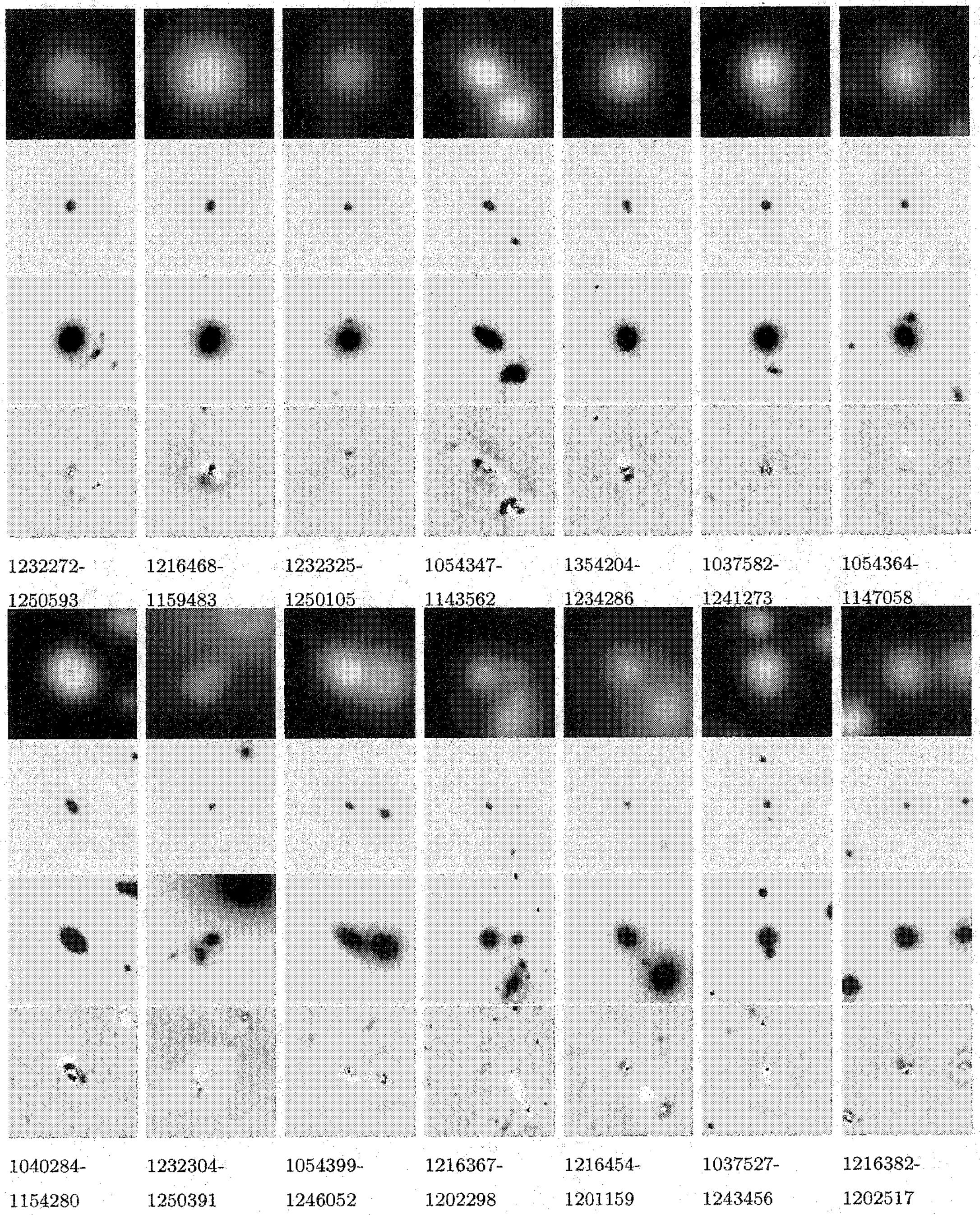

Figure 4.1 (continued)

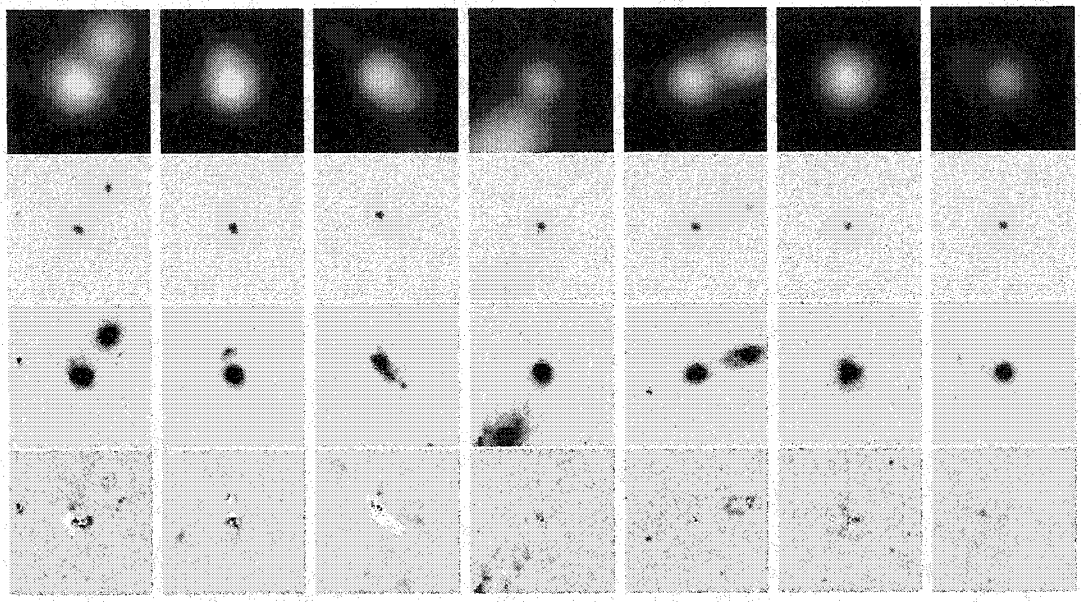

1216511-1158055 1216455-1159567 1138111-1132238 1232393-1253070 1354045-1234247 1037422-1247183 1232280-1250274

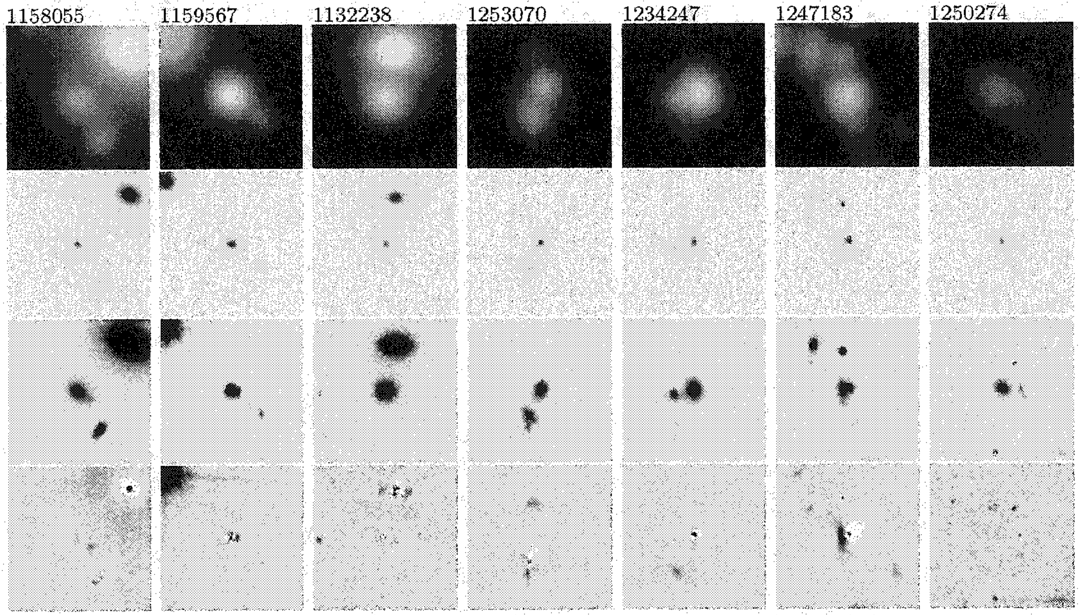

1216403-1202014 1054288-1145597 1037431-1246054 1054477-1245080 1216433-1200143 1040417-1155547 1232206-1252401

Figure 4.1 (continued)

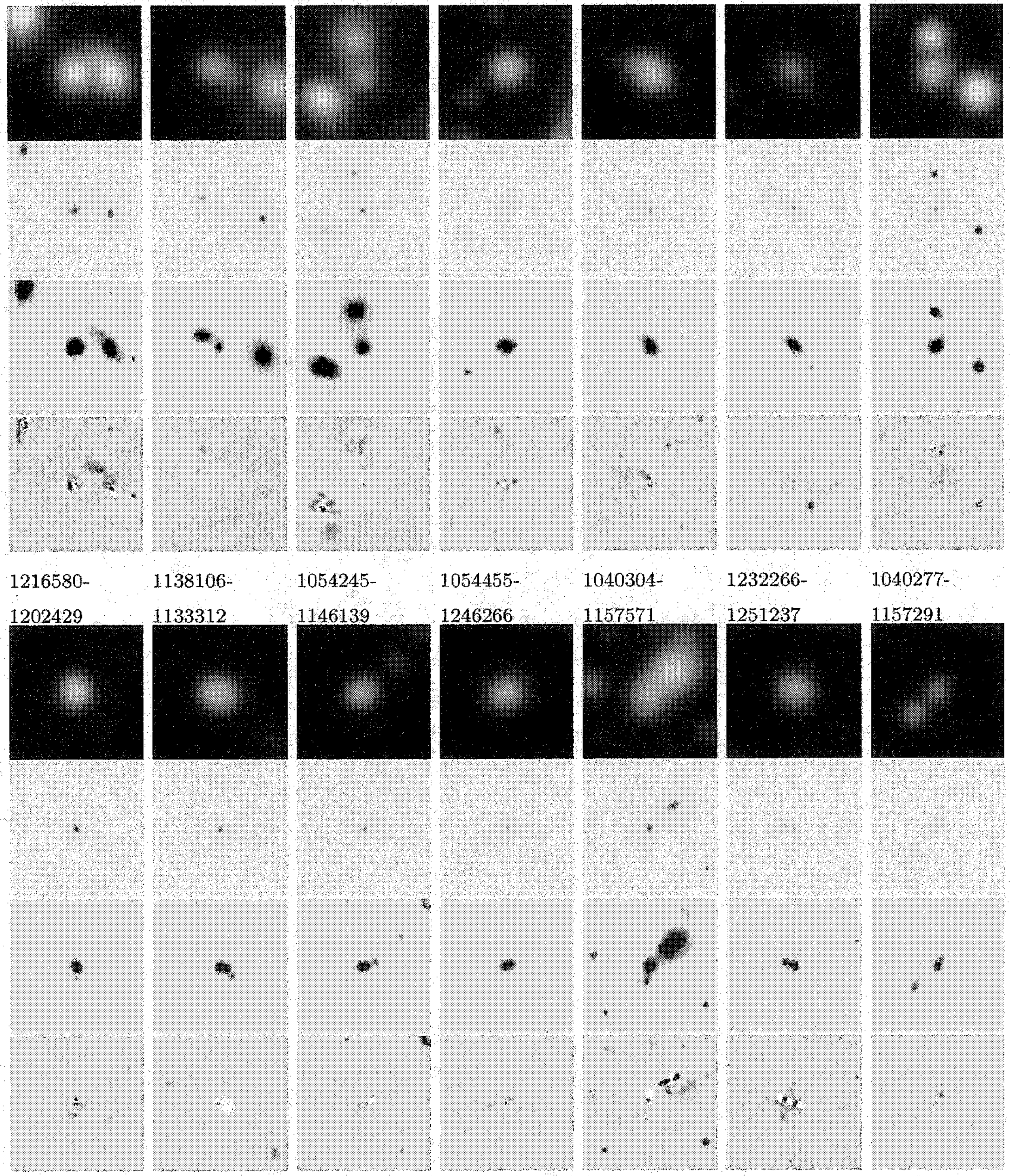

1216580-1202429 1138106-1133312 1054245-1146139 1054455-1246266 1040304-1157571 1232266-1251237 1040277-1157291

1037501-1243058 1040422-1154186 1232261-1249374 1040410-1155313 1232288-1249386 1138099-1135434 1216441-1202194

Figure 4.1 (continued)

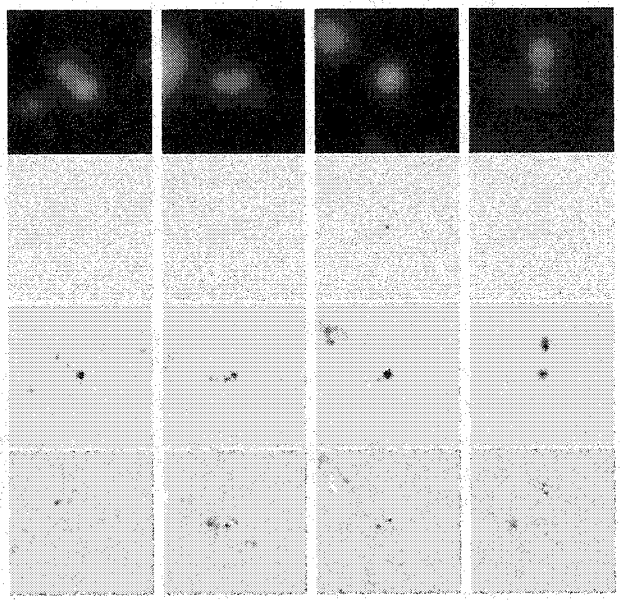

1216439-1200027

1216408-1202115

1138071-1132458

1054409-1245050

Figure 4.1 (continued)

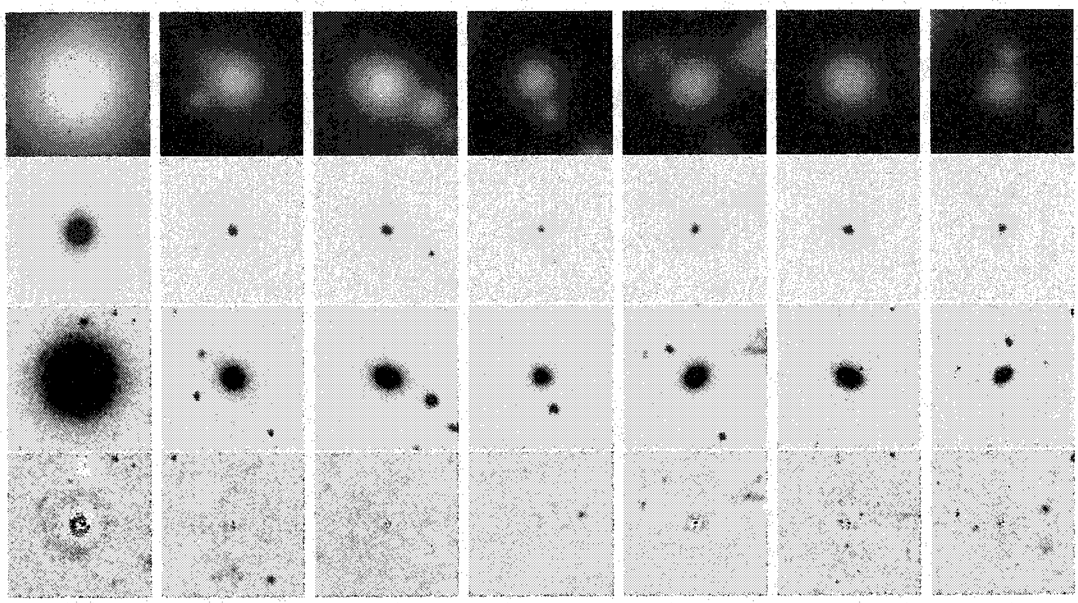

1232354-1248217 1354125-1233075 1354016-1230045 1216449-1201203 1232271-1250195 1232194-1252542 1232394-1248165

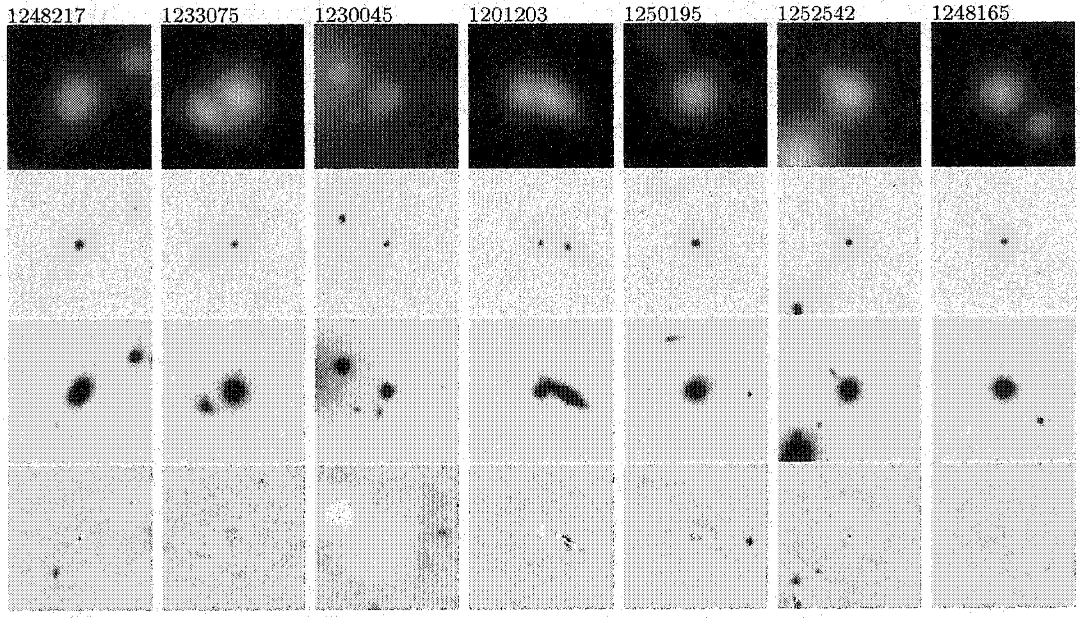

1232319-1250383 1054323-1147213 1232300-1250372 1216443-1201429 1232228-1251168 1054243-1146168 1232318-1249049

Figure 4.2 Possible Mergers Involving Ellipticals

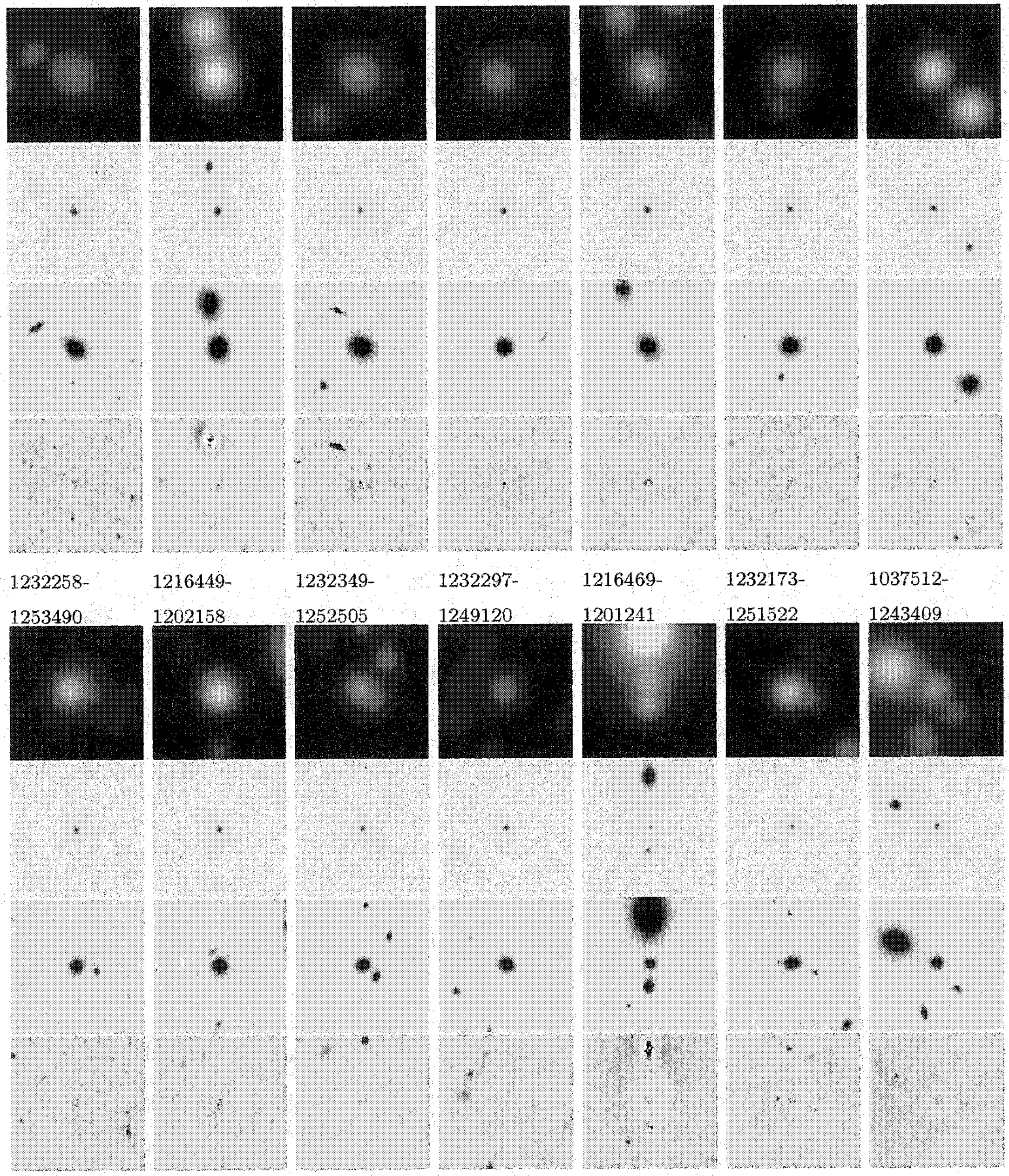

1232258-1253490
1216449-1202158
1232349-1252505
1232297-1249120
1216469-1201241
1232173-1251522
1037512-1243409

1054187-1144271
1037522-1246434
1216446-1201089
1232285-1250527
1216596-1200411
1038013-1242054
1354015-1230053

Figure 4.2 (continued)

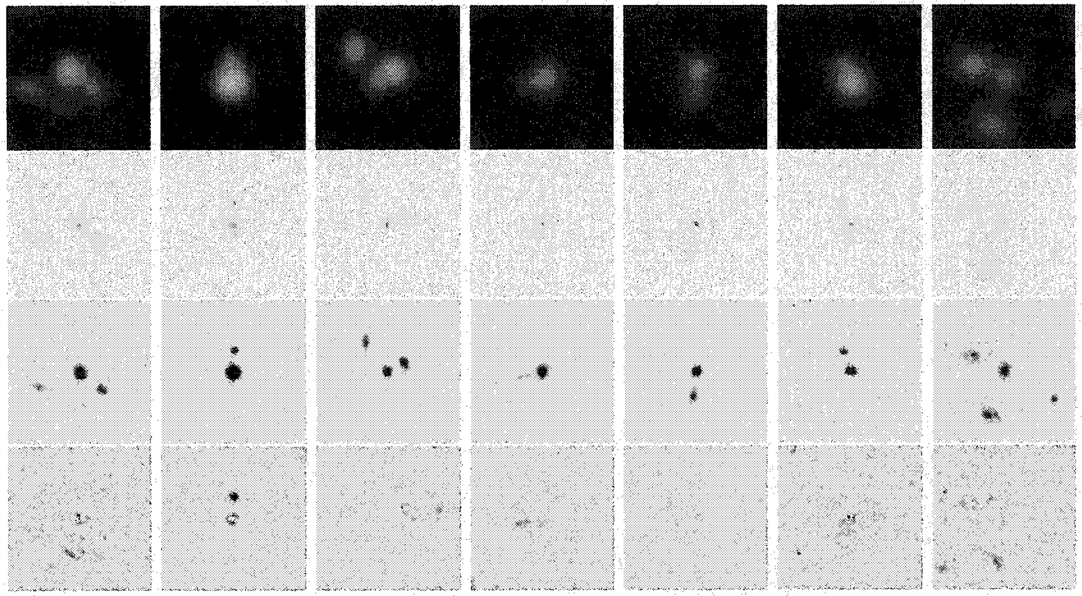

1037570-1246396 1040375-1155092 1216483-1201587 1216492-1202036 1054171-1147352 1138012-1137054 1040306-1152131

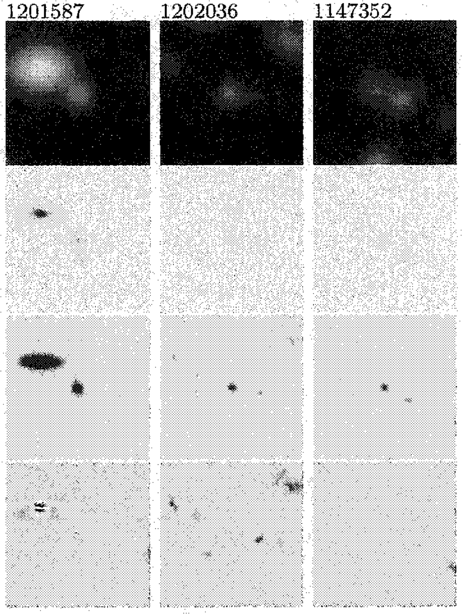

1216464-1159340 1138085-1133181 1054440-1246001

Figure 4.2 (continued)

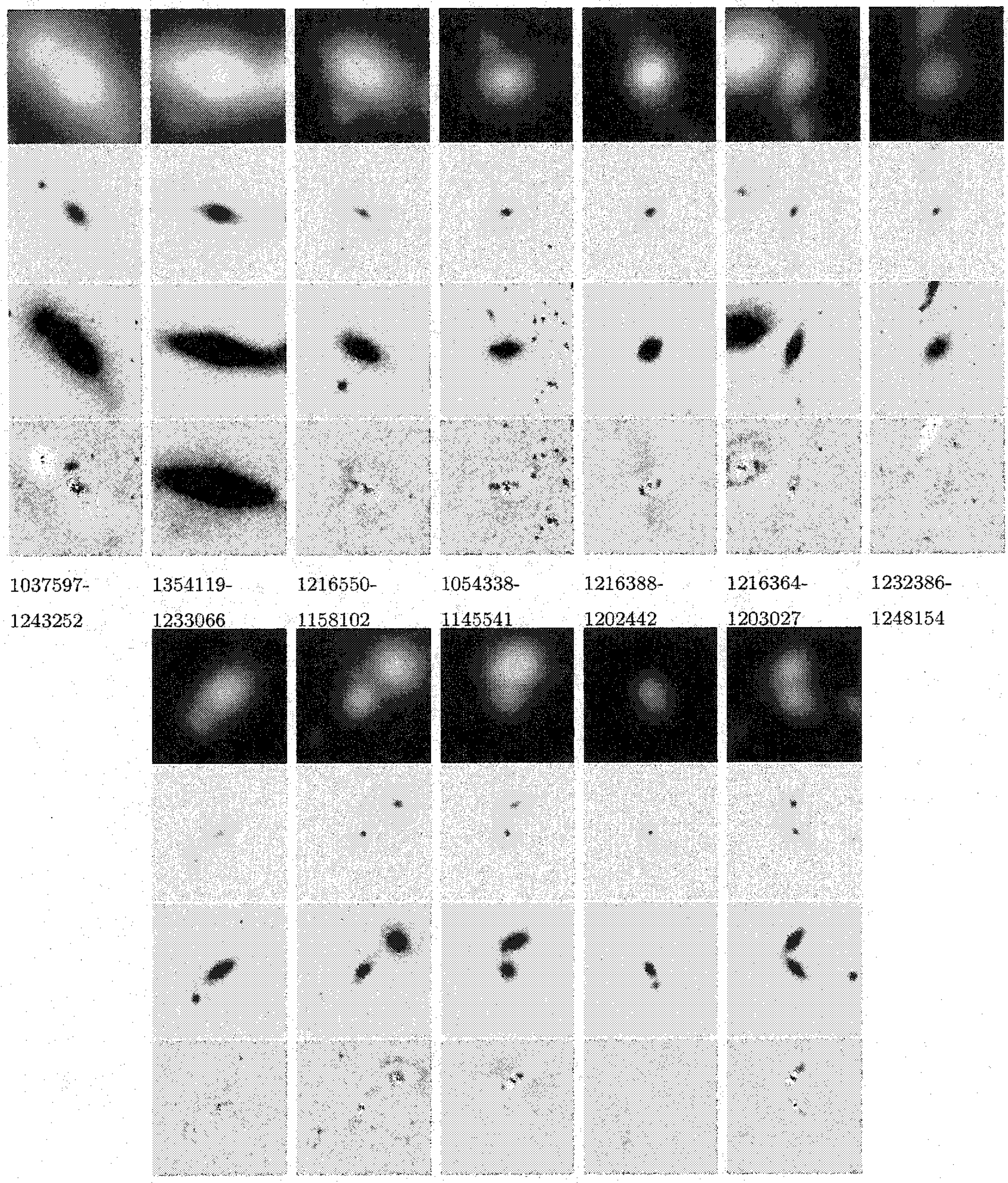

1037597-1243252
1354119-1233066
1216550-1158102
1054338-1145541
1216388-1202442
1216364-1203027
1232386-1248154

1138113-1132017
1216567-1159114
1232274-1251372
1354098-1231098
1354130-1230274

Figure 4.3 Definite Mergers Involving S0 Galaxies

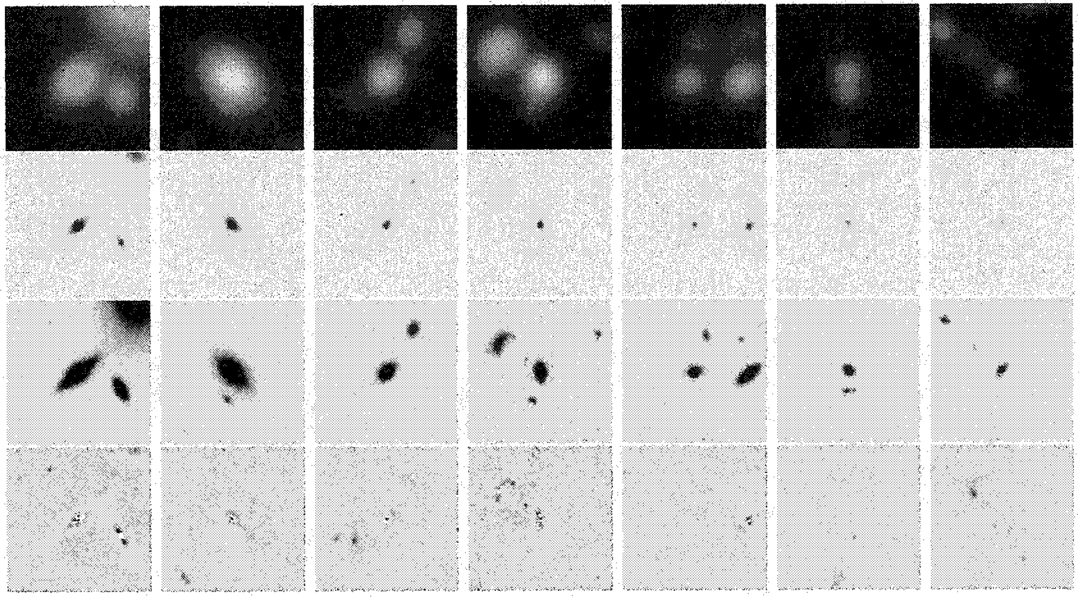

1232326-1249355 1054233-1147247 1054451-1247336 1138039-1136016 1354103-1231039 1054485-1246166 1216404-1202197

Figure 4.4 Possible Mergers Involving S0 Galaxies

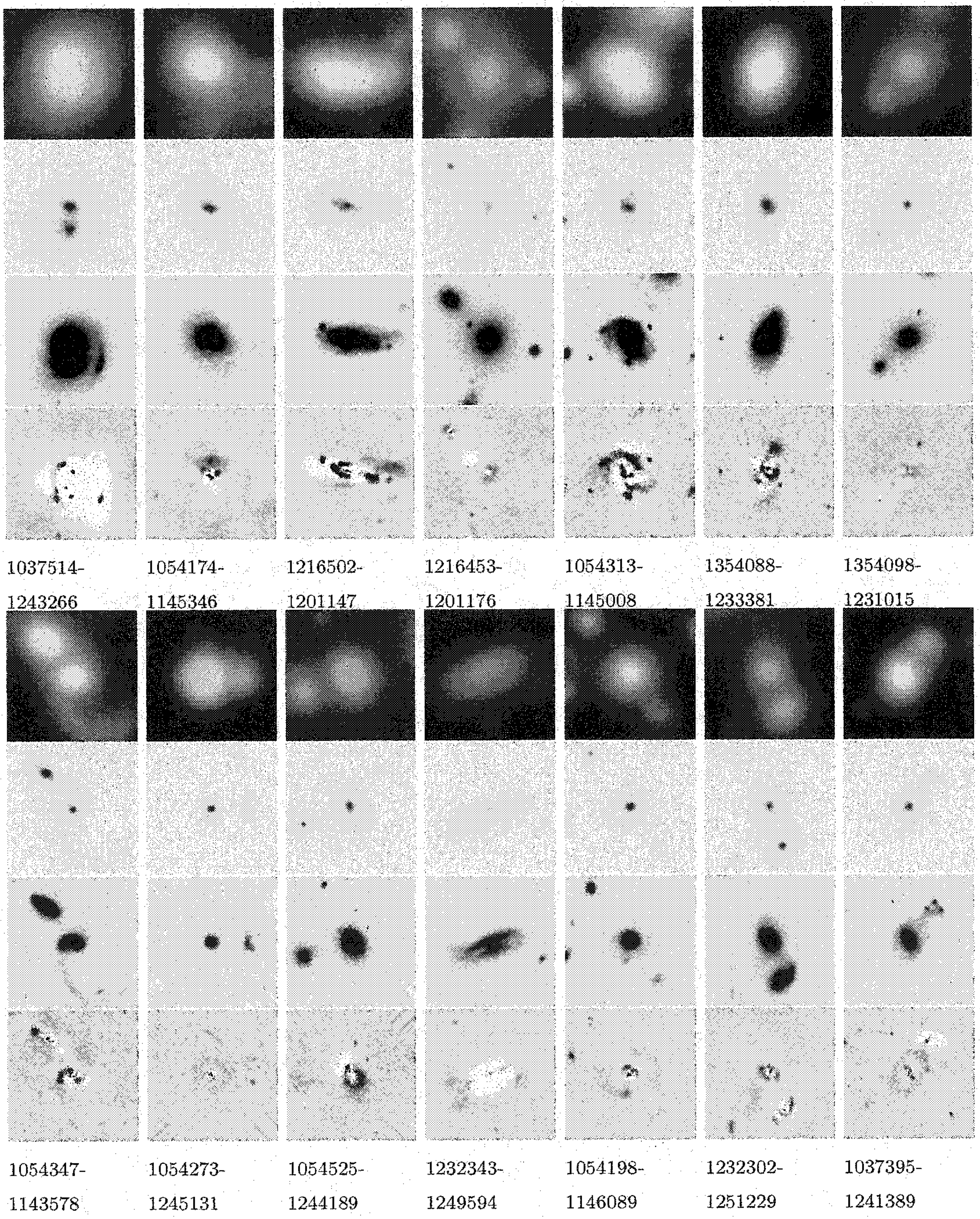

Figure 4.5 Definite Mergers Involving Sa Galaxies

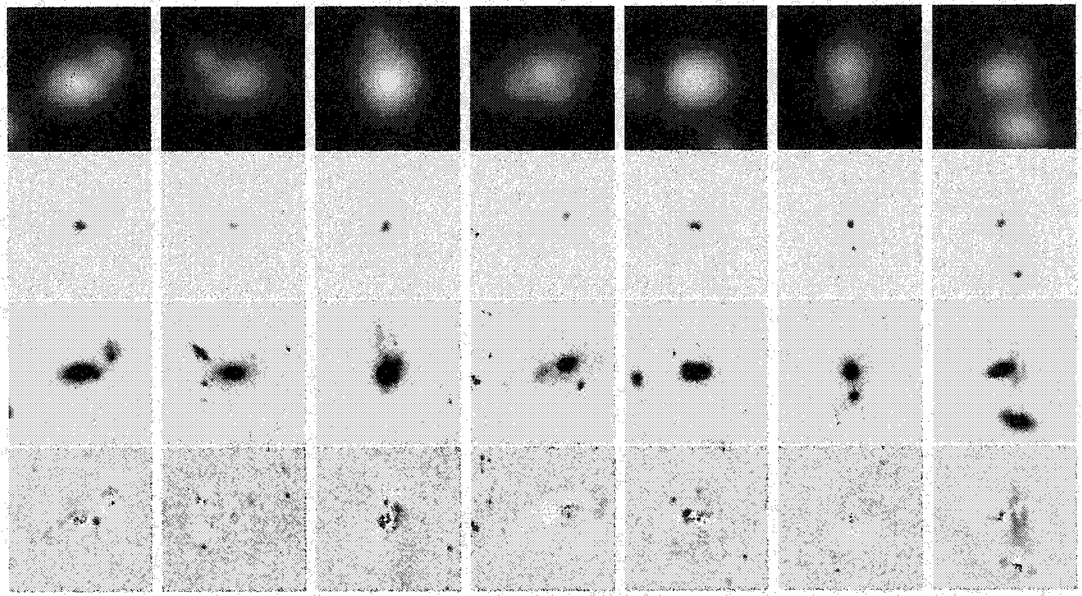

1054249-1147556

1354041-1234475

1054244-1150083

1038028-1241339

1232371-1249414

1354144-1228536

1054241-1146407

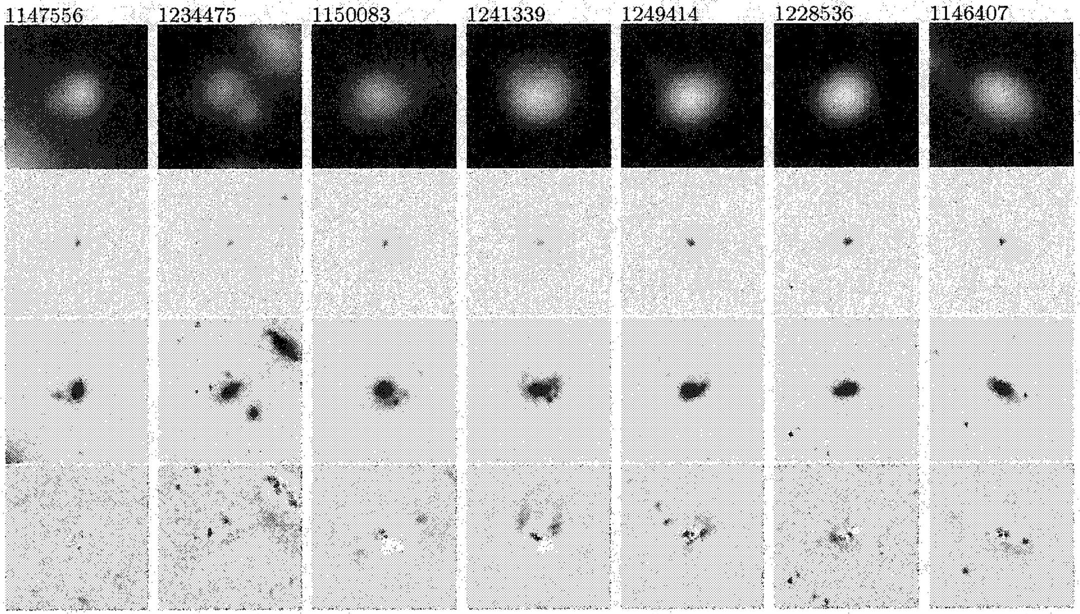

1037537-1241324

1216533-1201380

1054246-1146375

1040420-1156004

1138096-1135223

1232327-1254178

1040411-1156575

Figure 4.5 (continued)

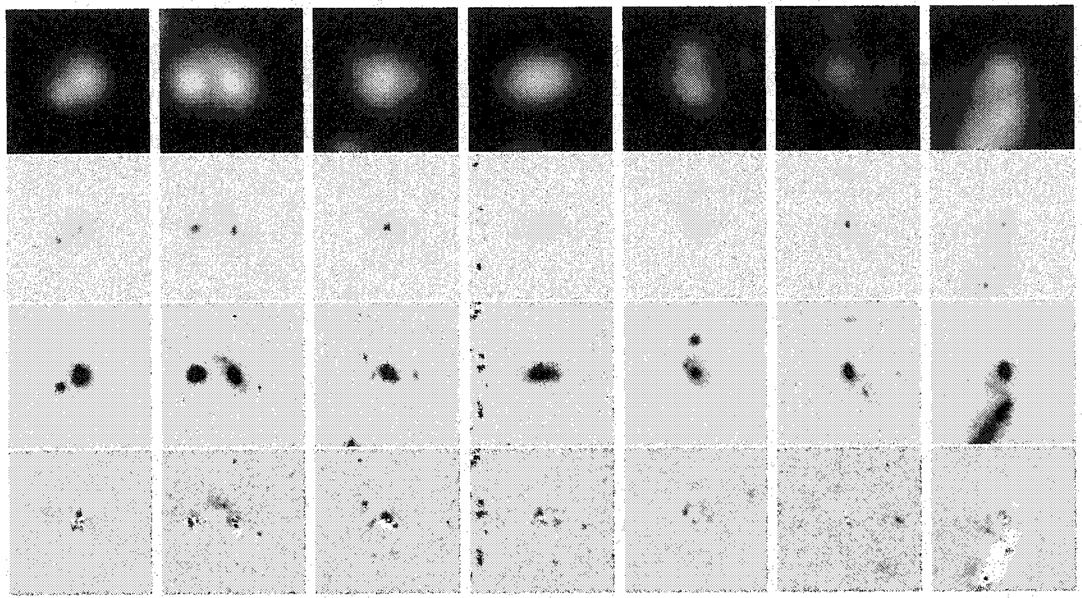

1037451-1245032 1216579-1202429 1216417-1157393 1040446-1152260 1054241-1145283 1232409-1252155 1037534-1243583

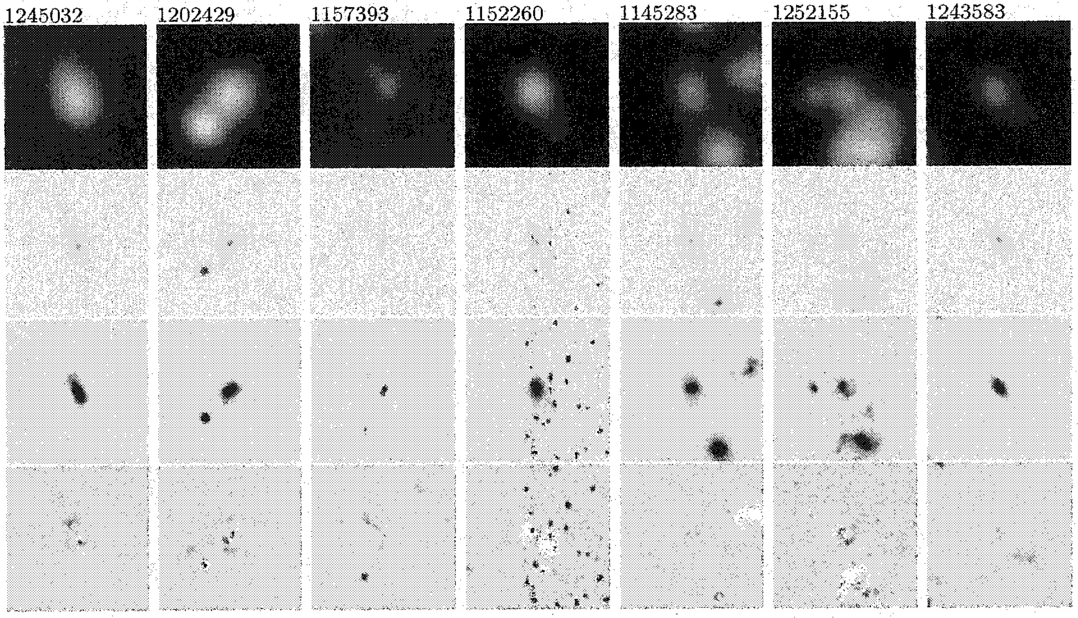

1054510-1245488 1054372-1246251 1054412-1245059 1037563-1241204 1216470-1201216 1040273-1157202 1232332-1251228

Figure 4.5 (continued)

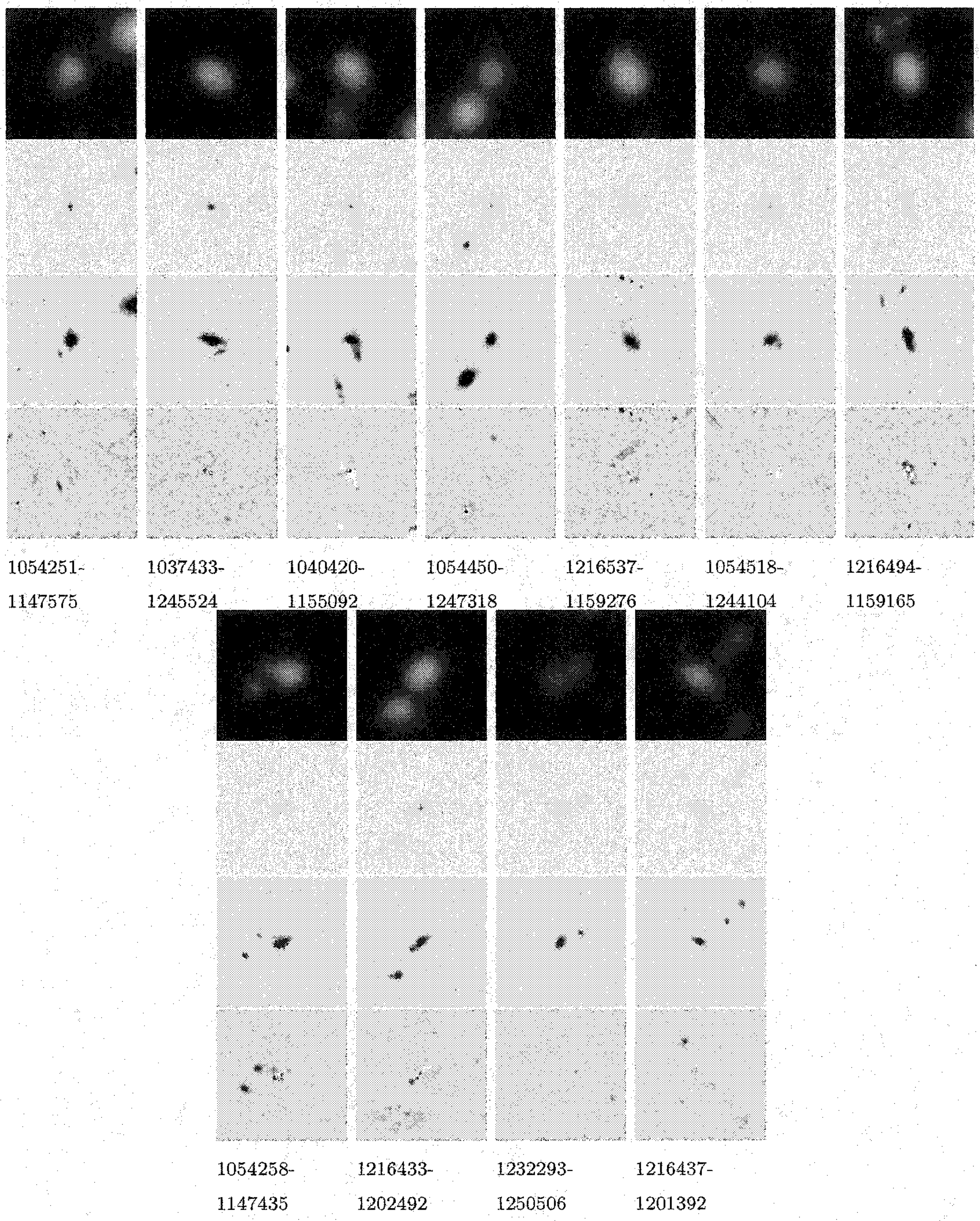

1054251-1147575 1037433-1245524 1040420-1155092 1054450-1247318 1216537-1159276 1054518-1244104 1216494-1159165

1054258-1147435 1216433-1202492 1232293-1250506 1216437-1201392

Figure 4.5 (continued)

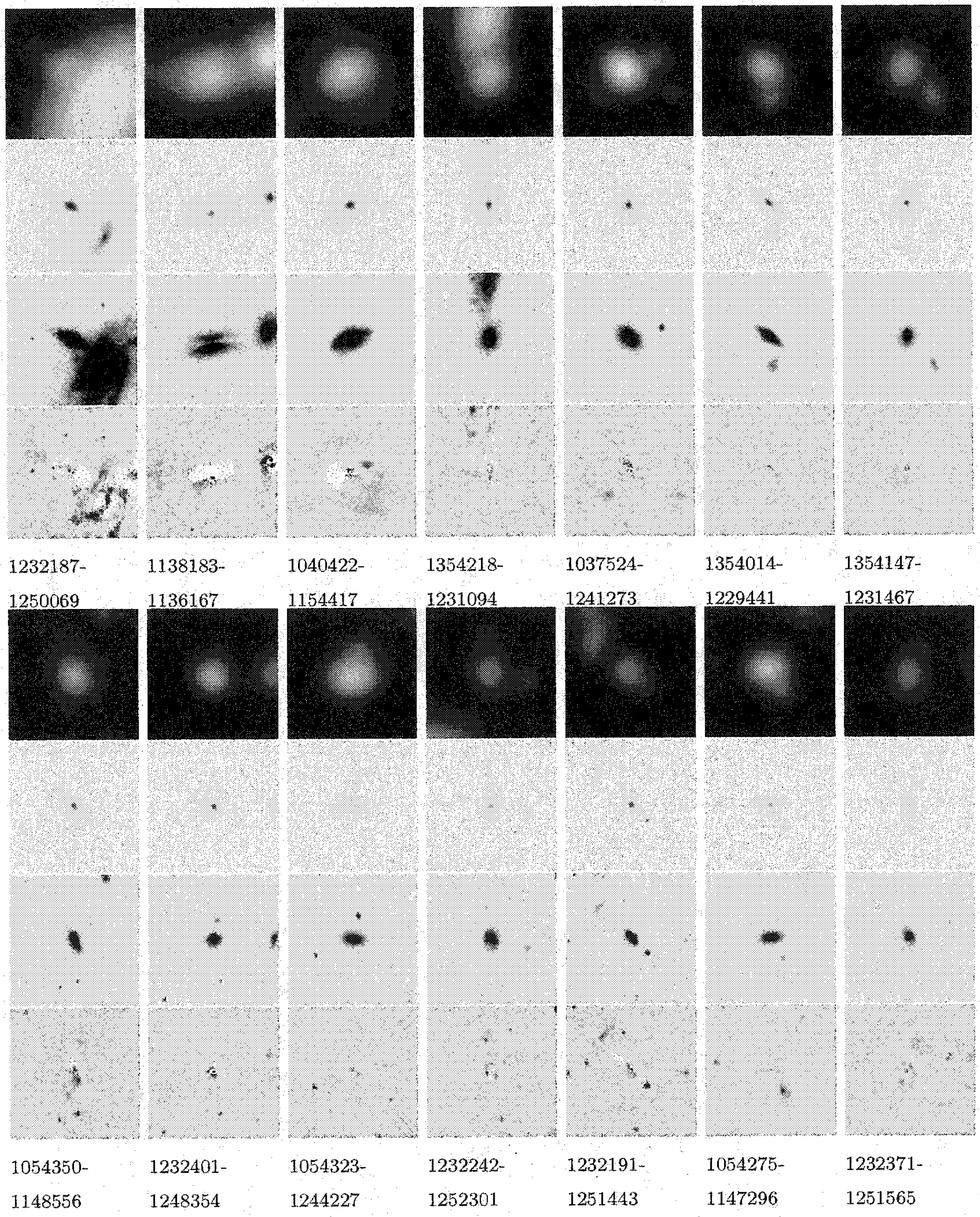

Figure 4.6 Possible Mergers Involving Sa Galaxies

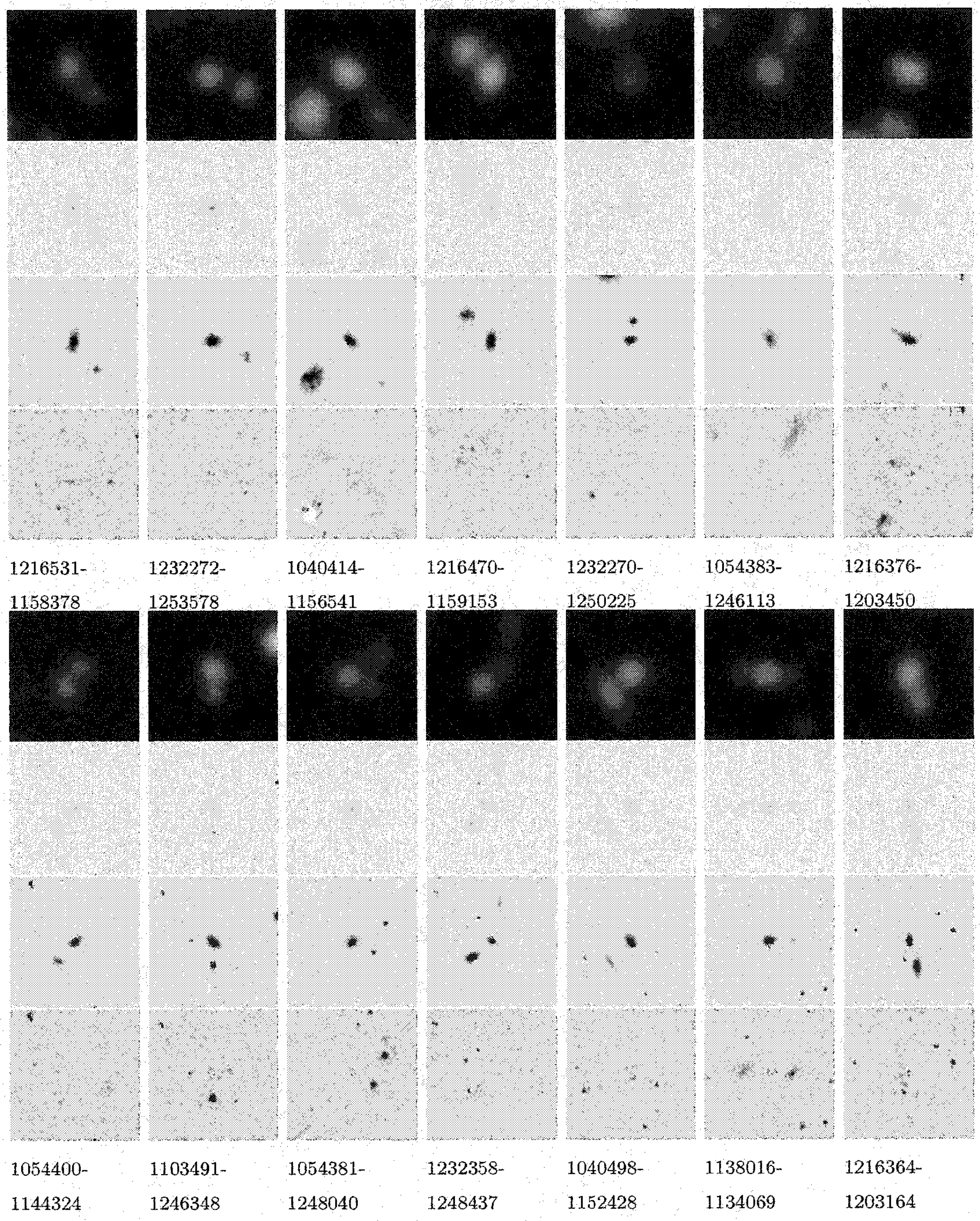

Figure 4.6 (continued)

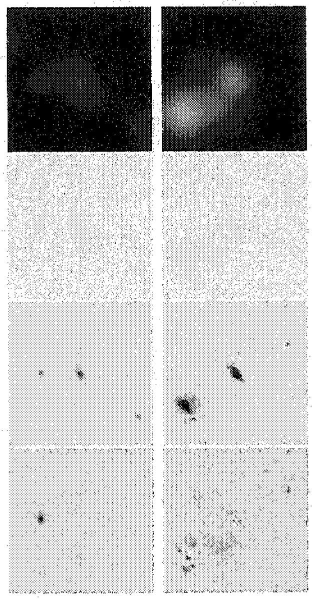

1232292-1249417 1037588-1245566

Figure 4.6 (continued)

4.5 Likely Membership of Identified Mergers

The merger candidates displayed in Figures 4.1 through 4.6 were selected without regard to their association with a cluster. However, we have two sources of information which bear on the likelihood of the mergers being cluster members. First, the EDisCS program includes an optical spectroscopic survey of each cluster field. At the time of writing, cl1040, cl1054-11, cl1054-12, cl1216, and cl1232 have available redshifts for ~100 galaxies each. Second, photometric redshifts have been computed using ground-based multicolor imaging taken at the Very Large Telescope (Pello et al., in preparation).

Tables 4.2 through 4.4 list the primary component of the merger, the secondary component of the merger, and their combined B band magnitudes and U-B colors. The VLT imaging, while of very high quality for ground-based data ($\lesssim 0.8''$ seeing), is still of much lower resolution than the ACS data. Therefore, some mergers which are resolved in the ACS images appear as one object in the VLT images. In these cases, Tables 4.2 through 4.4 list the secondary component as "N/A" and the magnitude and color refer to the single object detected in the VLT images. These tables also contain several flags which provide information about the likely membership of a merger candidate. The flag s_1 indicates whether the primary component is a spectroscopic member (1), a spectroscopic non-member (2), or was not spectroscopically targeted (9), while s_2 carries the same information for the secondary component. The flags p_1 and p_2 contain the analogous information based upon photometric redshifts. In the following plots, candidate mergers are considered cluster members if all identified components which were spectroscopically targeted are spectroscopic members. In the absence of spectroscopic information, photometric redshifts were used instead. Using this combination of spectroscopic and photometric redshifts, 54 of the E candidates, 8 of the S0 candidates, and 35 of the Sa candidates were designated as cluster members. Note that the photometric redshifts were calibrated to reject the maximum number of interlopers while rejecting no more than 10% of actual cluster members, independent of rest-frame color.

4.6 Estimate of Merger Fraction

Although we lack complete membership information for either the searched galaxies or the candidate mergers, and we do not know with certainty what fraction of mergers will evolve into elliptical galaxies, we can carry out a rough comparison between the number of non-merging cluster ellipticals and the number of merging elliptical progenitors.

Table 4.5 provides the number of merger candidates in each cluster as a function of morphology. Listed are both the raw counts, and the number after spectroscopic non-members are removed. Although the discussion of photometric redshifts in §4.5 indicates that many additional merger candidates are non-members, for this exercise

Table 4.2 Elliptical Merger Candidates

ID_1	ID_2	M_B^T	$(U\text{-}B)^T$	s_1	s_2	p_1	p_2	status
EDCSNJ1103329-1244065	NA	-25.879	-0.385	9	9	0	9	1
EDCSNJ1232354-1248217	NA	-24.337	-0.146	9	9	0	9	0
EDCSNJ1037539-1241367	NA	-22.670	0.235	9	9	1	9	1
EDCSNJ1138010-1135275	NA	-21.892	0.471	9	9	1	9	1
EDCSNJ1232303-1250364	NA	-21.929	0.475	1	9	1	9	1
EDCSNJ1232304-1251184	NA	-21.932	0.516	9	9	1	9	1
EDCSNJ1232207-1252016	NA	-22.859	0.436	1	9	0	9	1
EDCSNJ1037418-1244345	NA	-23.050	0.155	9	9	1	9	1
EDCSNJ1054187-1144023	NA	-23.420	-0.578	9	9	0	9	1
EDCSNJ1103462-1243242	NA	-23.185	-0.050	9	9	0	9	1
EDCSNJ1037539-1241421	EDCSNJ1037540-1241435	-22.708	0.187	9	9	1	1	1
EDCSNJ1040314-1153567	NA	-22.325	0.294	9	9	0	9	1
EDCSNJ1054244-1146194	NA	-22.111	0.506	1	9	1	9	1
EDCSNJ1054303-1149132	NA	-21.898	0.463	1	9	1	9	1
EDCSNJ1354125-1233075	NA	-22.257	0.349	9	9	1	9	0
EDCSNJ1232350-1250103	NA	-21.663	0.252	1	9	1	9	1
EDCSNJ1232272-1250593	NA	-22.039	0.224	9	9	1	9	1
EDCSNJ1216468-1159483	NA	-23.293	-0.520	9	9	1	9	1
EDCSNJ1354016-1230045	EDCSNJ1354015-1230053	-22.751	0.161	9	9	0	0	0
EDCSNJ1232325-1250105	NA	-21.810	0.399	9	9	1	9	1
EDCSNJ1054347-1143562	EDCSNJ1054347-1143578	-22.944	-0.121	9	9	0	1	1
EDCSNJ1354204-1234286	NA	-22.325	0.251	9	9	0	9	1
EDCSNJ1037582-1241273	NA	-21.998	0.266	9	9	1	9	1
EDCSNJ1054364-1147058	NA	-22.436	0.348	9	9	1	9	1
EDCSNJ1216449-1201203	NA	-21.870	0.477	1	9	1	9	0
EDCSNJ1232271-1250195	NA	-21.094	0.354	1	9	1	9	0
EDCSNJ1232194-1252542	NA	-21.109	0.425	9	9	0	9	0
EDCSNJ1040284-1154280	NA	-22.263	-0.561	9	9	1	9	1
EDCSNJ1232304-1250391	NA	-20.945	0.076	1	9	1	9	1
EDCSNJ1232394-1248165	NA	-20.483	0.431	9	9	1	9	0
EDCSNJ1232319-1250383	NA	-20.992	0.465	9	9	1	9	0
EDCSNJ1054323-1147213	NA	-22.195	-0.002	1	9	1	9	0
EDCSNJ1054399-1246052	EDCSNJ1054398-1246055	-23.182	-0.193	9	1	0	1	1
EDCSNJ1232300-1250372	NA	-20.440	0.409	9	9	1	9	0
EDCSNJ1216443-1201429	NA	-22.001	0.440	1	9	1	9	0
EDCSNJ1216367-1202298	NA	-21.974	0.408	9	9	1	9	1
EDCSNJ1216454-1201159	EDCSNJ1216453-1201176	-23.098	0.396	9	1	1	1	1
EDCSNJ1037527-1243456	NA	-21.111	0.393	9	9	1	9	1
EDCSNJ1216382-1202517	NA	-22.018	0.289	1	9	1	9	1

Table 4.2 (continued)

ID$_1$	ID$_2$	M_B^T	$(U-B)^T$	s_1	s_2	p_1	p_2	status
EDCSNJ1216511-1158055	NA	-22.226	-0.522	9	9	1	9	1
EDCSNJ1232228-1251168	EDCSNJ1232229-1251148	-21.274	0.325	1	9	1	0	0
EDCSNJ1054243-1146168	NA	-21.367	0.356	9	9	1	9	0
EDCSNJ1232318-1249049	EDCSNJ1232317-1249062	-21.312	0.086	1	9	1	0	0
EDCSNJ1232258-1253490	EDCSNJ1232259-1253481	-20.643	0.523	9	9	0	0	0
EDCSNJ1216455-1159567	NA	-22.452	-0.619	9	9	0	9	1
EDCSNJ1216449-1202158	EDCSNJ1216449-1202139	-22.928	-0.019	9	0	0	0	0
EDCSNJ1138111-1132238	NA	-20.324	-0.691	9	9	0	9	1
EDCSNJ1232393-1253070	EDCSNJ1232394-1253096	-21.752	-0.208	9	0	0	0	1
EDCSNJ1232349-1252505	NA	-20.540	0.357	9	9	1	9	0
EDCSNJ1232297-1249120	NA	-20.894	0.283	1	9	1	9	0
EDCSNJ1354045-1234247	EDCSNJ1354044-1234239	-22.492	-0.326	9	9	0	0	1
EDCSNJ1037422-1247183	NA	-21.221	-0.077	9	9	1	9	1
EDCSNJ1232280-1250274	NA	-20.809	0.300	9	9	1	9	1
EDCSNJ1216403-1202014	EDCSNJ1216403-1202029	-22.239	0.237	1	1	1	1	1
EDCSNJ1216469-1201241	EDCSNJ1216470-1201216	-22.186	0.452	9	9	1	1	0
EDCSNJ1054288-1145597	NA	-21.340	-0.639	9	9	0	9	1
EDCSNJ1037431-1246054	EDCSNJ1037430-1246036	-22.269	0.078	9	9	1	1	1
EDCSNJ1232173-1251522	NA	-20.635	0.294	9	9	1	9	0
EDCSNJ1054477-1245080	NA	-21.703	0.103	9	9	1	9	1
EDCSNJ1216433-1200143	NA	-21.957	-0.475	9	9	0	9	1
EDCSNJ1037512-1243409	EDCSNJ1037511-1243425	-21.355	0.321	9	9	1	1	0
EDCSNJ1040417-1155547	NA	-21.262	-0.488	9	9	1	9	1
EDCSNJ1232206-1252401	NA	-19.943	0.436	9	9	0	9	1
EDCSNJ1216580-1202429	EDCSNJ1216579-1202429	-22.532	-0.555	9	9	0	0	1
EDCSNJ1054187-1144271	NA	-21.329	-0.264	0	9	1	9	0
EDCSNJ1037522-1246434	NA	-20.589	-0.124	9	9	1	9	0
EDCSNJ1216446-1201089	NA	-21.258	0.342	1	9	1	9	0
EDCSNJ1138106-1133312	NA	-19.288	0.239	9	9	0	9	1
EDCSNJ1232285-1250527	EDCSNJ1232287-1250539	-20.255	0.271	9	9	1	0	0
EDCSNJ1216596-1200411	NA	-21.459	-0.353	9	9	1	9	0
EDCSNJ1038013-1242054	NA	-20.481	-0.117	9	9	1	9	0
EDCSNJ1054245-1146139	EDCSNJ1054246-1146124	-21.843	0.226	1	1	1	1	1
EDCSNJ1054455-1246266	NA	-20.803	-0.647	9	9	0	9	1
EDCSNJ1354015-1230053	EDCSNJ1354016-1230045	-22.751	0.161	9	9	0	0	0
EDCSNJ1040304-1157571	NA	-20.933	-0.654	9	9	0	9	1
EDCSNJ1037570-1246396	EDCSNJ1037572-1246400	-20.180	-0.288	9	9	0	0	0
EDCSNJ1232266-1251237	NA	-19.877	0.205	9	9	0	9	1

Table 4.2 (continued)

ID_1	ID_2	M_B^T	$(U-B)^T$	s_1	s_2	p_1	p_2	status
EDCSNJ1040277-1157291	EDCSNJ1040277-1157276	-21.522	-0.349	9	9	0	1	1
EDCSNJ1040375-1155092	NA	-20.733	-0.477	9	9	0	9	0
EDCSNJ1037501-1243058	NA	-20.293	-0.528	9	9	1	9	1
EDCSNJ1040422-1154186	NA	-20.743	-0.782	9	9	0	9	1
EDCSNJ1216483-1201587	NA	-20.933	-0.369	9	9	0	9	0
EDCSNJ1232261-1249374	NA	-19.868	-0.513	9	9	0	9	1
EDCSNJ1040410-1155313	NA	-20.485	-0.581	9	9	1	9	1
EDCSNJ1216492-1202036	NA	-20.810	0.120	9	9	1	9	0
EDCSNJ1054171-1147352	NA	-20.214	0.320	0	9	0	9	0
EDCSNJ1232288-1249386	EDCSNJ1232287-1249376	-22.031	-0.406	9	9	0	1	1
EDCSNJ1138012-1137054	NA	-19.052	-0.682	9	9	0	9	0
EDCSNJ1138099-1135434	NA	-19.223	-0.820	9	9	0	9	1
EDCSNJ1040306-1152131	EDCSNJ1040307-1152126	-20.823	0.030	9	9	1	1	0
EDCSNJ1216464-1159340	EDCSNJ1216465-1159330	-22.424	0.091	1	9	0	0	0
EDCSNJ1138085-1133181	NA	-18.192	0.126	9	9	0	9	0
EDCSNJ1216441-1202194	EDCSNJ1216441-1202204	-20.831	-0.373	9	9	1	0	1
EDCSNJ1054440-1246001	NA	-19.995	-0.341	0	9	0	9	0
EDCSNJ1216439-1200027	NA	-20.204	-0.712	9	9	0	9	1
EDCSNJ1216408-1202115	NA	-19.973	-0.602	9	9	0	9	1
EDCSNJ1138071-1132458	NA	-18.653	-0.733	9	9	0	9	1
EDCSNJ1054409-1245050	EDCSNJ1054409-1245039	-20.578	-0.410	9	9	1	0	1

Table 4.3 S0 Merger Candidates

ID_1	ID_2	M_B^T	$(U-B)^T$	s_1	s_2	p_1	p_2	status
EDCSNJ1037597-1243252	NA	-23.736	0.251	9	9	1	9	1
EDCSNJ1354119-1233066	EDCSNJ1354116-1233065	-24.257	-0.435	9	9	0	0	1
EDCSNJ1232326-1249355	EDCSNJ1232325-1249361	-22.008	0.244	0	9	1	0	0
EDCSNJ1216550-1158102	NA	-22.528	-0.528	0	9	0	9	1
EDCSNJ1054233-1147247	NA	-22.131	0.276	9	9	0	9	0
EDCSNJ1054338-1145541	NA	-21.688	0.410	9	9	1	9	1
EDCSNJ1216388-1202442	NA	-22.262	-0.288	0	9	1	9	1
EDCSNJ1216364-1203027	NA	-22.122	0.129	9	9	1	9	1
EDCSNJ1232386-1248154	EDCSNJ1232386-1248126	-21.022	0.402	9	9	1	0	1
EDCSNJ1138113-1132017	NA	-20.407	0.223	9	9	0	9	1
EDCSNJ1054451-1247336	EDCSNJ1054450-1247318	-21.964	0.425	1	9	0	0	0
EDCSNJ1138039-1136016	EDCSNJ1138040-1136005	-20.600	-0.334	9	9	0	0	0
EDCSNJ1216567-1159114	EDCSNJ1216566-1159101	-22.695	0.186	9	9	1	0	1
EDCSNJ1354103-1231039	NA	-20.774	0.312	9	9	1	9	0
EDCSNJ1232274-1251372	EDCSNJ1232274-1251361	-21.767	-0.496	0	9	1	1	1
EDCSNJ1354098-1231098	NA	-20.955	0.435	9	9	1	9	1
EDCSNJ1054485-1246166	NA	-20.791	0.060	9	9	1	9	0
EDCSNJ1354130-1230274	EDCSNJ1354130-1230263	-22.025	0.453	9	9	1	1	1
EDCSNJ1216404-1202197	NA	-20.040	0.031	9	9	1	9	0

Table 4.4 Sa Merger Candidates

ID$_1$	ID$_2$	M_B^T	$(U-B)^T$	s_1	s_2	p_1	p_2	status
EDCSNJ1037514-1243266	NA	-23.327	0.334	9	9	1	9	1
EDCSNJ1054174-1145346	NA	-23.366	0.061	0	9	0	9	1
EDCSNJ1216502-1201147	NA	-22.795	-0.453	9	9	0	9	1
EDCSNJ1216453-1201176	NA	-22.549	0.421	1	9	1	9	1
EDCSNJ1054313-1145008	NA	-22.522	-0.607	9	9	0	9	1
EDCSNJ1354088-1233381	NA	-23.404	-0.365	9	9	0	9	1
EDCSNJ1354098-1231015	NA	-22.140	0.401	9	9	1	9	1
EDCSNJ1054347-1143578	EDCSNJ1054347-1143562	-22.944	-0.121	9	9	1	0	1
EDCSNJ1054273-1245131	NA	-22.948	-0.669	9	9	0	9	1
EDCSNJ1054525-1244189	EDCSNJ1054527-1244196	-22.796	0.467	1	9	1	1	1
EDCSNJ1232343-1249594	NA	-21.790	0.106	0	9	1	9	1
EDCSNJ1054198-1146089	NA	-21.878	0.098	9	9	1	9	1
EDCSNJ1232187-1250069	EDCSNJ1232186-1250082	-23.768	-0.497	9	9	1	0	0
EDCSNJ1138183-1136167	EDCSNJ1138181-1136159	-21.135	0.210	9	9	0	0	0
EDCSNJ1040422-1154417	NA	-22.359	0.167	0	9	1	9	0
EDCSNJ1232302-1251229	EDCSNJ1232301-1251245	-21.880	0.224	9	0	1	0	1
EDCSNJ1037395-1241389	NA	-21.819	-0.217	9	9	1	9	1
EDCSNJ1054249-1147556	NA	-21.678	0.070	0	9	1	9	1
EDCSNJ1354041-1234475	NA	-22.474	0.383	9	9	1	9	1
EDCSNJ1054244-1150083	NA	-22.175	-0.391	9	9	0	9	1
EDCSNJ1038028-1241339	NA	-21.497	0.176	9	9	1	9	1
EDCSNJ1232371-1249414	NA	-21.230	-0.592	0	9	1	9	1
EDCSNJ1354144-1228536	NA	-22.364	0.371	9	9	1	9	1
EDCSNJ1354218-1231094	EDCSNJ1354218-1231068	-22.636	-0.341	9	9	1	0	0
EDCSNJ1054241-1146407	EDCSNJ1054241-1146427	-22.082	0.425	9	9	1	1	1
EDCSNJ1037537-1241324	NA	-20.671	-0.016	9	9	1	9	1
EDCSNJ1216533-1201380	NA	-21.573	0.410	9	9	1	9	1
EDCSNJ1037524-1241273	NA	-21.190	0.113	9	9	1	9	0
EDCSNJ1054246-1146375	NA	-21.631	-0.019	9	9	0	9	1
EDCSNJ1040420-1156004	NA	-21.732	-0.569	9	9	0	9	1
EDCSNJ1138096-1135223	NA	-20.518	-0.171	9	9	1	9	1
EDCSNJ1232327-1254178	NA	-20.978	-0.690	0	9	1	9	1
EDCSNJ1040411-1156575	NA	-21.152	-0.683	9	9	0	9	1
EDCSNJ1037451-1245032	NA	-20.959	-0.187	9	9	1	9	1
EDCSNJ1216579-1202429	EDCSNJ1216580-1202429	-22.532	-0.555	9	9	0	0	1
EDCSNJ1216417-1157393	NA	-21.837	-0.573	9	9	0	9	1
EDCSNJ1354014-1229441	NA	-21.614	0.011	9	9	1	9	0
EDCSNJ1354147-1231467	NA	-21.585	0.099	9	9	1	9	0

Table 4.4 (continued)

ID_1	ID_2	M_B^T	$(U-B)^T$	s_1	s_2	p_1	p_2	status
EDCSNJ1040446-1152260	NA	-21.104	-0.597	9	9	1	9	1
EDCSNJ1054241-1145283	NA	-20.625	-0.113	9	9	1	9	1
EDCSNJ1054350-1148556	NA	-21.081	0.268	9	9	1	9	0
EDCSNJ1232409-1252155	NA	-20.230	0.484	9	9	0	9	1
EDCSNJ1232401-1248354	NA	-20.455	0.006	0	9	1	9	0
EDCSNJ1037534-1243583	EDCSNJ1037535-1244006	-21.679	0.153	9	9	1	1	1
EDCSNJ1054323-1244227	NA	-21.431	-0.654	9	9	1	9	0
EDCSNJ1054510-1245488	NA	-21.429	-0.636	9	9	0	9	1
EDCSNJ1232242-1252301	NA	-20.309	0.124	1	9	1	9	0
EDCSNJ1054372-1246251	EDCSNJ1054372-1246262	-22.086	-0.692	9	9	0	0	1
EDCSNJ1054412-1245059	NA	-19.519	-0.426	9	9	0	9	1
EDCSNJ1037563-1241204	NA	-20.424	0.090	9	9	1	9	1
EDCSNJ1216470-1201216	EDCSNJ1216468-1201208	-21.703	0.006	9	9	1	1	1
EDCSNJ1040273-1157202	EDCSNJ1040272-1157222	-21.823	-0.530	9	9	1	0	1
EDCSNJ1232332-1251228	NA	-20.105	0.246	9	9	1	9	1
EDCSNJ1232191-1251443	EDCSNJ1232192-1251425	-20.343	-0.130	9	9	1	0	0
EDCSNJ1054251-1147575	NA	-20.576	0.249	0	9	1	9	1
EDCSNJ1037433-1245524	NA	-20.224	0.014	9	9	0	9	1
EDCSNJ1054275-1147296	NA	-20.886	-0.527	9	9	0	9	0
EDCSNJ1040420-1155092	NA	-20.660	-0.275	0	9	1	9	1
EDCSNJ1232371-1251565	NA	-20.138	-0.026	9	9	1	9	0
EDCSNJ1054450-1247318	EDCSNJ1054451-1247336	-21.964	0.425	9	1	0	0	1
EDCSNJ1216537-1159276	NA	-21.170	-0.573	0	9	0	9	1
EDCSNJ1216531-1158378	NA	-21.086	0.180	9	9	1	9	0
EDCSNJ1232272-1253578	EDCSNJ1232271-1253584	-20.250	-0.311	9	9	1	0	0
EDCSNJ1054518-1244104	NA	-20.749	0.273	9	9	1	9	1
EDCSNJ1040414-1156541	EDCSNJ1040415-1156559	-21.483	-0.430	9	1	0	1	0
EDCSNJ1216470-1159153	EDCSNJ1216471-1159142	-21.483	-0.536	9	9	0	0	0
EDCSNJ1232270-1250225	NA	-19.321	0.138	9	9	1	9	0
EDCSNJ1054383-1246113	EDCSNJ1054382-1246094	-20.842	-0.280	9	9	1	0	0
EDCSNJ1216494-1159165	NA	-20.974	-0.634	0	9	0	9	1
EDCSNJ1216376-1203450	NA	-20.616	-0.416	9	9	0	9	0
EDCSNJ1054400-1144324	NA	-20.289	-0.013	9	9	1	9	0
EDCSNJ1103491-1246348	NA	-20.160	-0.343	9	9	1	9	0
EDCSNJ1054381-1248040	NA	-20.511	0.030	0	9	1	9	0

Table 4.4 (continued)

ID_1	ID_2	$\mathrm{M}_\mathrm{B}^\mathrm{T}$	$(\mathrm{U-B})^\mathrm{T}$	s_1	s_2	p_1	p_2	status
EDCSNJ1232358-1248437	EDCSNJ1232358-1248416	-19.937	-0.297	9	9	0	0	0
EDCSNJ1054258-1147435	NA	-20.283	-0.649	9	9	0	9	1
EDCSNJ1040498-1152428	EDCSNJ1040499-1152437	-20.839	-0.582	9	9	1	0	0
EDCSNJ1216433-1202492	NA	-20.659	-0.630	9	9	0	9	1
EDCSNJ1232293-1250506	NA	-19.476	0.086	9	9	0	9	1
EDCSNJ1138016-1134069	NA	-18.878	-0.347	9	9	0	9	0
EDCSNJ1216364-1203164	EDCSNJ1216364-1203174	-21.403	-0.205	9	9	0	1	0
EDCSNJ1232292-1249417	NA	-19.114	0.193	9	9	1	9	0
EDCSNJ1037588-1245566	EDCSNJ1037589-1245578	-20.655	-0.436	9	9	1	1	0
EDCSNJ1216437-1201392	NA	-20.274	-0.450	9	9	1	9	1

we assume that all of the remaining candidates are cluster members, allowing us to calculate a conservative upper limit to the merger fraction.

Table 4.1 lists the number of ellipticals observed in the fields of each cluster, as well as the area of these fields. However, the number of ellipticals contains a substantial fraction of non-cluster-members. We subtract the field galaxies statistically as follows. From Postman et al. (1998), we estimate the surface density of field galaxies down to the magnitude limit of our visual classifications. The Medium Deep Survey (MDS) indicates that 10% of field galaxies down to $I = 22$ are ellipticals. We assume that this percentage can be extrapolated to $I_{\mathrm{auto}} = 23$. We then calculate the expected number of field galaxies and subtract it from those observed to calculate the number of expected cluster ellipticals.

The resulting number of expected ellipticals is given as the first number in column 6 of Table 4.5. Subtracted from this is the number of ellipticals involved in a merger. The result is the number of non-merging elliptical cluster members. Note that the accuracy of these values is very low. Because the HST mosaics cover a large area, a small error in the surface density of field galaxies will lead to a large inaccuracy in the number of expected field galaxies. The same holds true for small errors in the percentage of field galaxies that are ellipticals.

Comparing columns 5 and 6 of Table 4.5, we see that in most instances, given the very large errors, the number of mergers is comparable to the number of non-merging ellipticals, similar to the result seen in MS1054-03. If the same comparison were made with full spectroscopic membership information, the number of mergers would be lower and the number of ellipticals would be higher, for two reasons. First, many of the mergers that we have included in column 5 are not likely to be members, based upon photometric redshifts. Second, the overestimated number of mergers involving ellipticals has been subtracted from the total number of observed ellipticals in order to estimate the number of non-merging ellipticals. Thus, we have actually underestimated the number of non-merging ellipticals.

Therefore, we conclude that the number of mergers is significantly less than the number of non-merging ellipticals. The EDisCS clusters contain far fewer mergers than does MS1054-03. Because the likelihood of neighboring galaxies in a cluster to merge depends upon their relative velocities, the number of mergers in a cluster depends upon the cluster's dynamical state. It is therefore not surprising that the EDisCS clusters differ significantly from MS1054-03, since the dynamical states of clusters at high redshift are expected to vary substantially.

4.7 Likely Merger Products

The morphologies of the candidate merger remnants depend on two factors: the gas content and relative masses of the merging galaxies. Simulations show that if the gas content is very low, then the result will be a spheroidal galaxy (Toomre & Toomre, 1972; Barnes, 1992). If the gas content is high, but the merging galaxies are of roughly equal mass, the result will still be spheroidal. On the other hand, mergers involving large amounts of gas and very disparate masses may result in a disk galaxy. These would appear in our color VLT images as large blue objects merging with small blue or red objects. Among the mergers that are likely cluster members,

Table 4.5 Non-Merging Ellipticals Versus Merging Progenitors of Ellipticals

Cluster	$N_{E,mergers}$	$N_{S0,mergers}$	$N_{Sa,mergers}$	$N_{tot,mergers}$	$N_{E,members}$	f
cl1037-1243	12	1	10	23	31.2-12=19.2	1.20
cl1040-1155	9	0	8-2 =6	15	24.7-9=15.7	0.95
cl1054-1146	11-2=9	2	14-3 =11	22	32.4-9=23.4	0.94
cl1054-1245	5-1=4	2	10-1=9	15	0	
cl1103-1245	2	0	1	3	11.3-2=9.3	0.32
cl1138-1133	7	2	3	12	25.7-7=18.7	0.64
cl1216-1201	21-1=20	5-2 =3	14-2 =12	35	94.3-20=74.3	0.47
cl1232-1250	26-1=25	3-2 =1	16-5 =11	37	27.2-25=2.2	16.8
cl1354-1230	5	4	7	16	0	

we do not see many objects of this description, but EDCSNJ1037395-1241389 and EDCSNJ1037588-1245566 are examples of mergers that are the most unlikely to form ellipticals.

We have estimates of the [OII] λ3727 equivalent width for the 20 mergers that have at least one member targeted for spectroscopy. Of these, only 6 had any measurable [OII] emission, with equivalent widths of -0.8 (EDCSNJ1054303-1149132), -3.5 (EDCSNJ1216382-1202517), -3.6 (EDCSNJ1232271-1250195), -7.6 (EDCSNJ1054323-1147213), -13.6 (EDCSNJ1054246-1146124, a secondary), and -16.9 (EDCSNJ1232304-1250391). Therefore, most of the spectroscopic sample is gas-free.

4.8 Discussion

In Figure 4.7 we plot the spatial distribution of those mergers not rejected as likely non-members. Green dots are merger candidates without spectra, but which have been assigned cluster membership based upon their photometric redshifts. Red dots are spectroscopically confirmed merger candidates. Those merger candidates surrounded by a thin circle are "possible" mergers, while those surrounded by a heavy circle are "definite" mergers. The number of mergers varies substantially from cluster to cluster. Clusters cl1037, cl1054-11, cl1216, and cl1232 contain many more merger candidates than the remaining clusters. The large number of candidates in cl1054-11, cl1216, and cl1232 is likely due to the fact that these are the three richest clusters in our sample. However, cl1037 is the poorest cluster. It is also has a very elongated, filamentary structure, indicating that it is not dynamically evolved. Perhaps this cluster is composed of cold groups within which relative galaxy velocities are small.

In general, the merger candidates can be found both in the cluster center and in the cluster outskirts. The presence of a large number of mergers in the cluster center, such as those found in cl1232, is surprising. The relative velocities in such an environment should be too high for mergers to be common. Because most of these centrally-located merger candidates have been assigned cluster membership based upon photometric redshifts, it will be interesting to see whether spectroscopic followup confirms membership.

Figures 4.8 through 4.10 show the rest-frame U-B versus B color-magnitude diagrams of the merger candidates in each cluster. The merger candidates are indicated with the same symbols used to plot their spatial distribution in Figure 4.7. In addition, spectroscopically-confirmed elliptical galaxies are plotted as red points and ellipticals lacking spectra but which may be cluster members based upon their photometric redshifts are plotted as black points. There are several features of note in these plots. First, a fair number of the merger candidates lie blueward of the red sequence, as found for the mergers in MS1054-03. Second, there is often a merger candidate at the tip of the elliptical sequence, indicating the build-up of the BCG (e.g. cl1037, cl1054-12, cl1216, cl1232). Finally, those clusters for which spectroscopy is available (cl1040, cl1054-11, cl1054-12, cl1216, cl1232) contain spectroscopically-confirmed ellipticals which lie on relatively narrow red sequences. However, the ellipticals that have not been spectroscopically confirmed as cluster members show a significantly larger scatter which varies tremendously from cluster-to-cluster (e.g. cl1216 versus cl1232). This could be due to the fact that the photometric redshifts were calibrated conservatively so as to reject as few real cluster members as possible. It will be very interesting to further investigate these possible blue elliptical cluster members.

4.9 Conclusions

We have identified the merging galaxies among the E, S0, and Sa populations of nine high-redshift ($0.4 < z < 0.8$) clusters drawn from the ESO Distant Cluster Survey. After rejecting those mergers that are not cluster members based on the available spectroscopy and those mergers that are likely non-members based upon photometric redshifts, we compared the number of mergers with the number of non-merging ellipticals. The largest uncertainty in this comparison is the background subtraction. If we overestimate the number of mergers and underestimate the number of non-merging ellipticals, we find that the two quantities are comparable within the large errors. Therefore, the true merger fraction is smaller than the elliptical fraction, indicating that the large number of mergers found in MS1054-03 is atypical. We stress that this result is preliminary, and would benefit from spectroscopy of all merger candidates to determine cluster membership.

We also examined the merger candidates' distributions in both coordinate and color-magnitude space. Although the number of candidates found in some clusters is quite small, we find no strong trend for the mergers to preferentially reside in the outskirts of the clusters, as found in MS1054-03. This perhaps indicates that some of the mergers are chance superpositions along the line of sight. Again, additional spectroscopy would clarify the nature of these objects. The color-magnitude diagrams reveal that the merger candidates are for the most part bluer than the red sequence, indicating that their stellar populations are younger than the existing ellipticals, as found in MS1054-03.

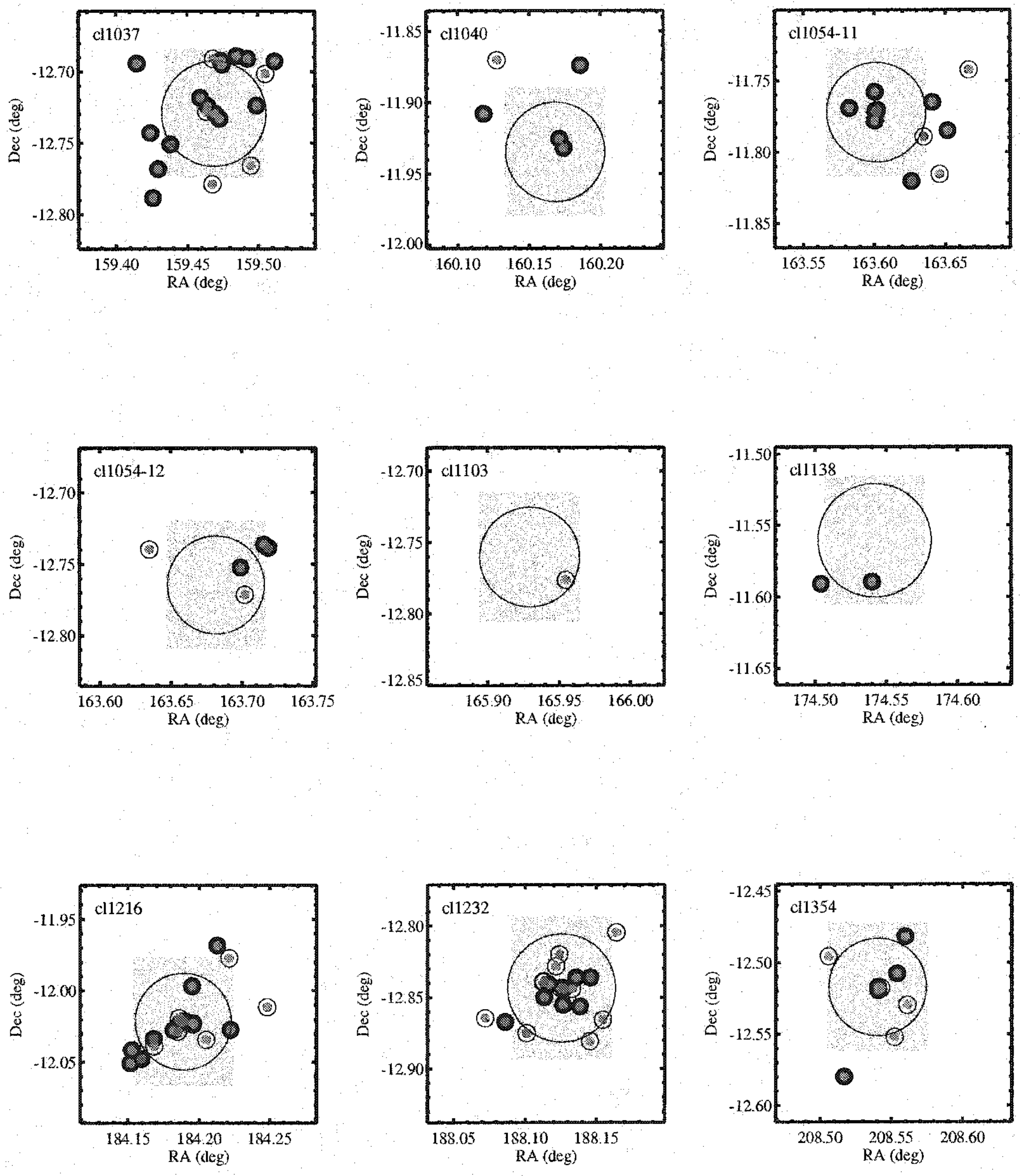

Figure 4.7 Spatial Distribution of Mergers. Filled circles are definite mergers. Hollow circles are possible mergers. Small, filled, red circles indicate cluster members based upon spectroscopy. Small, filled, green circles indicate membership based upon photometric redshifts. We have infrared data, and therefore more reliable photometric redshifts, over the shaded region. The circle has a radius of 1 Mpc and is centered on the brightest cluster galaxy.

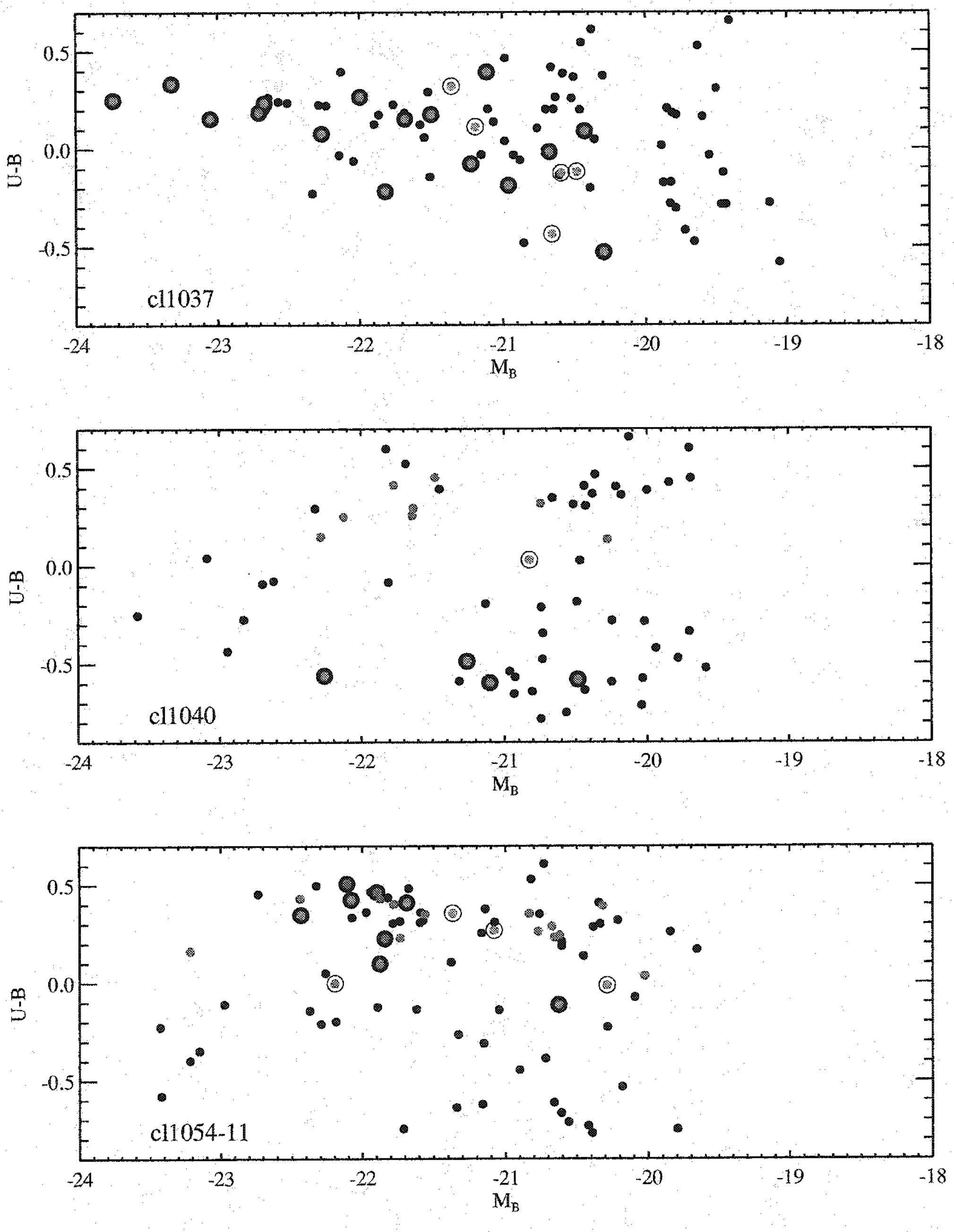

Figure 4.8 Mergers are depicted with the same symbols as in Figure 4.7. For those clusters which have available spectroscopic information, the red dots indicate elliptical galaxies that display absorption spectra. The black dots indicate elliptical galaxies without spectra that may be cluster members, based on their photometric redshifts.

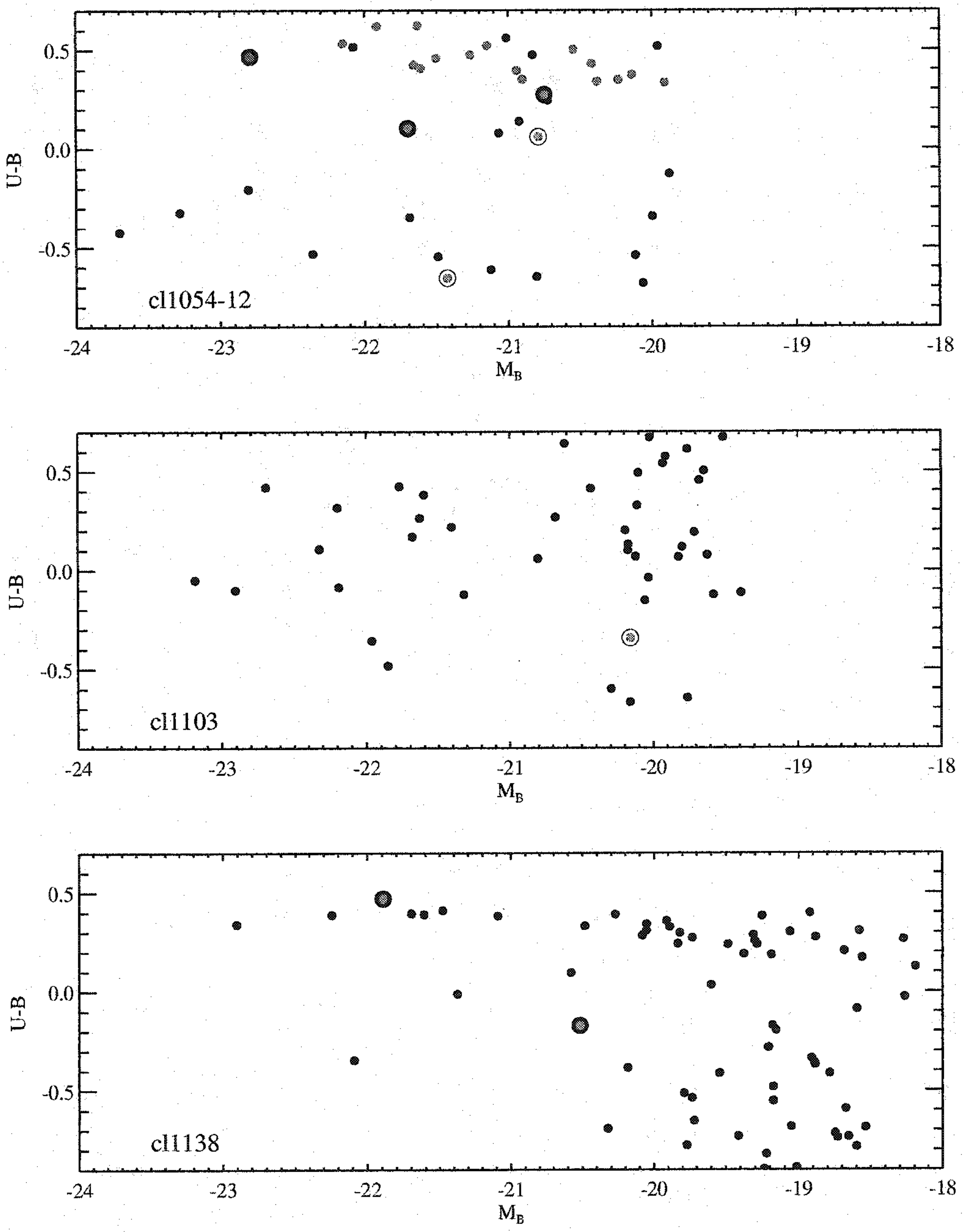

Figure 4.9 Same as Figure 4.8.

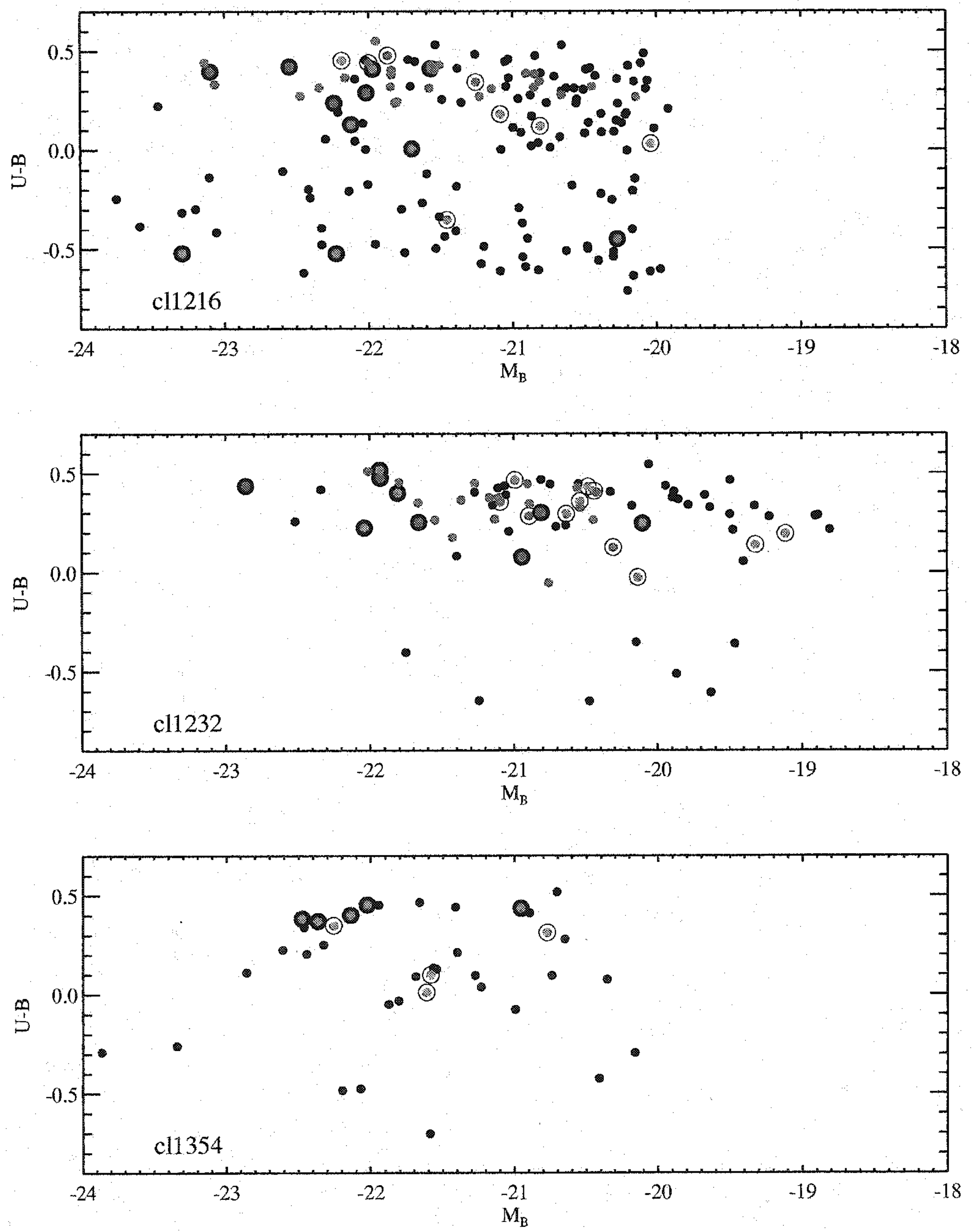

Figure 4.10 Same as Figure 4.8.

BIBLIOGRAPHY

Abell, G. O. 1965, ARAA, 3, 1

Abraham, R. G., Tanvir, N. R., Santiago, B. X., Ellis, R. S., Glazebrook, K., & van den Bergh, S. 1996, MNRAS, 279, L47

Andreon, S. 1998, ApJ, 501, 533

Andreon, S., Davoust, E., & Heim, T. 1997, A&A, 323, 337

Aragon-Salamanca, A., Ellis, R. S., Couch, W. J., & Carter, D. 1993, MNRAS, 262, 764

Arimoto, N., & Yoshii, Y. 1987, A&A, 173, 23

Bahcall, N. A., McKay, T. A., Annis, J., Kim, R. S. J., Dong, F., Hansen, S., Goto, T., Gunn, J. E., Miller, C., Nichol, R. C., Postman, M., Schneider, D., Schroeder, J., Voges, W., Brinkmann, J., & Fukugita, M. 2003, ApJS, 148, 243

Barger, A. J., Aragon-Salamanca, A., Ellis, R. S., Couch, W. J., Smail, I., & Sharples, R. M. 1996, MNRAS, 279, 1

Barger, A. J., Aragon-Salamanca, A., Smail, I., Ellis, R. S., Couch, W. J., Dressler, A., Oemler, A., Poggianti, B. M., & Sharples, R. M. 1998, ApJ, 501, 522

Barkana, R., Haiman, Z., & Ostriker, J. P. 2001, ApJ, 558, 482

Barnes, J. E. 1988, ApJ, 331, 699

—. 1989, Nature, 338, 123

—. 1992, ApJ, 393, 484

Barnes, J. E., & Hernquist, L. 1992, ARAA, 30, 705

Baugh, C. M., Cole, S., & Frenk, C. S. 1996, MNRAS, 283, 1361

Beers, T. C., Flynn, K., & Gebhardt, K. 1990, AJ, 100, 32

Bender, R., Saglia, R. P., Ziegler, B., Belloni, P., Greggio, L., Hopp, U., & Bruzual, G. 1998, ApJ, 493, 529

Bender, R., Ziegler, B., & Bruzual, G. 1996, ApJ, 463, L51

Benson, A. J., Frenk, C. S., Baugh, C. M., Cole, S., & Lacey, C. G. 2003, MNRAS, 343, 679

Bernardi, M., Sheth, R. K., Annis, J., Burles, S., Eisenstein, D. J., Finkbeiner, D. P., Hogg, D. W., Lupton, R. H., Schlegel, D. J., SubbaRao, M., Bahcall, N. A., Blakeslee, J. P., Brinkmann, J., Castander, F. J., Connolly, A. J., Csabai, I., Doi, M., Fukugita, M., Frieman, J., Heckman, T., Hennessy, G. S., Ivezić, Ž., Knapp, G. R., Lamb, D. Q., McKay, T., Munn, J. A., Nichol, R., Okamura, S., Schneider, D. P., Thakar, A. R., & York, D. G. 2003, AJ, 125, 1866

Blanton, M. R., Brinkmann, J., Csabai, I., Doi, M., Eisenstein, D., Fukugita, M., Gunn, J. E., Hogg, D. W., & Schlegel, D. J. 2003, AJ, 125, 2348

Blumenthal, G. R., Faber, S. M., Flores, R., & Primack, J. R. 1986, ApJ, 301, 27

Bode, P., Bahcall, N. A., Ford, E. B., & Ostriker, J. P. 2001, ApJ, 551, 15

Bond, J. R., Cole, S., Efstathiou, G., & Kaiser, N. 1991, ApJ, 379, 440

Borgani, S., Governato, F., Wadsley, J., Menci, N., Tozzi, P., Quinn, T., Stadel, J., & Lake, G. 2002, MNRAS, 336, 409

Bower, R. G. 1991, MNRAS, 248, 332

Bower, R. G., Lucey, J. R., & Ellis, R. S. 1992, MNRAS, 254, 601

Bressan, A., Chiosi, C., & Fagotto, F. 1994, ApJS, 94, 63

Bullock, J. S., Kolatt, T. S., Sigad, Y., Somerville, R. S., Kravtsov, A. V., Klypin, A. A., Primack, J. R., & Dekel, A. 2001, MNRAS, 321, 559

Butcher, H., & Oemler, A. 1978, ApJ, 219, 18

—. 1984, ApJ, 285, 426

Cole, S., & Kaiser, N. 1989, MNRAS, 237, 1127

Cole, S., Lacey, C. G., Baugh, C. M., & Frenk, C. S. 2000, MNRAS, 319, 168

Colless, M. 1989, MNRAS, 237, 799

Colless, M., Burstein, D., Davies, R. L., McMahan, R. K., Saglia, R. P., & Wegner, G. 1999, MNRAS, 303, 813

Couch, W. J., Barger, A. J., Smail, I., Ellis, R. S., & Sharples, R. M. 1998, ApJ, 497, 188

Couch, W. J., Ellis, R. S., Sharples, R. M., & Smail, I. 1994, ApJ, 430, 121

Couch, W. J., & Sharples, R. M. 1987, MNRAS, 229, 423

Dalcanton, J. J. 1996, ApJ, 466, 92

Dalcanton, J. J., Spergel, D. N., & Summers, F. J. 1997, ApJ, 482, 659

Danese, L., de Zotti, G., & di Tullio, G. 1980, A&A, 82, 322

Davies, R. L., Burstein, D., Dressler, A., Faber, S. M., Lynden-Bell, D., Terlevich, R. J., & Wegner, G. 1987, ApJS, 64, 581

Davis, M., Efstathiou, G., Frenk, C. S., & White, S. D. M. 1985, ApJ, 292, 371

Djorgovski, S., & Davis, M. 1987, ApJ, 313, 59

Dressler, A. 1980a, ApJs, 42, 565

—. 1980b, ApJ, 236, 351

Dressler, A., Lynden-Bell, D., Burstein, D., Davies, R. L., Faber, S. M., Terlevich, R., & Wegner, G. 1987, ApJ, 313, 42

Dressler, A., Oemler, A. J., Butcher, H. R., & Gunn, J. E. 1994, ApJ, 430, 107

Dressler, A., Oemler, A. J., Couch, W. J., Smail, I., Ellis, R. S., Barger, A., Butcher, H., Poggianti, B. M., & Sharples, R. M. 1997, ApJ, 490, 577

Ellis, R. S., Smail, I., Dressler, A., Couch, W. J., Oemler, A. J., Butcher, H., & Sharples, R. M. 1997, ApJ, 483, 582

Fasano, G., Poggianti, B. M., Couch, W. J., Bettoni, D., Kjærgaard, P., & Moles, M. 2000, ApJ, 542, 673

Ferrarese, L. 2002, ApJ, 578, 90

Fukugita, M., Ichikawa, T., Gunn, J. E., Doi, M., Shimasaku, K., & Schneider, D. P. 1996, AJ, 111, 1748

Fukugita, M., Shimasaku, K., & Ichikawa, T. 1995, PASP, 107, 945

Gómez, P. L., Nichol, R. C., Miller, C. J., Balogh, M. L., Goto, T., Zabludoff, A. I., Romer, A. K., Bernardi, M., Sheth, R., Hopkins, A. M., Castander, F. J., Connolly, A. J., Schneider, D. P., Brinkmann, J., Lamb, D. Q., SubbaRao, M., & York, D. G. 2003, ApJ, 584, 210

Gebhardt, K., Bender, R., Bower, G., Dressler, A., Faber, S. M., Filippenko, A. V., Green, R., Grillmair, C., Ho, L. C., Kormendy, J., Lauer, T. R., Magorrian, J., Pinkney, J., Richstone, D., & Tremaine, S. 2000, ApJ, 539, L13

Gehrels, N. 1986, ApJ, 303, 336

Gerhard, O., Kronawitter, A., Saglia, R. P., & Bender, R. 2001, AJ, 121, 1936

Ghigna, S., Moore, B., Governato, F., Lake, G., Quinn, T., & Stadel, J. 1998, MNRAS, 300, 146

—. 2000, ApJ, 544, 616

Giovanelli, R., Haynes, M. P., Herter, T., Vogt, N. P., da Costa, L. N., Freudling, W., Salzer, J. J., & Wegner, G. 1997, AJ, 113, 53

Girardi, M., & Mezzetti, M. 2001, ApJ, 548, 79

Gnedin, O. Y., & Ostriker, J. P. 2001, ApJ, 561, 61

Gonzalez, A. H., Williams, K. A., Bullock, J. S., Kolatt, T. S., & Primack, J. R. 2000, ApJ, 528, 145

Gonzalez, A. H., Zaritsky, D., Dalcanton, J. J., & Nelson, A. 2001, ApJS, 137, 117

Goto, T., Yamauchi, C., Fujita, Y., Okamura, S., Sekiguchi, M., Smail, I., Bernardi, M., & Gomez, P. L. 2003, MNRAS, 346, 601

Governato, F., Baugh, C. M., Frenk, C. S., Cole, S., Lacey, C. G., Quinn, T., & Stadel, J. 1998, Nature, 392, 359

Governato, F., Moore, B., Cen, R., Stadel, J., Lake, G., & Quinn, T. 1997, New Astronomy, 2, 91

Griffiths, R. E., Casertano, S., Ratnatunga, K. U., Neuschaefer, L. W., Ellis, R. S., Gilmore, G. F., Glazebrook, K., Santiago, B., Huchra, J. P., Windhorst, R. A., Pascarelle, S. M., Green, R. F., Illingworth, G. D., Koo, D. C., & Tyson, A. J. 1994, ApJ, 435, L19

Gunn, J. E., Carr, M., Rockosi, C., Sekiguchi, M., Berry, K., Elms, B., de Haas, E., Ivezić, Ž., Knapp, G., Lupton, R., Pauls, G., Simcoe, R., Hirsch, R., Sanford, D., Wang, S., York, D., Harris, F., Annis, J., Bartozek, L., Boroski, W., Bakken, J., Haldeman, M., Kent, S., Holm, S., Holmgren, D., Petravick, D., Prosapio, A., Rechenmacher, R., Doi, M., Fukugita, M., Shimasaku, K., Okada, N., Hull, C., Siegmund, W., Mannery, E., Blouke, M., Heidtman, D., Schneider, D., Lucinio, R., & Brinkman, J. 1998, AJ, 116, 3040

Gunn, J. E., & Gott, J. R. I. 1972, ApJ, 176, 1

Hayashi, E., Navarro, J. F., Taylor, J. E., Stadel, J., & Quinn, T. 2003, ApJ, 584, 541

Helsdon, S. F., & Ponman, T. J. 2003, MNRAS, 339, L29

Hernquist, L. 1990, ApJ, 356, 359

—. 1992, ApJ, 400, 460

Hernquist, L., Spergel, D. N., & Heyl, J. S. 1993, ApJ, 416, 415

Hui, L. 2001, Physical Review Letters, 86, 3467

Jenkins, A., Frenk, C. S., White, S. D. M., Colberg, J. M., Cole, S., Evrard, A. E., Couchman, H. M. P., & Yoshida, N. 2001, MNRAS, 321, 372

Jones, L., Smail, I., & Couch, W. J. 2000, ApJ, 528, 118

Jørgensen, I. 1999, MNRAS, 306, 607

Jørgensen, I., Franx, M., Hjorth, J., & van Dokkum, P. G. 1999, MNRAS, 308, 833

Kaiser, N. 1984, ApJ, 284, L9

Katz, N., & White, S. D. M. 1993, ApJ, 412, 455

Kauffmann, G. 1996, MNRAS, 281, 487

Kelson, D. D., van Dokkum, P. G., Franx, M., Illingworth, G. D., & Fabricant, D. 1997, ApJ, 478, L13+

Klypin, A., Gottlöber, S., Kravtsov, A. V., & Khokhlov, A. M. 1999, ApJ, 516, 530

Kochanek, C. S., & White, M. 2001, ApJ, 559, 531

Kodama, T., & Arimoto, N. 1997, A&A, 320, 41

Kodama, T., Bower, R. G., & Bell, E. F. 1999, MNRAS, 306, 561

Kronawitter, A., Saglia, R. P., Gerhard, O., & Bender, R. 2000, A&AS, 144, 53

Lacey, C., & Cole, S. 1993, MNRAS, 262, 627

Larson, R. B. 1969, MNRAS, 145, 405

—. 1975, MNRAS, 173, 671

Lavery, R. J., Pierce, M. J., & McClure, R. D. 1992, AJ, 104, 2067

Lubin, L. M., Oke, J. B., & Postman, M. 2002, AJ, 124, 1905

Lubin, L. M., Postman, M., Oke, J. B., Ratnatunga, K. U., Gunn, J. E., Hoessel, J. G., & Schneider, D. P. 1998, AJ, 116, 584

Lupton, R. H., Gunn, J. E., Ivezić, Z., Knapp, G. R., Kent, S., & Yasuda, N. 2001, in ASP Conf. Ser. 238: Astronomical Data Analysis Software and Systems X, 269–+

Mac Low, M., & Ferrara, A. 1999, ApJ, 513, 142

Matteucci, F., & Tornambe, A. 1987, A&A, 185, 51

Melnick, J., & Sargent, W. L. W. 1977, ApJ, 215, 401

Miller, C. J., Genovese, C., Nichol, R. C., Wasserman, L., Connolly, A., Reichart, D., Hopkins, A., Schneider, J., & Moore, A. 2001, AJ, 122, 3492

Miralda-Escudé, J. 2002, ApJ, 564, 60

Mo, H. J., Mao, S., & White, S. D. M. 1998, MNRAS, 295, 319

Moore, B., Katz, N., Lake, G., Dressler, A., & Oemler, A. 1996, Nature, 379, 613

Moore, B., Lake, G., Quinn, T., & Stadel, J. 1999, MNRAS, 304, 465

Navarro, J. F., Frenk, C. S., & White, S. D. M. 1997, ApJ, 490, 493

Nichol, R. C., Miller, C., Connolly, A. J., Chong, S.-S., Genovese, C., Moore, A. W., Reichart, D., Schneider, J., Wasserman, L., Annis, J., Brinkman, J., Böhringer, H., Castander, F., McKay, T., Postman, M., Sheldon, E., Szapudi, I., Romer, K., & Voges, W. 2001, in Mining the Sky, 613–+

Oemler, A. J. 1974, ApJ, 194, 1

Oemler, A. J., Dressler, A., & Butcher, H. R. 1997, ApJ, 474, 561

Okamoto, T., & Habe, A. 2000, PASJ, 52, 457

Peebles, P. J. E. 2002, in ASP Conf. Ser. 283: A New Era in Cosmology, 351–+

Pipino, A., & Matteucci, F. 2004, MNRAS, 347, 968

Poggianti, B. M. 1997, A&AS, 122, 399

Poggianti, B. M., Smail, I., Dressler, A., Couch, W. J., Barger, A. J., Butcher, H., Ellis, R. S., & Oemler, A. J. 1999, ApJ, 518, 576

Postman, M., & Geller, M. J. 1984, ApJ, 281, 95

Postman, M., Lauer, T. R., Szapudi, I., & Oegerle, W. 1998, ApJ, 506, 33

Press, W. H., & Schechter, P. 1974, ApJ, 187, 425

Quinn, T., Katz, N., & Efstathiou, G. 1996, MNRAS, 278, L49

Reed, D., Gardner, J., Quinn, T., Stadel, J., Fardal, M., Lake, G., & Governato, F. 2003, MNRAS, 346, 565

Schade, D., Lilly, S. J., Crampton, D., Ellis, R. S., Le Fèvre, O., Hammer, F., Brinchmann, J., Abraham, R., Colless, M., Glazebrook, K., Tresse, L., & Broadhurst, T. 1999, ApJ, 525, 31

Schlegel, D. J., Finkbeiner, D. P., & Davis, M. 1998, ApJ, 500, 525

Schweizer, F. 2000, Royal Society of London Philosophical Transactions Series A, 358, 2063

Sheth, R. K., Bernardi, M., Schechter, P. L., Burles, S., Eisenstein, D. J., Finkbeiner, D. P., Frieman, J., Lupton, R. H., Schlegel, D. J., Subbarao, M., Shimasaku, K., Bahcall, N. A., Brinkmann, J., & Ivezić, Ž. 2003, ApJ, 594, 225

Sheth, R. K., Mo, H. J., & Tormen, G. 2001, MNRAS, 323, 1

Sheth, R. K., & Tormen, G. 1999, MNRAS, 308, 119

Shimasaku, K. 1993, ApJ, 413, 59

Smail, I., Dressler, A., Couch, W. J., Ellis, R. S., Oemler, A. J., Butcher, H., & Sharples, R. M. 1997, ApJS, 110, 213

Smith, G. P., Treu, T., Ellis, R. S., Moran, S. M., & Dressler, A. 2004, submitted to ApJ

Solanes, J. M., Salvador-Sole, E., & Sanroma, M. 1989, AJ, 98, 798

Somerville, R. S. 2002, ApJ, 572, L23

Somerville, R. S., & Primack, J. R. 1999, MNRAS, 310, 1087

Spitzer, L. J., & Baade, W. 1951, ApJ, 113, 413

Springel, V., & Hernquist, L. 2003, MNRAS, 339, 312

Springel, V., White, S. D. M., Tormen, G., & Kauffmann, G. 2001, MNRAS, 328, 726

Stadel, J. G. 2001, Ph.D. Thesis

Stanford, S. A., Eisenhardt, P. R., & Dickinson, M. 1998, ApJ, 492, 461

Stanford, S. A., Elston, R., Eisenhardt, P. R., Spinrad, H., Stern, D., & Dey, A. 1997, AJ, 114, 2232

Stoughton, C., Lupton, R. H., Bernardi, M., Blanton, M. R., Burles, S., Castander, F. J., Connolly, A. J., Eisenstein, D. J., Frieman, J. A., Hennessy, G. S., Hindsley, R. B., Ivezić, Ž., Kent, S., Kunszt, P. Z., Lee, B. C., Meiksin, A., Munn, J. A., Newberg, H. J., Nichol, R. C., Nicinski, T., Pier, J. R., Richards, G. T., Richmond, M. W., Schlegel, D. J., Smith, J. A., Strauss, M. A., SubbaRao, M., Szalay, A. S., Thakar, A. R., Tucker, D. L., Vanden Berk, D. E., Yanny, B., Adelman, J. K., Anderson, J. E., Anderson, S. F., Annis, J., Bahcall, N. A., Bakken, J. A., Bartelmann, M., Bastian, S., Bauer, A., Berman, E., Böhringer, H., Boroski, W. N., Bracker, S., Briegel, C., Briggs, J. W., Brinkmann, J., Brunner, R., Carey, L., Carr, M. A., Chen, B., Christian, D., Colestock, P. L., Crocker, J. H., Csabai, I., Czarapata, P. C., Dalcanton, J., Davidsen, A. F., Davis, J. E., Dehnen, W., Dodelson, S., Doi, M., Dombeck, T., Donahue, M., Ellman, N., Elms, B. R., Evans, M. L., Eyer, L., Fan, X., Federwitz, G. R., Friedman, S., Fukugita, M., Gal, R., Gillespie, B., Glazebrook, K., Gray, J., Grebel, E. K., Greenawalt, B., Greene, G., Gunn, J. E., de Haas, E., Haiman, Z., Haldeman, M., Hall, P. B., Hamabe, M., Hansen, B., Harris, F. H., Harris, H., Harvanek, M., Hawley, S. L., Hayes, J. J. E., Heckman, T. M., Helmi, A., Henden, A., Hogan, C. J., Hogg, D. W., Holmgren, D. J., Holtzman, J., Huang, C., Hull, C., Ichikawa, S., Ichikawa, T., Johnston, D. E., Kauffmann, G., Kim, R. S. J., Kimball, T., Kinney, E., Klaene, M., Kleinman, S. J., Klypin, A., Knapp, G. R., Korienek, J., Krolik, J., Kron, R. G., Krzesiński, J., Lamb, D. Q., Leger, R. F., Limmongkol, S., Lindenmeyer, C., Long, D. C., Loomis, C., Loveday, J., MacKinnon, B., Mannery, E. J., Mantsch, P. M., Margon, B., McGehee, P., McKay, T. A., McLean, B., Menou, K., Merelli, A., Mo, H. J., Monet, D. G., Nakamura, O., Narayanan, V. K., Nash, T., Neilsen, E. H., Newman, P. R., Nitta, A., Odenkirchen, M., Okada, N., Okamura, S., Ostriker, J. P., Owen, R., Pauls, A. G., Peoples, J., Peterson, R. S., Petravick, D., Pope, A., Pordes, R., Postman, M., Prosapio, A., Quinn, T. R., Rechenmacher, R., Rivetta, C. H., Rix, H., Rockosi, C. M., Rosner, R., Ruthmansdorfer, K., Sandford, D., Schneider, D. P., Scranton, R., Sekiguchi, M., Sergey, G., Sheth, R., Shimasaku, K., Smee, S., Snedden, S. A., Stebbins, A., Stubbs, C., Szapudi, I., Szkody, P., Szokoly, G. P., Tabachnik, S., Tsvetanov, Z., Uomoto, A., Vogeley, M. S., Voges, W., Waddell, P., Walterbos, R., Wang, S., Watanabe, M., Weinberg, D. H., White, R. L., White, S. D. M., Wilhite, B., Wolfe, D., Yasuda, N., York, D. G., Zehavi, I., & Zheng, W. 2002, AJ, 123, 485

Strateva, I., Ivezić, Ž., Knapp, G. R., Narayanan, V. K., Strauss, M. A., Gunn, J. E., Lupton, R. H., Schlegel, D., Bahcall, N. A., Brinkmann, J., Brunner, R. J., Budavári, T., Csabai, I., Castander, F. J., Doi, M., Fukugita, M., Győry, Z., Hamabe, M., Hennessy, G., Ichikawa, T., Kunszt, P. Z., Lamb, D. Q., McKay, T. A., Okamura, S., Racusin, J., Sekiguchi, M., Schneider, D. P., Shimasaku, K., & York, D. 2001, AJ, 122, 1861

Tantalo, R., Chiosi, C., Bressan, A., & Fagotto, F. 1996, A&A, 311, 361

Terlevich, A. I., Caldwell, N., & Bower, R. G. 2001, MNRAS, 326, 1547

Tinsley, B. M. 1972, ApJ, 178, 319

Toomre, A., & Toomre, J. 1972, ApJ, 178, 623

Tormen, G., Diaferio, A., & Syer, D. 1998, MNRAS, 299, 728

Trager, S. C., Faber, S. M., Worthey, G., & González, J. J. 2000, AJ, 119, 1645

Treu, T., Ellis, R. S., Kneib, J., Dressler, A., Smail, I., Czoske, O., Oemler, A., & Natarajan, P. 2003, ApJ, 591, 53

Tully, R. B., & Fouque, P. 1985, ApJS, 58, 67

Tully, R. B., Somerville, R. S., Trentham, N., & Verheijen, M. A. W. 2002, ApJ, 569, 573

van Dokkum, P. G., & Franx, M. 1996, MNRAS, 281, 985

van Dokkum, P. G., Franx, M., Fabricant, D., Illingworth, G. D., & Kelson, D. D. 2000, ApJ, 541, 95

van Dokkum, P. G., Franx, M., Fabricant, D., Kelson, D. D., & Illingworth, G. D. 1999, ApJ, 520, L95

van Dokkum, P. G., Franx, M., Kelson, D. D., & Illingworth, G. D. 1998, ApJ, 504, L17+

van Dokkum, P. G., & Stanford, S. A. 2003, ApJ, 585, 78

van Dokkum, P. G., Stanford, S. A., Holden, B. P., Eisenhardt, P. R., Dickinson, M., & Elston, R. 2001, ApJl, 552, L101

White, S. D. M., Davis, M., Efstathiou, G., & Frenk, C. S. 1987, Nature, 330, 451

White, S. D. M., & Frenk, C. S. 1991, ApJ, 379, 52

White, S. D. M., & Rees, M. J. 1978, MNRAS, 183, 341

White, S. D. M., Tully, R. B., & Davis, M. 1988, ApJ, 333, L45

Wirth, G. D., Koo, D. C., & Kron, R. G. 1994, ApJ, 435, L105

York, D. G., Adelman, J., Anderson, J. E., Anderson, S. F., Annis, J., Bahcall, N. A., Bakken, J. A., Barkhouser, R., Bastian, S., Berman, E., Boroski, W. N., Bracker, S., Briegel, C., Briggs, J. W., Brinkmann, J., Brunner, R., Burles, S., Carey, L., Carr, M. A., Castander, F. J., Chen, B., Colestock, P. L., Connolly, A. J., Crocker, J. H., Csabai, I., Czarapata, P. C., Davis, J. E., Doi, M., Dombeck, T., Eisenstein, D., Ellman, N., Elms, B. R., Evans, M. L., Fan, X., Federwitz, G. R., Fiscelli, L., Friedman, S., Frieman, J. A., Fukugita, M., Gillespie, B., Gunn, J. E., Gurbani, V. K., de Haas, E., Haldeman, M., Harris, F. H., Hayes, J., Heckman, T. M., Hennessy, G. S., Hindsley, R. B., Holm, S., Holmgren, D. J., Huang, C., Hull, C., Husby, D., Ichikawa, S., Ichikawa, T., Ivezić, Ž., Kent, S., Kim, R. S. J., Kinney, E., Klaene, M., Kleinman, A. N., Kleinman, S., Knapp, G. R., Korienek, J., Kron, R. G., Kunszt, P. Z., Lamb, D. Q., Lee, B., Leger, R. F., Limmongkol, S., Lindenmeyer, C., Long, D. C., Loomis, C., Loveday, J., Lucinio, R., Lupton, R. H., MacKinnon, B., Mannery, E. J., Mantsch, P. M., Margon, B., McGehee, P., McKay, T. A., Meiksin, A., Merelli, A., Monet, D. G., Munn, J. A., Narayanan, V. K., Nash, T., Neilsen, E., Neswold, R., Newberg, H. J., Nichol, R. C., Nicinski, T., Nonino, M., Okada, N., Okamura, S., Ostriker, J. P., Owen, R., Pauls, A. G., Peoples, J., Peterson, R. L., Petravick, D., Pier, J. R., Pope, A., Pordes, R., Prosapio, A., Rechenmacher, R., Quinn, T. R., Richards, G. T., Richmond, M. W., Rivetta, C. H., Rockosi, C. M., Ruthmansdorfer, K., Sandford, D., Schlegel, D. J., Schneider, D. P., Sekiguchi, M., Sergey, G., Shimasaku, K., Siegmund, W. A., Smee, S., Smith, J. A., Snedden, S., Stone, R., Stoughton, C., Strauss, M. A., Stubbs, C., SubbaRao, M., Szalay, A. S., Szapudi, I., Szokoly, G. P., Thakar, A. R., Tremonti, C., Tucker, D. L., Uomoto, A., Vanden Berk, D., Vogeley, M. S., Waddell, P., Wang, S., Watanabe, M., Weinberg, D. H., Yanny, B., & Yasuda, N. 2000, AJ, 120, 1579

Zaritsky, D., Nelson, A. E., Dalcanton, J. J., & Gonzalez, A. H. 1997, ApJ, 480, L91+

Ziegler, B. L., Saglia, R. P., Bender, R., Belloni, P., Greggio, L., & Seitz, S. 1999, A&A, 346, 13

Appendix A

POPULATING SUBHALOS WITH GALAXIES

The circular velocity profiles measured from dark matter simulations must be corrected before they may be compared to those measured in galaxies, which contain baryons in addition to dark matter. First, baryons directly increase the mass enclosed within a given radius. Second, collapsed baryons pull the dark matter halo into a more concentrated equilibrium configuration. Both of these corrections require knowledge of how the baryonic mass is distributed. In this appendix, we outline our statistical method for assigning galaxy types, masses, and sizes to the population of subhalos identified in the zero-redshift output of our highest resolution cluster simulation, HR Virgo.

A.1 Assigning Galaxy Types

Although galaxies exhibit a range of bulge-to-disk ratios, for simplicity we assign either a pure spheroidal or a pure disk baryonic component to each subhalo in the HR Virgo simulation (see §1.6). Spheroidals are described by a Hernquist density profile (Hernquist, 1990):

$$\rho(r) = \frac{M_{\rm sph}}{2\pi}\frac{R_{\rm sph}}{r}\frac{1}{(r+R_{\rm sph})^3}, \tag{A.1}$$

where $M_{\rm sph}$ is the total mass of the spheroid, and the scalelength $R_{\rm sph}$ is related to the projected half-light radius R_0 of a deVaucoleurs surface brightness profile by $R_{\rm sph} = 0.551 R_0$.

Late type galaxies are assumed to be infinitely thin, and have surface density profiles of the form

$$\Sigma(r) = \frac{M_{\rm d}}{2\pi R_{\rm d}^2} e^{-r/R_{\rm d}}, \tag{A.2}$$

where $R_{\rm d}$ is the disk scale length and $M_{\rm d} = 2\pi\Sigma_0 R_{\rm d}^2$. is the total mass of the disk.

Observationally, galaxy type is a function of circular velocity, with early type galaxies dominating at high $V_{\rm c}$ (Shimasaku, 1993; Kochanek & White, 2001; Sheth et al., 2003). Only the peak circular velocity of the dark matter component, $V_{\rm pk}$, can be measured for each subhalo. We therefore assume that if early type galaxies dominate at high $V_{\rm c}$, they also dominate at high $V_{\rm pk}$. We randomly assign each subhalo the designation of early or late type based upon the early type fraction as a function of $V_{\rm pk}$, $f_{\rm early}(V_{\rm pk})$. For simplicity we adopt a step function for $f_{\rm early}(V_{\rm pk})$.

$$f_{\rm early}\left(V_{\rm pk}\right) = \begin{cases} 0 & : \quad V_{\rm pk} < V_{\rm break} \\ 1 & : \quad V_{\rm pk} \geq V_{\rm break} \end{cases}, \tag{A.3}$$

where $125\,{\rm km\,s^{-1}} < V_{\rm break} < 150\,{\rm km\,s^{-1}}$. Alternative functional forms which provide smoother transitions in the run of galaxy type with $V_{\rm pk}$ do not produce significantly different results. Subtantially different values of $V_{\rm break}$ produce disagreement with the joint distribution of R_0 and σ_0 found by Bernardi et al. (2003) (see §A.3).

A.2 Assigning Galaxy Masses

In the previous section, we described our procedure for assigning either a Hernquist or exponential density profile to each subhalo. Each of these two profiles is parametrized by both a mass in collapsed baryons ($M_{\rm sph}$ or $M_{\rm d}$) and a scale length ($R_{\rm sph}$ or $R_{\rm d}$). As is usually done, we set the baryonic mass within each subhalo equal to a fraction of the virial mass of that subhalo at the time that the baryons collapsed.

The first step towards determining the mass in cooled baryons embedded within each subhalo is to determine the virial mass of each subhalo. The virial radius of a simulated dark matter halo is usually taken to be R_{200}, the radius interior to which the average density is equal to 200 times the critical density. The virial mass is then estimated as M_{200}, the mass interior to R_{200}. For subhalos, R_{200}, and therefore M_{200}, is very difficult to measure. In addition, the baryons likely collapsed prior to the subhalo falling into the cluster and suffering the dynamical effects therein. We are therefore interested in the value of M_{200} for each subhalo before cluster incorporation. Although the cluster environment can lead to significant mass stripping, the peak circular velocities of halos ($V_{\rm pk}$) remain relatively constant (Hayashi et al., 2003). We can therefore use the values of $V_{\rm pk}$ measured in the redshift zero simulation output to infer M_{200} using a correlation between the two found by Navarro et al. (1997):

$$\log\left(\frac{M_{200}}{10^{10}M_{\odot}}\right) = 3.23\log\left(\frac{V_{\rm pk}}{\rm km\,s^{-1}}\right) - 5.31. \tag{A.4}$$

Once M_{200} has been determined for each subhalo, the second step is to specify the fraction, $f_{\rm cool}$, of M_{200} that winds up as cooled baryons. For late-type galaxies, we adopt the fitting function found by Gonzalez et al. (2000) in an analysis of the semi-analytic models of Somerville & Primack (1999):

$$f_{\rm cool} \simeq 0.1\left(\frac{x-0.25}{1+x^2}\right), \tag{A.5}$$

where $x = V_{\rm pk}/(200\,{\rm km\,s^{-1}})$. The above is valid for late type galaxies with $V_{\rm pk} \simeq 60 - 350\ \ {\rm km\,s^{-1}}$. For subhalos with $V_{\rm pk} \leq 60\,{\rm km\,s^{-1}}$, we set $f_{\rm cool} = 0.02$. This minimum value of $f_{\rm cool}$ does not affect our comparison to observations, as subhalos with $V_{\rm pk} \leq 60\,{\rm km\,s^{-1}}$ are unlikely to have $V_{\rm c} > V_{\rm compl}$. For early type galaxies, we explore $f_{\rm cool} = 0.025, 0.05, 0.1$.

A.3 Early Type Galaxy Sizes

In the previous two sections, we presented simple prescriptions for assigning a density profile shape and normalization to each subhalo within our highest resolution cluster simulation. Before the effects of baryons on galaxy rotation curves can be explored, we must assign scale lengths to the baryonic component of each subhalo. One projection of the Fundamental Plane tells us that the line of sight velocity dispersions, $\sigma_{\rm los}$, of early type galaxies are correlated with their half-light radii, R_0, which are in turn simply related to the scale length of a Hernquist density profile. Under the assumption that $\sigma_{\rm los}$ also correlates with the peak circular velocities $V_{\rm pk}$ of the dark matter halos in which they form, we can relate $R_{\rm sph}$ to $V_{\rm pk}$.

In order to assign values of $R_{\rm sph}$ to each subhalo, we first assign values of R_0. Using the full covariance matrix from B03, we draw one ($\sigma_{\rm los}$, R_0) pair for each subhalo selected through the procedure described in §A.1 to host an early type galaxy. Each value of R_0 is assigned a rank, with the largest R_0 receiving a rank of 1. Ranks are similarly assigned for each drawn $\sigma_{\rm los}$ and for each subhalo based opon its measured $V_{\rm pk}$. Although we do not know the relationship between $\sigma_{\rm los}$ and $V_{\rm pk}$, we expect both to correlate with R_0. Thus, we assign each ($\sigma_{\rm los}$, R_0) pair to a subhalo that has the same rank as that of the $\sigma_{\rm los}$ in that pair. This method of assigning sizes to subhalos preserves the scatter in the correlation between $\sigma_{\rm los}$ and R_0, but assumes a perfect correlation between $\sigma_{\rm los}$ and $V_{\rm pk}$.

Once values of R_0 have been assigned to each subhalo, $R_{\rm sph}$ is determined through $R_{\rm sph} = 0.551 R_0$.

A.4 Late Type Galaxy Sizes

Our statistical assignment of early type galaxy sizes to subhalos was driven by observed correlations. For disk galaxies, if baryons initially share the spatial and angular momentum distribution of their host dark matter halo, and conserve angular momentum as they collapse, the resulting scalelength is related to the properties of the dark matter halo (Dalcanton et al., 1997; Mo et al., 1998). We use this idea to assign a scale length, $R_{\rm d}$, to each subhalo chosen to host a late type galaxies. Mo et al. (1998) show that

$$R_{\rm d} = \frac{1}{\sqrt{2}} \frac{j_{\rm d}}{f_{\rm cool}} \lambda R_{200} f_c^{-1/2} f_R, \tag{A.6}$$

where j_d is the fraction of the total halo angular momentum contained in the disk; $f_{\rm cool}$

is, as before, the fraction of the dark matter mass contained in cooling baryons; λ is the spin parameter of the dark matter halo; and R_{200} is the virial radius. Additionally,

$$f_c \simeq \frac{2}{3} + \left(\frac{c}{21.5}\right)^{0.7}, \tag{A.7}$$

where c is the halo concentration and

$$f_R \simeq \left(\frac{f_{\rm cool}}{j_{\rm d}}\frac{\lambda}{0.1}\right)^{(-0.06+2.71 f_{\rm cool}+0.0047 f_{\rm cool}/(j_{\rm d}\lambda))} \tag{A.8}$$

$$\times \left(1 - 0.019c + 0.00025c^2 + 0.52/c\right). \tag{A.9}$$

We have specified $f_{\rm cool}$ in §A.2, and we assume that $j_{\rm d} = f_{\rm cool}$. Bullock et al. (2001) analyzed a 60 h^{-1} Mpc simulation carried out with an adaptive refinement tree N–body code, and found that the average halo spin parameter, $\overline{\lambda} = 0.04$, is independent of $V_{\rm pk}$. They also find the following relation for halo concentration:

$$c \approx 14\sqrt{\frac{V_{\rm pk}}{200\ {\rm km\,s^{-1}}}} \tag{A.10}$$

Finally, R_{200}, the radius within which the average halo density is 200 times the critical density, was calculated from M_{200}, the mass enclosed within this radius:

$$R_{200} = \left(\frac{3M_{200}}{800\pi\rho_{\rm crit}}\right)^{1/3}, \tag{A.11}$$

where $\rho_{\rm crit,0} \approx 136 {\rm M_\odot kpc^{-3}}$ is the critical density of the universe and M_{200} was determined from Equation §A.4.

VITA

Vandana Desai received her B.S. in Astronomy at the California Institute of Technology in 1997, her M.S. in Astronomy at the University of Washington in 1998, and her Ph.D. in Astronomy at the University of Washington in 2004.